

Dynamics and equation of state dependencies of relevance for nucleosynthesis in supernovae and neutron star mergers

Hans-Thomas Janka¹ * and Andreas Bauswein²

Abstract Neutron stars (NSs) and black holes (BHs) are born when the final collapse of the stellar core terminates the lives of stars more massive than about 9 solar masses. This can trigger the powerful ejection of a large fraction of the star's material in a core-collapse supernova (CCSN), whose extreme luminosity is energized mostly by the decay of radioactive isotopes such as ^{56}Ni and its daughter nucleus ^{56}Co . When evolving in close binary systems, the compact relics of such infernal catastrophes spiral towards each other on orbits gradually decaying by gravitational-wave emission. Ultimately, the violent collision of the two components forms a more massive, rapidly spinning remnant, again accompanied by the ejection of considerable amounts of matter. These merger events can be observed by high-energy bursts of gamma rays with afterglows and electromagnetic transients called kilonovae, which radiate the energy released in radioactive decays of freshly assembled rapid neutron-capture elements. By means of their mass ejection and the nuclear and neutrino reactions taking place in the ejecta, both CCSNe and compact object mergers (COMs) are prominent sites of heavy-element nucleosynthesis and play a central role in the cosmic cycle of matter and the chemical enrichment history of galaxies. The nuclear equation of state (EoS) of NS matter, from neutron-rich to proton-dominated conditions and with temperatures ranging from about zero to roughly 100 MeV, is a crucial ingredient in these astrophysical phenomena. It determines their dynamical processes, their remnant properties even at the level of deciding between NS or BH, and the properties of the associated emission of neutrinos, whose interactions govern the thermodynamic conditions and the neutron-to-proton ratio for nucleosynthesis reactions in the innermost ejecta. This chapter discusses corresponding EoS dependent effects of relevance in CCSNe as well as COMs.

¹ Max-Planck-Institute for Astrophysics, Karl-Schwarzschild-Str. 1, 85748 Garching, Germany
e-mail: thj@mpa-garching.mpg.de

² GSI Helmholtzzentrum für Schwerionenforschung, Planckstraße 1, 64291 Darmstadt, Germany
e-mail: a.bauswein@gsi.de

* corresponding author

1 Dynamical events of neutron stars and their equation of state

Astrophysical phenomena involving neutron stars (NSs) and black hole (BHs) generate the most extreme conditions in the universe after the Big Bang. The temperatures, densities, degrees of neutronization, and magnetic field strengths realized in the interior of these relics of stellar evolution and in matter in their immediate surroundings cannot be explored in terrestrial experiments. Correspondingly, the description of physical processes that involve such objects heavily rests on theoretical models for the dynamics and of the relevant microphysics. The same holds true for the prediction of associated observable signals and the interpretation of such measurements. Because of their extraordinary conditions, compact stellar remnants are therefore unique laboratories of nuclear physics, gravitational physics, and particle physics, in particular of high-energy neutrino physics.

This chapter will provide an introduction to the dynamical scenarios that lead to NS and BH formation by the collapse of massive stars and the final collisions of two such bodies after their secular inspiral in binary systems over tens of millions to billions of years (Figure 1). These violent cosmic events can generate densities up to more than $2 \times 10^{15} \text{ g cm}^{-3}$ (nearly 8 times higher than the nuclear saturation density of $n_0 \approx 0.16 \text{ nucleons fm}^{-3}$ or $\rho_0 \approx 2.66 \times 10^{14} \text{ g cm}^{-3}$). Temperatures up to roughly 100 MeV (about 10^{12} K) can be reached inside the new-born NSs (the so-called proto-NSs; PNSs) and during the mergers of two NSs, and matter that gets explosively expelled from the close vicinity of the compact objects starts its expansion with temperatures that can exceed $\sim 1 \text{ MeV}$ (about 10^{10} K), where nuclear statistical equilibrium (NSE) is established. In such environments neutrino emission and absorption processes play a pivotal role, and the neutron-to-proton ratios can therefore range from close to zero up to nearly unity. The discussion in this chapter will be focused on the influence of the high-density equation of state (EoS) of hot NS matter on the dynamical evolution of core-collapse supernovae (CCSNe) and compact object mergers (COMs) and on how these dependencies affect the production of heavy chemical elements in their ejecta. The nucleosynthesis in the expelled material can also open new ways to gain more information about the EoS of NS matter, which is still incompletely known, in particular also at non-zero temperatures.

Traditionally, the mass-radius relation of cold NSs, which is a characteristic property of the NS structure and depends on the pressure-density relation of the dense-matter EoS, is constrained by measuring lower limits of the maximum NS mass as well as determinations or estimates of NS radii. These can be obtained through astronomical observations of close binary-star systems, mainly double NS binaries, white dwarf-NS binaries, and X-ray or optical binaries where a NS or BH accretes mass from a nondegenerate, gas-donating companion. The currently tightest lower bounds on the maximum NS mass come from massive pulsars in relativistic or very compact binaries: $1.91 \pm 0.02 M_\odot$ for PSR J1614-2230 (Arzoumanian et al., 2018), $2.01 \pm 0.04 M_\odot$ for PSR J0348+0432 (Antoniadis et al., 2013), $2.14_{-0.09}^{+0.10} M_\odot$ for PSR J0740+6620 (Cromartie et al., 2020), $2.13 \pm 0.04 M_\odot$ for PSR J1810+1744 (Romani et al., 2021), and $2.35 \pm 0.17 M_\odot$ for the “black widow” pulsar PSR J0952-0607 (Romani et al., 2022) (1σ confidence intervals). Combining information from

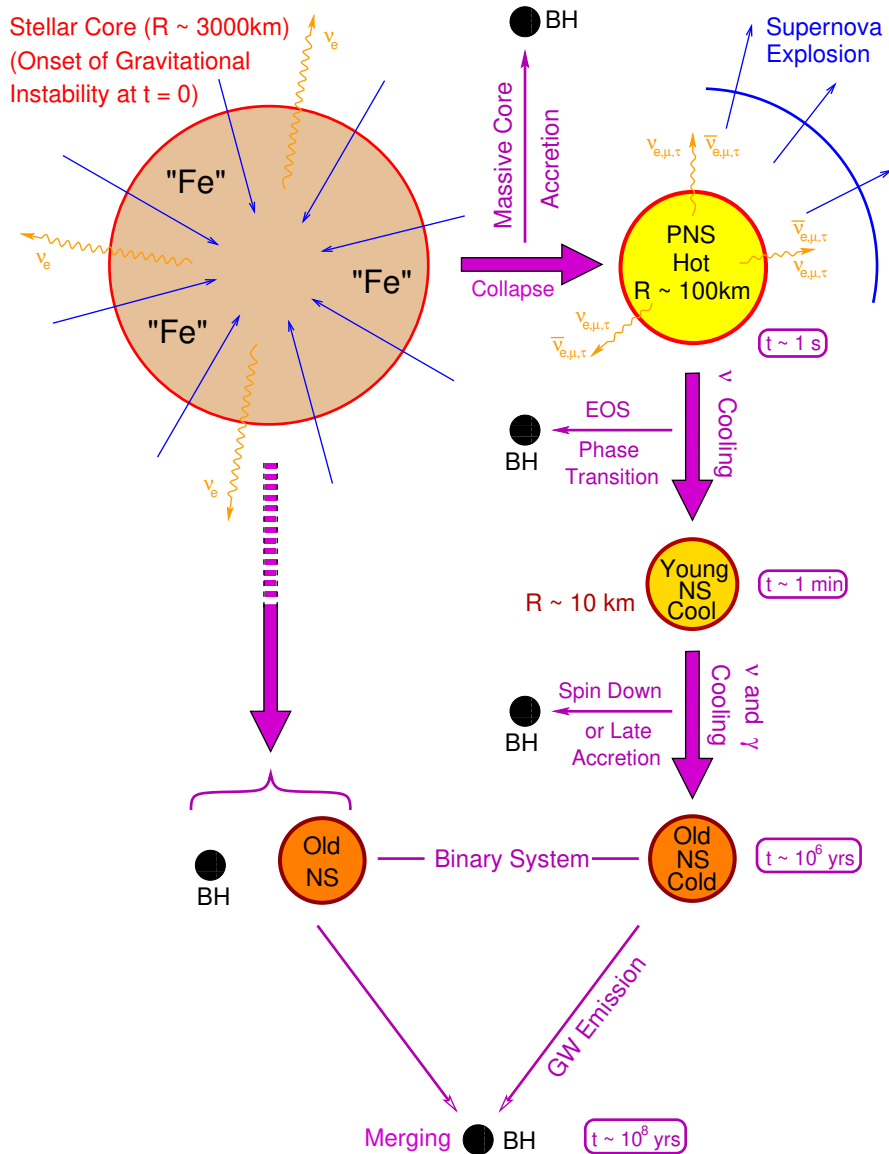


Fig. 1 Evolution paths from collapsing massive stars to NSs and stellar-mass BHs. The gravitational instability of the degenerate core (mostly composed of iron-group elements) of a massive star can either lead to the “direct” formation of a BH by continuous accretion of matter onto the transiently formed proto-NS (PNS) without any concomitant CCSN explosion. If a successful explosion is launched, an initially hot PNS cools by intense emission of neutrinos and antineutrinos of all flavors. On the way to an old, cold NS, a phase transition in the high-density EoS, spin-down by angular momentum loss (e.g., through magnetic fields), or late accretion of matter that does not achieve to get unbound in the CCSN explosion can lead to the delayed collapse of the PNS or young NS to a BH. In close binary systems the compact remnants spiral towards each other by GW emission to merge after tens of millions to billions of years, giving birth to a BH or, in some cases, a very massive NS. Mass ejection during the CCSN explosion and COM yields important contributions to the cosmic formation of heavy chemical elements. The dynamics of these processes and the associated emission of neutrinos are governed by the properties of the high-density EoS in PNSs and NSs.

the last case with reanalysis of other pulsars, a minimum value of $2.09 M_{\odot}$ for the maximum NS mass was concluded at 3σ confidence (Romani et al., 2022).

A new multimessenger window to the universe opened up in recent years with the now-possible measurements of gravitational wave (GW) signals from COM events (Abbott et al., 2021), in particular from the binary NS mergers of GW170817 (Abbott et al., 2017b, 2019) and GW190425 (Abbott et al., 2020), the former being associated with detections of a short gamma-ray-burst, GRB 170817A (Troja et al., 2017; Abbott et al., 2017a,c), and an ultraviolet, optical, and near-infrared electromagnetic transient, AT 2017gfo, a so-called kilonova (e.g., Pian et al., 2017; Tanvir et al., 2017; Smartt et al., 2017; Arcavi et al., 2017; Cowperthwaite et al., 2017). The GW signal from the NS-NS inspiral phase provided information on the tidal deformability of the NSs and thus new, important clues on the cold high-density EoS. The LIGO Scientific Collaboration together with the Virgo Collaboration deduced a total mass of the binary system of $2.74^{+0.04}_{-0.01} M_{\odot}$ and individual masses of $(1.36\text{--}1.60) M_{\odot}$ for the primary component and $(1.17\text{--}1.36) M_{\odot}$ for the secondary component (90% credible intervals), if the two NS spins are restricted to low values in the range of observed Galactic binary NSs (Abbott et al., 2017b). In addition, they could determine the radii of both NSs to be in the range from about $10.8^{+2.0}_{-1.7}$ km to $11.9^{+1.4}_{-1.4}$ km at the 90% credible level, depending on the description of macroscopic NS properties or a pressure-density parametrization of the EoS, respectively (Abbott et al., 2018).

State-of-the-art radius determinations were recently also obtained through observations and modelling of X-rays emitted from hot regions on the surface of rotating NSs, making use of data from the *Neutron Star Interior Composition Explorer* (NICER), an X-ray telescope installed on the International Space Station. For the isolated millisecond pulsar PSR J0030+0451 Riley et al. (2019) inferred a gravitational mass of $1.34^{+0.15}_{-0.16} M_{\odot}$ and an equatorial radius of $12.71^{+1.14}_{-1.19}$ km (approximately 16% and 84% quantiles), whereas Miller et al. (2019) estimated a gravitational mass of $1.44^{+0.15}_{-0.14} M_{\odot}$ and an equatorial circumferential radius of $13.02^{+1.24}_{-1.06}$ km (68% confidence). And for PSR J0740+6620, which is among the NSs with the highest well determined mass values, Riley et al. (2021) constrained the mass to be $2.072^{+0.067}_{-0.066} M_{\odot}$ and the equatorial radius to be $12.39^{+1.30}_{-0.98}$ km (posterior credible intervals bounded by the 16% and 84% quantiles). Combining these NICER determinations and the NS mass-radius constraints from GW170817, Raaijmakers et al. (2021) inferred 95% credible radius ranges of $12.33^{+0.76}_{-0.81}$ km or $12.18^{+0.56}_{-0.79}$ km for a $1.4 M_{\odot}$ NS, considering two different parameterizations of the high-density EoS and confirming previous bounds derived on grounds of a Bayesian analysis of a heterogeneous data set from X-ray observations (Type-I X-ray bursters and transient low-mass X-ray binaries) by Steiner et al. (2010).

Explosive astrophysical events that lead to high-temperature conditions such as CCSNe and binary NS mergers offer promising perspectives to obtain novel constraints on the intrinsic physics also of hot NS matter. This concerns the properties of the nuclear EoS as well as the neutrino reactions in such matter. GW signals and neutrino signals are messengers originating most directly from the high-density regions, reflecting effects associated with the bulk motions of the plasma (in GWs

and neutrinos) as well as the thermodynamical state of the emitting regions (in neutrinos). Both of these signals have already demonstrated their high potential, for GWs in connection with the NS merger event of GW170817, which occurred in the S0 galaxy NGC 4993 at a distance of 40 ± 4 Mpc (redshift of $z = 0.00968$) (Pian et al., 2017; Smartt et al., 2017), and for neutrinos in association with the once-in-a-hundred-years event of Supernova (SN) 1987A, which was the explosive death of the blue supergiant star Sanduleak $-69\ 202$ in the Tarantula Nebula of the Large Magellanic Cloud.

Two dozen electron antineutrinos from SN 1987A captured in the large underground water and scintillator experiments of Kamiokande II (Hirata et al., 1987), IMB (Bionta et al., 1987), and Baksan (Alekseev et al., 1987) proved the—at least transient—existence of a NS formed in the collapse of the stellar core. The integrated energy of the neutrino burst of approximately ~ 10 s duration provided rough constraints on the NS mass and its EoS, although with huge uncertainties because of the poor statistics of the measured neutrinos (e.g., Burrows, 1990a,b). A future CCSN in the Milky Way, however, which is expected to happen 1–3 times per century on average (e.g., Diehl et al., 2006), will yield splendid information on the time, energy, and potentially also flavor evolution of the emitted neutrinos (for a recent review, see Mirizzi et al., 2016).

In the case of GW170817 the distance of the source permitted to measure the GW signal only from the inspiral phase before the merger of the two NSs, because the final plunge and subsequent ring-down with their higher-frequency emission were too weak to be registered by the LIGO and Virgo detectors active at that time. Nevertheless, extremely useful limits on the tidal deformability parameter linked to the cold EoS of the pre-merger NSs could be deduced from the signal (Abbott et al., 2019) and provided valuable input for state-of-the-art constraints on the dense matter EoS and NS properties (e.g., Fattoyev et al., 2018; Raaijmakers et al., 2021). With the successively enhanced sensitivity of the GW interferometers, the number of detected NS-NS mergers is determined to grow and, with a sufficiently long period of measurements also close events will be discovered. These will ultimately permit to extract the ring-down GW signal with its characteristic peak frequency from quadrupole oscillations of the massive merger remnant (e.g., Oechslin & Janka, 2007; Bauswein et al., 2010; Stergioulas et al., 2011; Bauswein & Janka, 2012; Bauswein et al., 2012; Hotokezaka et al., 2013a; Takami et al., 2014, 2015; Bernuzzi et al., 2015; Rezzolla & Takami, 2016) and with further EoS-dependent features probing the high-temperature, high-density physics and potential phase transitions in the super-nuclear regime.

Also the fact that the kilonova AT 2017gfo was observed in connection to GW170817 can be used to infer constraints on the NS EoS. The electromagnetic emission of this astronomical transient over more than 10 days was powered by the radioactive decay heating of rapid neutron-capture (“r-process”) nuclei in approximately $0.05 M_{\odot}$ of ejected material (e.g., Kasen et al., 2017; Smartt et al., 2017; Perego et al., 2017). This implies a NS-NS merger remnant that has not collapsed to a BH immediately after the collision but, if the remnant finally collapsed, its gravitational instability is likely to have happened only considerably (tens of milliseconds

or more) after the instant of the merging. Only if the merger product survived for some time, a sufficient amount of mass could be added to the dynamical ejecta from the collision phase itself (which can account for up to roughly $0.02 M_{\odot}$; Bauswein et al., 2013; Hotokezaka et al., 2013b) by subsequent secular mass loss of the remnant through magnetohydrodynamic and viscous effects as well as neutrino-driven mass ejection (e.g. Fernández & Metzger, 2013; Perego et al., 2014; Just et al., 2015; Wu et al., 2016; Fernández & Metzger, 2016; Shibata et al., 2017; Radice et al., 2018). Making use of this argument, Bauswein et al. (2017) deduced lower limits on the radii of (cold) $1.6 M_{\odot}$ and maximum-mass NSs of $10.68^{+0.15}_{-0.04}$ km and $9.60^{+0.14}_{-0.03}$ km, respectively. Referring to the observation of the kilonova and its properties, in particular its large ejecta mass, the preceding GRB 170817A, and the general theoretical understanding of the merger dynamics, upper mass limits for non-rotating (spherical) NSs were inferred by Margalit & Metzger (2017) ($\sim 2.17 M_{\odot}$ at 90% confidence), Shibata et al. (2017) ($2.15\text{--}2.25 M_{\odot}$), Rezzolla et al. (2018) (between $2.01 \pm 0.04 M_{\odot}$ and $2.16^{+0.17}_{-0.15} M_{\odot}$), and Ruiz et al. (2018) ($2.16\text{--}2.28 M_{\odot}$).

This chapter aims at explicating these and other links between the nucleosynthesis occurring in CCSNe and COMs on the one hand and characteristic features of the high-density EoS in NSs on the other hand.

2 Core-collapse supernovae

2.1 Dynamical evolution and types of explosions

This section will provide a brief summary of the evolution of massive stars and their final ends in SN explosions. Theoretical and numerical research, most recently culminating in direct 3D simulations, and a wide spectrum of partly game-changing observational discoveries have led to increasingly deeper insights over more than 50 years, in particular also with respect to the enormous diversity of stellar death scenarios and the plethora of phenomena that can play a role during the post-main-sequence evolution (e.g., interactions of the components in binary stars). The wealth of literature in this wide field of research cannot be adequately accounted for here. Therefore the references provided will be constrained to a selection of reviews reflecting the development of the knowledge over the decades, earlier papers defining novel directions of the field, and some recent publications that provide information of the current status of the rapidly growing understanding. The selection will unavoidably be biased by personal views of the authors and it will be constrained by the goal to lay a very basic foundations for the subsequent discussion of SN nucleosynthesis and its dependences on the nuclear EoS of hot PNS matter.

Massive stars evolve over millions of years in hydrostatic equilibrium, assembling increasingly heavier chemical elements through a sequence of nuclear burning stages (for reviews, see, e.g., Woosley et al., 2002; Heger et al., 2003; Woosley & Janka, 2005). Thus these stars develop an onion-shell structure, in which the

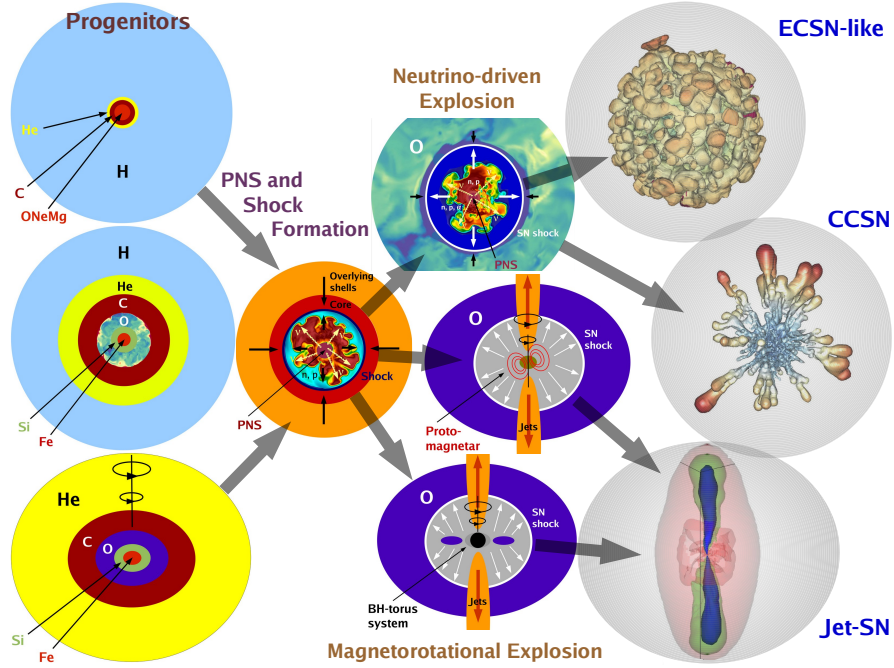


Fig. 2 Theoretical typology of SNe from massive stars. Different progenitors with their onion-shell structure indicated schematically by colored layers (not drawn to scale; *left column*) lead to different kinds of massive-star explosions (*right*). All types have in common that the degenerate stellar core, either composed of oxygen, neon, and magnesium in stars near the low-mass end of core-collapse progenitors (around $9 M_{\odot}$ for solar metallicity) or containing iron in more massive progenitors (up to the pair-instability regime), collapses to a neutrino-emitting PNS, which begins to assemble at the moment of core bounce, simultaneously with the formation of a strong shock wave (*second column*). Successful explosions can take place through the neutrino-driven mechanism or, in rapidly spinning progenitors, by a magnetorotational mechanism, which requires the efficient amplification of magnetic fields either in a proto-magnetar or in an accretion disk around a newly formed BH; this scenario is accompanied by the launch of two polar jets (*third column*). Low-mass progenitors with deep, tenuous, and very extended hydrogen envelopes thus lead to events similar to electron-capture-SNe of ONeMg-core progenitors (denoted by ECSN-like), more massive iron-core progenitors produce CCSNe, and rapidly rotating progenitors, which have often stripped their hydrogen envelopes, can end their lives by jet-driven or jet-associated SNe (*right column*). BHs are expected to form in rare cases of CCSNe as well as in jet-SNe besides those stellar core-collapse events that do not end in successful explosions. The asymmetric structures interior to the semi-transparent envelopes in the right column indicate anisotropic distributions of metals mixed outward from the SN core, which happens nearly spherically with small-scale variations for ECSN-like events and highly asymmetrically for CCSNe. In jet-SNe these metal-rich structures are dwarfed by the global, prolate deformation associated with the much faster polar jets

ashes of these burning phases accumulate in stratified layers that surround a degenerate core, whose stability against gravitational collapse is sustained by the quantum mechanical fermion pressure of degenerate electrons. In stars with birth (zero-age-main-sequence; ZAMS) masses of more than roughly $7\text{--}9 M_{\odot}$ (depending on the initial metal content or “metallicity” of the stellar plasma) the degenerate core undergoes a catastrophic implosion at the end of the star’s stable life to form a proto-NS (PNS) and to potentially initiate a SN explosion. The collapse sets in when the gas of electrons becomes highly relativistic and the mass of the degenerate stellar core approaches the Chandrasekhar limit. In the lowest-mass progenitors of SNe ($M_{\text{ZAMS}} \lesssim 9 M_{\odot}$), whose cores are composed of oxygen, neon, and magnesium, the gravitational instability of the stellar core is triggered by electron captures predominantly on ^{20}Ne (e.g., Kirsebom et al., 2019; Zha et al., 2019; Suzuki et al., 2019). In the iron cores of more massive progenitors, which possess higher entropies and are hotter, photo-disintegration reactions of iron nuclei through thermal gamma rays initiate a fatal contraction before electron captures (first on nuclei, later also on an increasing number of free protons) cause a runaway process that ultimately leads to the dynamical collapse (e.g., Langanke et al., 2003; Janka et al., 2007).

In both cases the infall stops only when super-nuclear densities are reached at the center and the EoS stiffens by the phase transition to homogeneous nuclear matter, generating dominant abundances of free neutrons and protons instead of heavy nuclei. The subsonically collapsing central part of the stellar core (the “inner core” with a mass of $0.4\text{--}0.5 M_{\odot}$) overshoots its equilibrium density, the repulsive component of the strong force between the nucleons drives its re-expansion, and this so-called core bounce sends a strong shock wave into the supersonically infalling outer layers of the stellar core. This shock wave propagates outward in mass and radius, but on its way it loses enormous amounts of energy by photo-dissociation of heavy nuclei into free nucleons (consuming more than 8 MeV per nucleon). More energy loss happens by the emission of a bright flash (“shock break-out burst”) of electron neutrinos, which are released through rapid electron captures by the abundant free protons behind the shock when the latter reaches neutrino-transparent low-density conditions. In combination, both effects weaken the shock and lead to shock stagnation within milliseconds after core bounce, implying that the bounce shock is unable to initiate a successful explosion because it transforms to a standing accretion shock. This means that not only the preshock velocities but also the postshock velocities of the stellar medium become negative. Therefore the newly forming NS continues to grow in mass but no ejection of matter develops at this stage.

Different mechanisms have been suggested to revive the stalled SN shock. The most widely accepted ones are the delayed neutrino-heating mechanism and magneto-rotationally driven explosions (Figure 2). A mechanism based on quark deconfinement is a more recent non-standard idea for achieving explosions, which, however, requires specific assumptions about the behavior of the super-nuclear EoS in hot, quite massive PNSs.

2.1.1 Neutrino-driven explosions

The neutrino-driven mechanism taps the enormous gravitational binding energy — several 10^{53} erg and thus several hundred times the explosion energy of a canonical CCSN— that is set free when the degenerate stellar core collapses to a NS (Colgate & White, 1966). Neutrinos and antineutrinos of all flavors, which are produced by particle reactions in the hot PNS interior, escape in huge numbers (about 10^{58} in total) from the PNS surface (“neutrinosphere”), carry away this binding energy, and govern the gradual conversion of the initially proton-rich matter of the PNS to the final, neutron-dominated medium of the cold, deleptonized NS. On their way of leaving the collapsing stellar core, these neutrinos can transfer a small fraction (on the order of typically one percent) of their total energy to the layer behind the stagnant shock wave. This is accomplished mainly through electron neutrino and antineutrino captures on free neutrons and protons, respectively,

$$\nu_e + n \longrightarrow e^- + p, \quad (1)$$

$$\bar{\nu}_e + p \longrightarrow e^+ + n, \quad (2)$$

which dominate over the inverse processes

$$e^- + p \longrightarrow \nu_e + n, \quad (3)$$

$$e^+ + n \longrightarrow \bar{\nu}_e + p, \quad (4)$$

in the so-called gain layer, which is the region between the gain radius and the SN shock, where neutrino heating exceeds neutrino cooling (Bethe & Wilson, 1985; Bethe, 1990). In order to power the SN explosion, neutrinos thus tap the thermal and degeneracy energy that is built up in the PNS by the conversion of gravitational energy during stellar core collapse. The efficiency of the energy transfer is typically around 5–10%, measuring the fraction of the luminosity radiated in ν_e and $\bar{\nu}_e$ that is absorbed by the matter in the gain layer. The neutrino energy deposition continues for several seconds before the explosion energy approaches its saturation level for the CCSNe of massive progenitors (e.g., Bollig et al., 2021).

These neutrino-powered explosions develop pronounced large-scale asymmetries in their innermost ejecta, connected to non-radial hydrodynamic instabilities that occur in the postshock layer due to convective overturn of neutrino-heated gas (Herant et al., 1994; Burrows et al., 1995; Janka & Müller, 1996) and due to a generic, global, oscillatorily growing accretion instability of the shock, the standing accretion shock instability (SASI; Blondin et al., 2003; Blondin & Mezzacappa, 2007; Foglizzo et al., 2015). Both assist the neutrino-heating mechanism by a corresponding buoyancy-driven expansion of the postshock matter or by shock expansion due to SASI sloshing and spiral modes, which have been interpreted in terms of effects associated with turbulent mass motions on the largest scales. The violent flows drive the shock outward and therefore increase the volume and mass in the gain layer, thus enabling more neutrino-energy deposition and the runaway expansion of the shock that is necessary for a successful SN explosion. The large-scale asymme-

tries imprinted on the postshock matter, which are often dominated by dipolar and quadrupolar modes (see, e.g., Burrows et al., 2020; Müller, 2020), are preserved in terms of later asymmetries of the heavy-element distributions (in particular of the intermediate-mass elements between neon and the iron group) on the largest scales, i.e., in opposite hemispheres and different octants (Wongwathanarat et al., 2013; Katsuda et al., 2018). CCSNe are thus expected to be globally asymmetric in their interior, in particular w.r.t. the metal core (Figure 2). They also exhibit extensive radial mixing of the metals into the helium shell and hydrogen envelope of the exploding stars because the initial ejecta asymmetries trigger entrainment and fragmentation at the composition-shell interfaces of the progenitors due to the growth of secondary (Rayleigh–Taylor, Kelvin–Helmholtz, and Richtmyer–Meshkov) instabilities near the shell boundaries after the passage of the outgoing SN shock (for more details on different aspects of the CCSN problem, see recent reviews and comprehensive studies on this topic and references therein, e.g., Janka, 2012; Burrows, 2013; Janka et al., 2016; Janka, 2017; Müller, 2020; Stockinger et al., 2020; Sandoval et al., 2021; Burrows & Vartanyan, 2021).

Sometimes a distinction is made between the SN explosions of the lowest-mass progenitors with either ONeMg cores or iron cores (and representatives in the ZAMS mass range below $\sim 10 M_{\odot}$) and the CCSNe of more massive stars (e.g., Müller, 2016). The former cases are termed electron-capture SNe (ECSNe) or ECSN-like events, respectively, because they possess characteristic differences in their progenitor and explosion properties compared to CCSNe, although in ECSN-like events as well as CCSNe the explosions are thought to be powered by neutrino energy transfer. The degenerate cores of the mentioned low-mass stars have lower entropies and temperatures than the iron cores of more massive progenitors, for which reason their electron chemical potentials are particularly high. This explains why electron captures on ^{20}Ne yield the first initiation of the gravitational instability in the case of ONeMg cores, whereas photo-disintegration and the corresponding NSE shift are more relevant for the more massive iron cores in more massive progenitors. In addition to this difference in the physics that triggers the core collapse, the particularly steep density gradient at the edge of the degenerate core, i.e., at the interface between ONeMg or Fe core and the overlying shells, enables different explosion dynamics, despite the explosion mechanism being based on neutrino-heating in both ECSN-like events and CCSNe. Since the SN shock accelerates outward as it travels down the steep density gradient in ECSN-like cases, the explosion develops shortly after bounce, i.e., the accelerated outward expansion of the SN shock starts within only some 10 ms up to about 100 ms instead of being delayed for several 100 ms in more massive stars. Correspondingly, convective overturn sets in concomitantly to the explosion but it is not crucial for the success of the SN blast. The short phase of postshock convection leads to only modest, small-scale anisotropies in the ejecta without the presence of dominant dipolar or quadrupolar asymmetry modes. After only a short phase of convective overturn, a neutrino-driven wind sets in, in which neutrino-heated gas is blown off from the PNS surface by neutrino heating essentially in a spherically symmetrical way and provides additional push to the explosion. Because the wind contains only little mass

(typically several $10^{-3} M_{\odot}$) and its power is low, the final explosion energy is usually also low—around 10^{50} erg instead of the canonical value of about 10^{51} erg of CCSNe—and reaches its terminal value within less than one second, the ejecta velocities are small, the SN is globally spherical, and also the radial mixing of metals in ECSN-like events is weak (Figure 2). Consistent with that, the NS kicks associated with the weakly asymmetric, low-energy explosions are only of the order of 10 km s^{-1} and thus much below the typical natal kicks of NSs of several 100 km s^{-1} (e.g., Stockinger et al., 2020; Kozyreva et al., 2021, 2022).

2.1.2 Magnetorotational explosions

In contrast to the neutrino-heating mechanism, the magneto-rotational mechanism makes use of the energy of rotation in a rapidly and differentially spinning PNS that is formed during the collapse of a fast-rotating progenitor with an average iron-core rotation period shorter than roughly 10 s, corresponding to iron-core angular momenta close to 10^{49} erg s or more. Under such circumstances magnetic fields are amplified not only by compression and in turbulent flow vortices but also by winding in differentially rotating layers, convective dynamo action, and the magnetorotational instability (MRI) to reach strengths of up to 10^{15} – 10^{16} G also in the large-scale field of the PNS. Moreover and equally relevant, under such circumstances the kinetic energy of rotation amounts to several 10^{51} erg at a time when the PNS still has a radius around 30 km, which is typical of the phase during which the explosion is expected to develop. The free energy of rotation that is released when the PNS evolves from a differentially rotating to a rigidly rotating object can be a fair fraction of the total rotation energy, i.e., of the order of several 10^{50} erg. Therefore it can make a significant contribution to the canonical explosion energy of CCSNe. If the total reservoir of rotational energy in the final, maximally spinning NS with $\sim (10\text{--}12)$ km radius could be tapped via magnetic fields, explosion energies up to several 10^{52} erg could be produced. This is sufficient to explain the most energetic observed stellar explosions.

The transfer of this energy through magnetic forces can drive fast mass ejection in jet-like magnetic towers along the poles, initiating an asymmetric, highly prolate explosion (Figure 2). Magnetically induced mass ejection is also possible in the equator-near directions, but the success or failure of the explosion and the exact dynamics and properties of the blast and its associated outflows in jets are extremely sensitive to the progenitor conditions, in particular to the core rotation and the strength and geometry of the magnetic fields prior to collapse. These initial conditions determine the field amplification in the new-born NS and the field-triggered mass ejection. For recent progress in the numerical modelling of such events, see, e.g., Bugli et al. (2021) and Obergaulinger & Aloy (2022) and references therein. Such magnetorotational explosions are expected to leave behind highly magnetized PNSs, so-called proto-magnetars, with millisecond periods (Aloy & Obergaulinger, 2021).

Also BHs can be formed in the collapse of rapidly spinning, magnetized progenitors, either after a successful explosion or before. These BHs then continue to accrete matter from the collapsing star through a centrifugally stabilized, thick accretion torus. In this so-called collapsar scenario, energy release from the torus by neutrinos, magnetohydrodynamic flows, and magnetically or turbulence-mediated viscous dissipation of rotational energy may also lead to jet production and mass ejection in a stellar explosion (Woosley, 1993; MacFadyen & Woosley, 1999; MacFadyen et al., 2001; Zhang et al., 2003; Gottlieb et al., 2022a,b). Alternatively or in addition, energy may be extracted from the spin-energy of the Kerr BH through the Blandford-Znajek process (Blandford & Znajek, 1977).

These highly asymmetric explosions are associated with the terminal collapse of rapidly spinning progenitors and receive their energy either from a proto-magnetar or accreting Kerr BH. They are considered as explanations of rare kinds of stellar death events with rates well below about 1% of the total CCSN rate, namely long-duration gamma-ray bursts (GRBs), hypernovae (HNe), and the roughly 10 times less frequent superluminous SNe (SLSNe). Such events are characterized by different distinct observational features. For GRBs there is the detection of a flash of gamma rays with energy spectra peaking at hundreds of keV to about one MeV, which points to the presence of ultrarelativistic jets. For HNe explosion energies are diagnosed that are up to 50 times higher than those of canonical CCSNe and seem to be out of reach for neutrino-powered explosions. And for SLSNe observations reveal normal explosion energies but extremely high optical luminosities, which exceed those of all other SN types by at least a factor of 10 during the peak phase of the emission. Long GRBs have been detected with and without hypernovae and hypernovae also without GRBs. Also cases of CCSN explosions with choked jets that cannot make their way to the stellar surface may be possible. These could occur in intermediate explosion cases where the SN blast is mainly driven by neutrino heating but magnetorotational effects do not achieve to produce powerful jets, perhaps because the stellar core does not rotate sufficiently fast and/or the magnetic field configuration is not supportive.

Magnetohydrodynamically driven mass ejection, in particular extremely fast-expanding jets in magnetorotational CCSNe (e.g. Winteler et al., 2012; Nishimura et al., 2015; Cowan et al., 2021, and references therein) and outflows from collapsar disks (Siegel et al., 2019; Siegel, 2022), are discussed as potentially neutron-rich environments that could provide favorable conditions for the production of r-process elements. However, it is still unclear whether and to which extent such phenomena can play a role as rare sources of neutron-capture elements primarily in the low-metallicity universe. Since the production of considerable amounts of iron in such events is hardly avoidable, their ability to inseminate metal-poor stars is at least questionable. Moreover, the neutron excess and hydrodynamic stability of jets in 3D depend extremely sensitively on the conditions in the progenitor star and may require fine-tuned assumptions (Mösta et al., 2018; Halevi & Mösta, 2018; Reichert et al., 2022). Also, collapsar tori had originally been discussed as origins of large amounts of radioactive ^{56}Ni as required by hypernova observations (MacFadyen &

Woosley, 1999), a conjecture that receives support by more recent models including a detailed treatment of neutrino transport (Just et al., 2022).

Currently it is unclear which fraction of CCSNe are caused by the magnetorotational mechanism and which progenitors are involved. There may be a continuum of behaviors, depending on the progenitor’s core rotation and magnetic field, namely mainly (or purely) neutrino-driven explosions, explosions caused by a combination of neutrino and magnetorotational effects, and extreme SNe exploding only because the magnetorotational mechanism provides sufficient energy. Rapid rotation in the stellar iron core with periods of less than ~ 10 s is not expected to be very common, because mass loss in stellar winds leads to the loss of large amounts of angular momentum during advanced stages of the stars’ evolution, slowing down the core rotation when magnetic fields are taken into account to establish an efficient coupling of core and envelope (see, e.g., Heger et al., 2005). This is considered as an argument why white dwarfs are observed to rotate slowly and why pulsars are estimated to have relatively long rotation periods (typically tens to hundreds of milliseconds) at the time of their birth (for a synopsis of such arguments with relevant references, see Janka et al., 2022). Moreover, asteroseismological measurements suggest more spin-down and slower interior rotation of red supergiants than expected from current stellar evolution models including magnetic fields. Together with the finding that CCSNe with energies too high to be explained by the neutrino-driven mechanism (i.e., more than roughly 2×10^{51} erg) are extremely rare, all these facts lead to the conclusion that rapid core rotation does not seem to be widespread among pre-collapse stars. However, binary interaction is thought to affect the progenitors of a major fraction of CCSNe (Sana et al., 2012) and might have an influence on the angular momentum of massive stars prior to core collapse in many ways, potentially spinning their degenerate cores up or down.

2.1.3 Stellar explosions triggered by quark deconfinement

Nuclear phase transitions in dense NS matter are an interesting phenomenon that might occur in Nature and that are relevant for our understanding of the properties of compact stellar remnants and the signals (neutrinos, gravitational waves, nucleosynthesis, explosions) associated with their formation in stellar core-collapse events and their mergers in compact binaries.

For example, phase transitions in PNSs are considered as one possible path to form a stellar-mass BH after a transiently existing NS has released the energy that enables the success of a SN explosion. Alternatively, a NS can also be pushed beyond the mass limit for BH formation by the fallback of larger amounts of matter that is initially accelerated outward but does not achieve to become gravitationally unbound during the SN. The destiny of gravitational instability might also happen to a rapidly rotating NS with a mass that is too large to be stabilized without centrifugal forces. If such a supramassive NS—or hypermassive NS if differential rotation increases its mass even beyond the limit for rigid rotation—loses angular momentum by mass shedding or magnetic field effects, it will become unstable and collapse

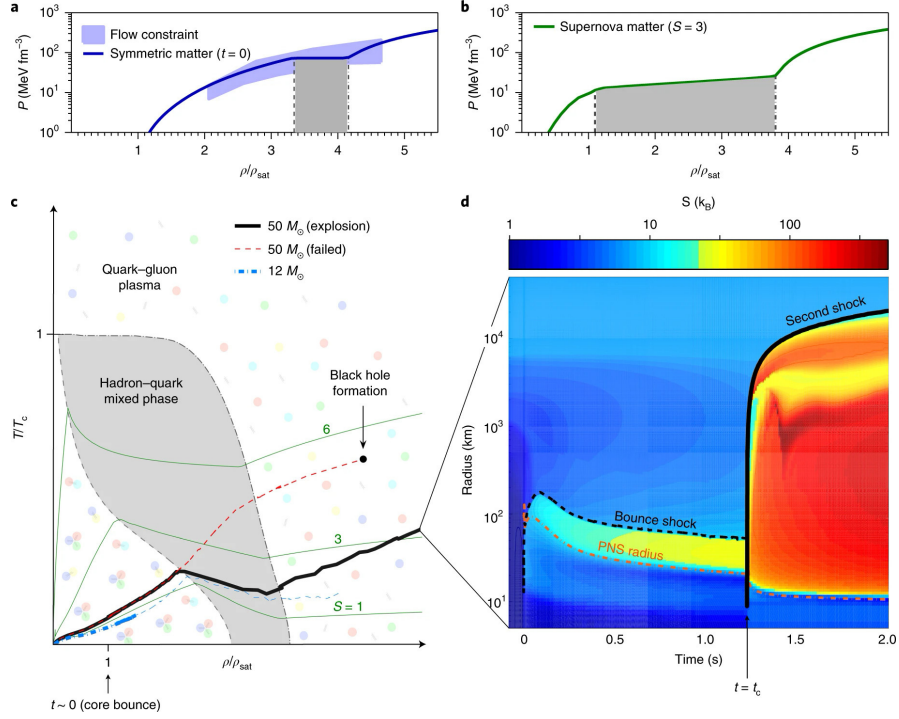


Fig. 3 Hadron-quark phase transition in a PNS and induced SN explosion. The two upper panels display the pressure of the hadron-quark EoS versus density (the latter in units of the nuclear saturation density) for isospin-symmetric matter at zero temperature (*panel a*) and for SN matter of fixed electron fraction ($Y_e = 0.3$) and an entropy per particle of $3 k_B$ (*panel b*). Gray shading marks the density interval of the hadron-quark mixed phase. *Panel c* provides the temperature-density phase diagram of the hybrid EoS with curves of constant entropy indicated by thin solid lines. Also the trajectories of the time-evolving central conditions of three SN models are displayed, with a $50 M_\odot$ model developing an explosion due to the energy release during the collapse from the hadronic PNS to a hybrid star with a compact core of quark-gluon plasma. *Panel d* shows the corresponding space-time diagram, which visualizes the evolution of the PNS radius and core-bounce shock (dashed lines) and the second shock caused by the later (at $t = t_c$) collapse and bounce due to the hadron-quark phase transition (solid black line) (Figure from Fischer et al. 2018; for more details consult this reference; ©Nature Springer. Reproduced with permission)

to a BH. These different scenarios provide routes to BH formation in association with SN explosions and in addition to the “direct” BH formation that occurs when the explosion fails, in which case the temporarily existing PNS continues to accrete mass from the infalling star until it implodes to become a BH (see Figure 1).

Interestingly, it has been shown that a first-order phase transition from nuclear matter to a quark-gluon plasma can also trigger a SN explosion (even in spherically symmetric models that do not account for the supportive effects of hydrodynamic instabilities), if other mechanisms do not succeed (Sagert et al., 2009; Fischer et al., 2018). The energy needed for the explosion is released at the expense of gravita-

tional binding energy when the phase transition sets in and instigates a dynamical collapse of the PNS to a more compact hybrid star with a core of pure quark-gluon plasma. When the quark core settles into a new hydrostatic equilibrium, a bounce shock is formed. This second shock, if propagating out of the compact star, can revive the first shock that is linked to the instant of core bounce when nuclear saturation density was exceeded in the infalling stellar iron core and a PNS began to assemble. Thus a SN explosion can ultimately be launched by the help of the second shock, provided this shock is powerful enough (Figure 3).

However, the exact density regime of the hadron-quark mixed phase, its dependence on temperature and electron fraction in the PNS medium, and the physical properties of the phase transition and of the quark phase are not known. Considerable fine tuning seems to be required in order to create a second shock wave, to obtain sufficient energy release for a viable explosion, and to satisfy the observational lower bounds for the maximum NS mass, too (Fischer et al., 2018; Zha et al., 2021; Jakobus et al., 2022). The first models assumed the hadron-quark phase transition to happen around nuclear saturation density and yielded moderate explosion energies as well as BH formation for compact object masses much below those of the heaviest well-measured NSs. These early models were also in conflict with our understanding of the explosion of SN 1987A and the likely existence of a NS left behind by this SN. Fischer et al. (2018) moved the phase transition to higher densities and their hadron-quark EoS is able to account for the NS mass limit. They could obtain fairly high explosion energies when the phase transition occurred in massive PNSs that did not collapse to BHs before (see Figure 3). In contrast, large model sets with different progenitors and different EoSs with hadron-quark phase transitions showed none (Zha et al., 2021) or very few (two out of 97) and very weak explosions (Jakobus et al., 2022).

In cases where the second shock is formed, the strong bounce connected to the quark-core formation produces a high-amplitude GW signal that lasts for several milliseconds and dominates other contributions to the GW emission of the collapsing star by far (Zha et al., 2020; Kuroda et al., 2022). Moreover, the phase-transition induced collapse and bounce lead to a second, high-luminosity, short-time (of order one millisecond) neutrino burst, followed by pulsational ring-down variations of the luminosities of neutrinos and antineutrinos of all flavors. The emission is dominated by electron antineutrinos produced through positron captures in the previously neutronized PNS matter. Both signals are characteristic of the strong hadron-quark phase transition and are predicted to be measurable for a future Galactic CCSN to provide observational evidence of such an interesting phenomenon in the deep interior of the newly formed compact object. If an explosion is caused by the quark deconfinement, also the production of r-process elements seems possible in rare SN events (Fischer et al., 2020).

2.1.4 Closing remarks

After a successful SN explosion a NS or, more generally, a compact star, is left behind and cools by intense neutrino emission until neutrino-transparent, cool ($T \lesssim 1$ MeV) conditions are reached (e.g., Burrows & Lattimer, 1986; Roberts & Reddy, 2017; Li et al., 2021). During this Kelvin-Helmholtz cooling the gravitational binding energy E_{gb} released in the formation of the compact star is carried away via neutrinos. It is given as a fraction of the mass of the remnant by

$$E_{\nu} \approx E_{\text{gb}} = \frac{0.6\beta}{1-0.5\beta} Mc^2 \quad (5)$$

(fit for non-rotating stars according to Lattimer & Prakash, 2001), where $M = M_0 - E_{\text{gb}}/c^2$ is the gravitational mass of the object with rest mass M_0 , and $\beta = GM/(Rc^2) = R_s/(2R)$ is the compactness parameter for stellar radius R and Schwarzschild radius R_s . Typically, $R \sim (2.5\dots 3)R_s$ and therefore about 10% of the star's rest mass or several 10^{53} ergs are lost in neutrinos.

As mentioned above and graphically represented in Figure 1, during the Kelvin-Helmholtz cooling or during the subsequent evolution, the compact star may collapse to a BH, either due to a phase transition, loss of thermal or angular-momentum support, or fallback accretion, all of which can destabilize the remnant, if the maximum mass determined by the EoS is exceeded. Fallback can not only cause the gravitational implosion of the compact star but it can also bring back the products of SN nucleosynthesis contained in the innermost initial ejecta. Depending on the mass, rotation rate, and magnetic fields of the core-collapse progenitor as well as on the properties of the high-density EoS, a wide spectrum of evolutionary scenarios with or without SN explosions is therefore possible, summarized visually by Figures 1, 2, and 3.

The discussion of SN scenarios and their EoS-dependent nucleosynthesis in this chapter will ignore pulsational pair-instability SNe (PPISNe) and pair-instability SNe (PISNe) (see, e.g., Heger et al., 2003) of the most massive stars with ZAMS masses of roughly more than $70 M_{\odot}$ and $140 M_{\odot}$, respectively (the exact mass boundaries are sensitive to metallicity, stellar mass-loss evolution, reaction rates for 3α and $^{12}\text{C}(\alpha, \gamma)^{16}\text{O}$, and on the stellar rotation). The collapse of such very massive stars is triggered by the onset of electron-positron pair production when the central temperature approaches $\sim 10^9$ K, and their powerful SN eruptions are caused by the energy release from explosive burning of oxygen and silicon. Therefore the high-density super-nuclear EoS does not play a determining role for the nucleosynthesis yields in their ejecta (for the more complex events following the final iron-core collapse in PPISNe, see Powell et al., 2021; Rahman et al., 2022).

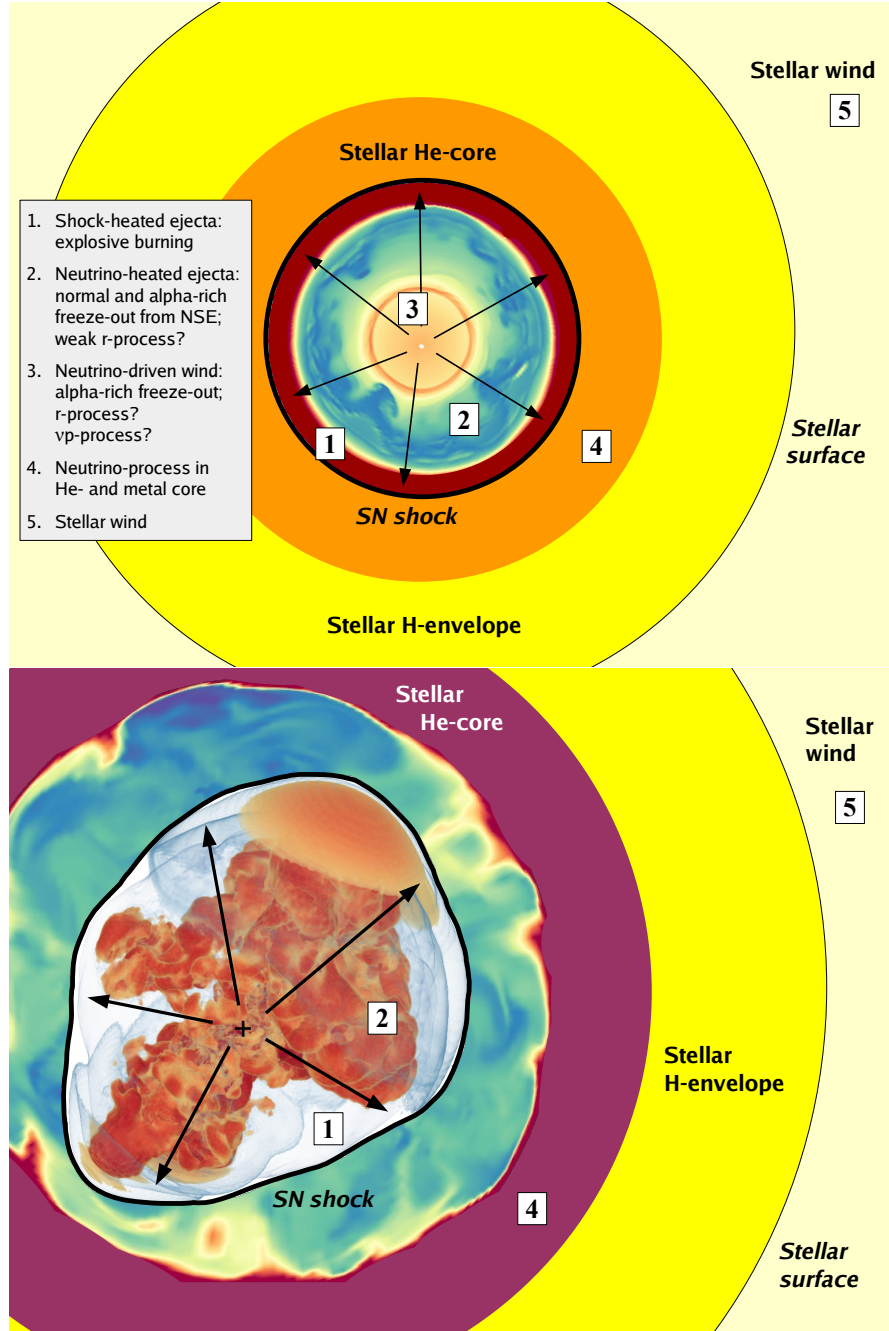


Fig. 4 Regions of different nucleosynthesis processes in ECSN-like explosions of low-mass progenitors ($M_{\text{ZAMS}} \lesssim 10 M_{\odot}$; *top*) and iron-core CCSNe from more massive progenitors (*bottom*). Nuclear burning in shock-heated matter (region 1) creates intermediate-mass elements and contributes to the production of iron-group species; normal and alpha-rich freeze-out from NSE in neutrino-heated postshock matter (region 2) assembles iron-group and trans-iron nuclei; alpha-rich freeze-out in the neutrino-driven mass outflow (“neutrino wind”; region 3) from the new-born NS is discussed as potential site of an r-process and/or neutrino-proton process; neutrino-nucleus reactions in the helium layer and carbon-oxygen core (region 4) can induce the production of various isotopes by the so-called neutrino-process; and the matter lost by the star in a stellar wind (region 5) carries nucleosynthesis products of the sequence of hydrostatic nuclear burning stages prior to core collapse. Note that a neutrino-driven wind (region 3) does not seem to be generic to explosions of massive progenitors. The stellar shells are not drawn to scale

2.2 Ejecta components and nucleosynthesis

SN explosions of massive stars contribute to the nucleosynthesis of chemical elements in the Universe through different parts of their ejecta and by various processes. The regions of nucleosynthesis are visualized in Figure 4 for ECSN-like explosions of low-mass progenitors and for CCSNe of more massive iron-core progenitors (see Section 2.1.1). Mass loss in the stellar wind of the progenitor star (**region 5**) distributes material that the star contained from the time of its formation but also nuclei produced by shell burning and the slow neutron capture process (s-process) and mixed into the outer stellar layers by hydrodynamic processes like convection, dredge-up, and rotation-induced flows (for reviews of the evolution and nucleosynthesis of massive stars and their explosions, see, e.g., Woosley et al., 2002, and a wealth of literature referenced therein).

Nucleosynthesis happening during the SN explosion itself and depending on the conditions in the ejecta as well as in the newly formed NS takes places in regions 1 to 4.

2.2.1 Region 1: shock-heated ejecta

Region 1 contains the products of explosive nuclear burning of silicon, oxygen, neon, and carbon in ejecta that are heated by the outgoing shock. The material in this region retains its pre-collapse electron fraction Y_e , because the collapse and explosion proceed too quickly for weak reactions (electron captures) to have an impact. Assuming that the heat capacity of the plasma behind the shock is dominated by the radiation field and that nearly isothermal conditions hold in the postshock volume, the peak temperature achieved as the shock passes a radius r can be estimated to good accuracy (except for the innermost region close to the PNS) by

$$T_s(r) \approx 1.33 \times 10^{10} \left(\frac{E_{k,\infty}}{10^{51} \text{ erg}} \right)^{1/4} \left(\frac{r}{10^8 \text{ cm}} \right)^{-3/4} \text{ K}, \quad (6)$$

where $E_{k,\infty}$ is the final kinetic energy of the explosion at infinity (Woosley et al., 2002). If the temperature reaches high enough for the nuclear burning time scale to be shorter than the hydrodynamical expansion time scale, explosive nucleosynthesis will modify the pre-explosion composition. Matter heated to 5×10^9 K and higher (typically for $r \lesssim 3000\text{--}4000$ km) will be processed into NSE and become iron-group nuclei during expansion and cooling; silicon burns on a hydrodynamic time scale between 4×10^9 K and 5×10^9 K ($r \lesssim 5000$ km), oxygen between 3×10^9 K and 4×10^9 K, neon between 2.5×10^9 K and 3×10^9 K, and carbon between 1.8×10^9 K and 2.5×10^9 K. At $r \gtrsim 10000\text{--}15000$ km explosive nuclear burning ceases for all elements heavier than helium and explosive processing becomes irrelevant. Therefore these layers are ejected without any appreciable changes of their initial composition; this concerns most elements lighter than oxygen. Also isotopes created by the p-process are expected to be produced in the shock-heated region 1 due to

the partial meltdown of s-process nuclei from the star's helium and carbon burning stages and from the star's original material at birth.

2.2.2 Region 2: neutrino-heated ejecta

Region 2 contains the neutrino-heated ejecta that have absorbed the energy for the explosion via capture reactions of ν_e and $\bar{\nu}_e$ on neutrons and protons, respectively (Eqs. 1 and 2). Different from the layers of region 1, the gas in region 2 falls inward to the close vicinity of the PNS and resides near the gain radius for a while. Thus it can receive the energy needed to expand outward again through the irradiation by the intense neutrino fluxes from the PNS. At the same time ν_e and $\bar{\nu}_e$ absorption, together with their inverse processes (Eqs. 3 and 4), also set the neutron-to-proton ratio that defines the nucleosynthesis conditions when the gas cools during expansion. Neutrino heating raises the entropy of the plasma to high values, for which reason buoyancy triggers convective overturn but also prevents the gas entropy in multi-dimensional simulations to rise as high as it does in spherically symmetric (1D) explosion models (see Figure 5). All matter in this region reaches NSE with the initial nuclei being broken down into free nucleons and α -particles. The nucleosynthesis during the explosive ejection proceeds via alpha-rich freeze-out or normal freeze-out, in which free neutrons and protons recombine to α -particles and heavier nuclei. Because state-of-the-art 2D and 3D CCSN simulations with detailed neutrino transport show that a dominant fraction of these ejecta obtains a proton excess (see Figures 5 and 6), proton-rich isotopes of light trans-iron elements, in particular ^{92}Mo , can be produced besides iron-group nuclei including an appreciable amount of ^{56}Ni , which adds to the ^{56}Ni assembled in region 1 (see Wanajo et al., 2018, for results from 2D models).

An interesting difference exists between ECSN-like explosions and CCSNe. In the former ones the earliest ejecta expand very quickly behind the SN shock, which accelerates and propagates much more rapidly than in the CCSNe of more massive progenitors. Therefore the exposure of the ejected material to the ν_e and $\bar{\nu}_e$ fluxes from the PNS is much shorter and they are able to retain a higher neutron excess, closer to the neutron-rich state that the gas had near the minimum radius that it reached during its infall (see Figure 7, upper panels). Compared to CCSNe, ECSN-like events therefore eject significantly more neutron-rich matter with lower minimum values of Y_e (Figure 8). Therefore they can contribute considerably to the production of trans-iron species from Zn to Zr and could be relevant sources of neutron-rich radioactive isotopes such as ^{48}Ca and ^{60}Fe and possibly also of elements beyond $N = 50$ made by a weak r-process reaching up to Pd, Ag, and Cd (Wanajo et al., 2011, 2013a,b).

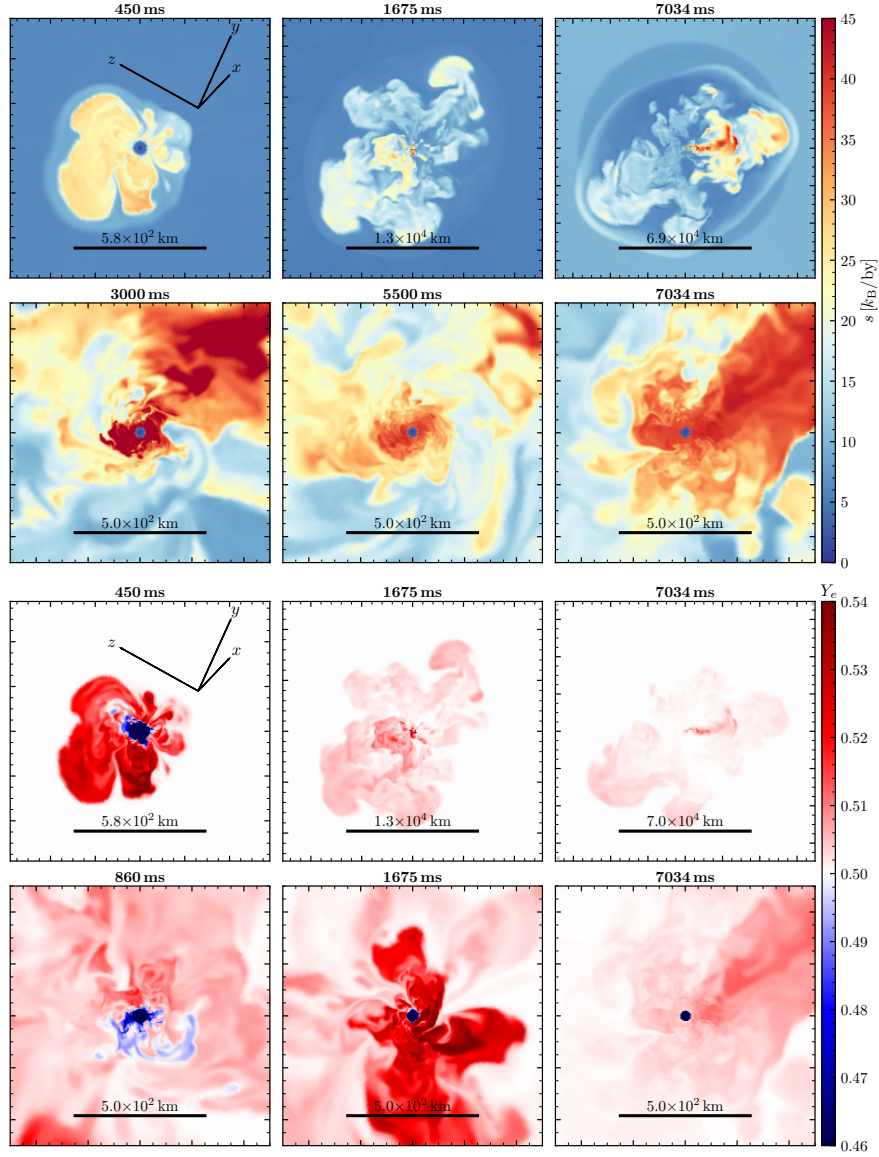


Fig. 5 Entropy (*top*) and electron fraction Y_e (*bottom*) distributions in cross-sectional cuts at six post-bounce times of a 3D CCSN simulation of a $19 M_{\odot}$ progenitor, whose explosion sets in at about 0.4 s after bounce. Note the different length scales indicated by yard sticks and the different times specified above the panels. The lower panels show close-ups of the turbulent vicinity of the PNS. They display lower-entropy downflows and high-entropy outflows of neutrino-heated matter until more than 7 s after bounce. A spherical neutrino-driven wind of neutrino-heated matter blown off the PNS surface does not develop until that time (Figure from Bollig et al. 2021; ©American Astronomical Society. Reproduced with permission)

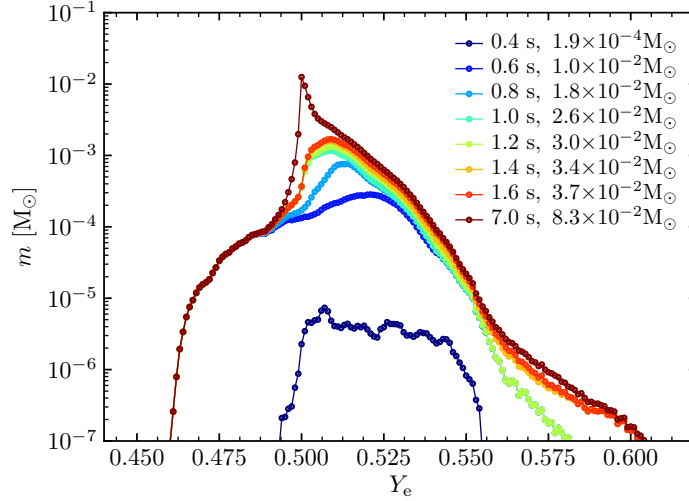


Fig. 6 Cumulative mass distributions of the ejecta as functions of Y_e until different post-bounce times (the integrated ejecta mass is given by the labels) for a 3D CCSN simulation of a $19 M_\odot$ progenitor (Figure from Bollig et al. 2021; ©American Astronomical Society. Reproduced with permission)

2.2.3 Region 3: neutrino-driven wind

Region 3 is the neutrino-driven wind (or “neutrino wind”), which is a low-density outflow of baryonic matter from the surface layers of the hot PNS. The neutrino emission during the Kelvin-Helmholtz cooling of the PNS does not permit a hydrostatic atmosphere, but neutrino heating exterior to the neutrinosphere, mainly by ν_e and $\bar{\nu}_e$ absorption of Equations (1) and (2) and on a lower level also by neutrino-electron scattering and neutrino-antineutrino pair annihilation, leads to mass loss through such a wind (see Duncan et al., 1986; Woosley & Baron, 1992; Wittl et al., 1994; Qian & Woosley, 1996; Otsuki et al., 2000; Thompson et al., 2001, and references therein). This outflow of matter is quasi-stationary, i.e., slowly evolving with time, and quasi-spherical for non-rotating or slowly rotating PNSs. Qian & Woosley (1996) provided analytic expressions for the important wind properties, assuming steady-state conditions in the wind. The mass loss rate is approximately given by

$$\dot{M} \approx 6 \times 10^{-4} L_{\text{tot},53}^{5/3} \epsilon_{\nu_e,15}^{10/3} R_6^{5/3} M_{1.4}^{-2} M_\odot \text{ s}^{-1}, \quad (7)$$

the asymptotic wind entropy for radiation-dominated conditions is

$$s \approx 15 + 50 L_{\text{tot},53}^{-1/6} \epsilon_{\nu_e,15}^{-1/3} R_6^{-2/3} M_{1.4} k_B \text{ per nucleon}, \quad (8)$$

and the expansion timescale of the wind with velocity v at radius r where the temperature has dropped to 0.5 MeV is

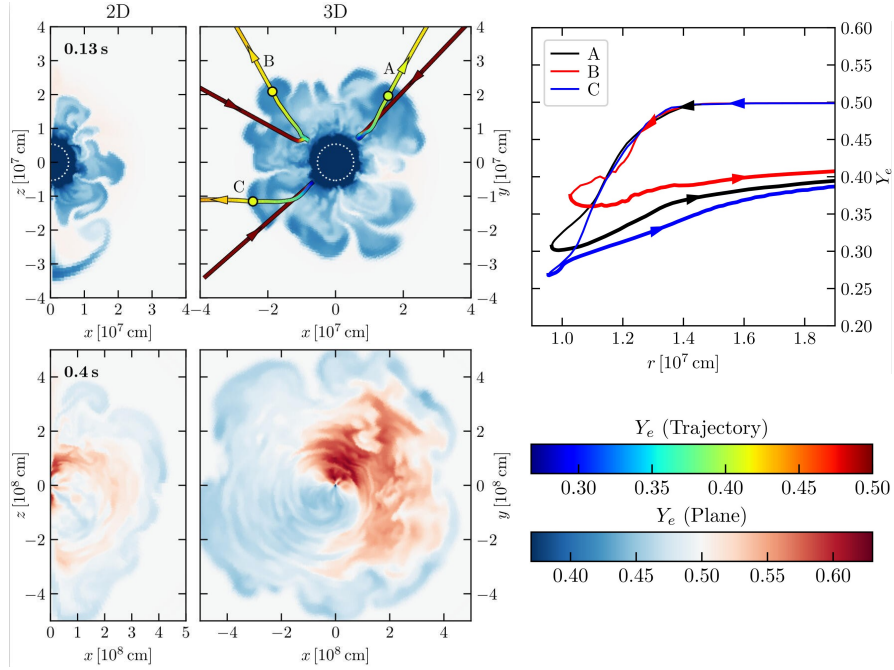


Fig. 7 Neutron-rich, fast, early ejecta (*upper panels*) and LESA-induced hemispheric asymmetry of the electron fraction in the neutrino-driven wind ejecta (*bottom left*) of an ECSN-like explosion of a $9.6 M_{\odot}$ progenitor. The *left panels* display cross-sectional cuts of 2D and 3D explosion models (color coding according to the color bar on the *bottom right*). The *upper right panel* shows the evolution of Y_e along three representative inflow-outflow trajectories for the earliest, neutron-rich ejecta in the 3D model as indicated in the *upper left panel* (Figure from Stockinger et al. 2020; ©Oxford University Press on behalf of the Royal Astronomical Society (RAS). Reproduced with permission)

$$t_{\text{dyn}} \equiv \left. \frac{r}{v} \right|_{T \approx 0.5 \text{ MeV}} \approx 6 \times 10^{-3} L_{\text{tot},53}^{-1} \varepsilon_{\nu_e,15}^{-2} R_6 M_{1.4} \text{ s}. \quad (9)$$

Here $L_{\text{tot},53}$ denotes the total neutrino luminosity (i.e., the sum of the contributions of neutrinos and antineutrinos of all flavors) in units of $10^{53} \text{ erg s}^{-1}$, R_6 the PNS radius in 10^6 cm , $M_{1.4}$ the PNS mass in $1.4 M_{\odot}$, and $\varepsilon_{\nu_e,15}$ is the ratio of neutrino spectral moments, defined as $\varepsilon_{\nu} \equiv \langle E_{\nu}^2 \rangle / \langle E_{\nu} \rangle$, for electron neutrinos in units of 15 MeV (the angle brackets denote spectral averages of powers of the neutrino energies E_{ν}).

The neutrino-driven wind is a generic feature of spherically symmetric (1D) simulations, where explosions have to be triggered artificially in most cases. However, it is witnessed in self-consistent, state-of-the-art 3D simulations only for the low-energy ECSN-like explosions (upper panel of Figure 4). The low-mass progenitors of ECSN-like events possess extremely steep density gradients exterior to their degenerate cores and correspondingly very low mass-infall rates (Stockinger et al., 2020). Therefore the quickly expanding shock immediately reverses their collapse to outflow and creates a low-density bubble around the PNS, into which the wind can

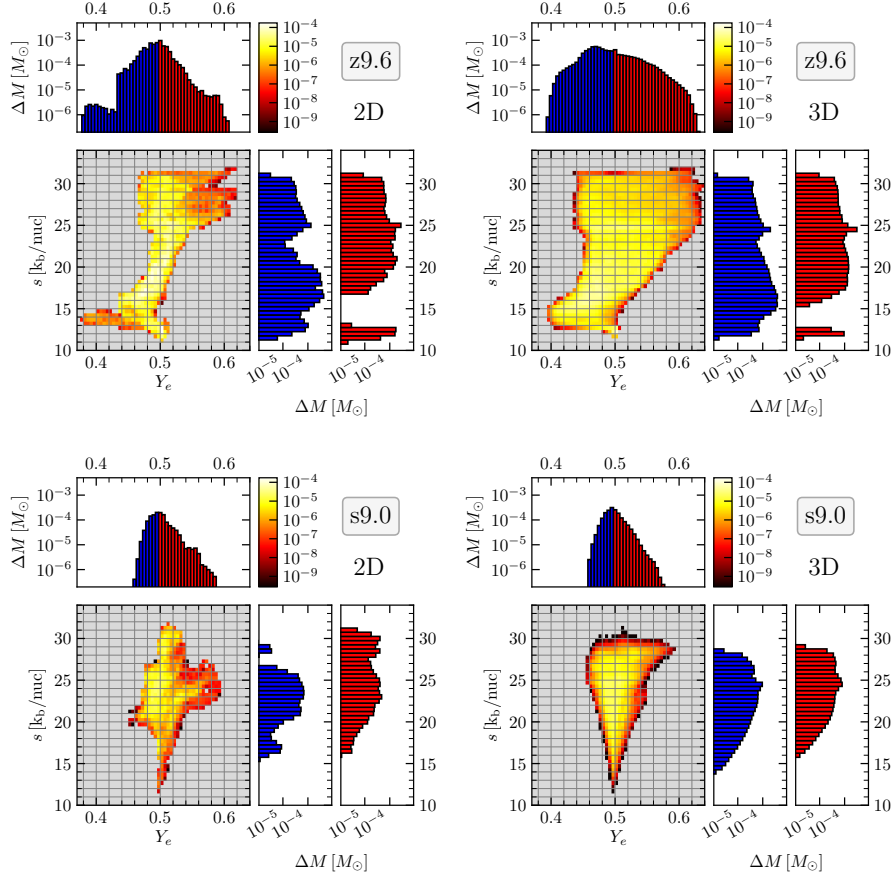


Fig. 8 Mass distributions of ejecta as functions of Y_e and entropy per nucleon, s (in units of Boltzmann’s constant), for 2D (*left*) and 3D (*right*) simulations of an ECSN-like explosion of a zero-metallicity $9.6 M_\odot$ progenitor (*top*) and a CCSN explosion of a solar-metallicity $9 M_\odot$ progenitor (*bottom*). Both progenitors have developed iron cores prior to collapse. The central panels in each case display the mass distribution in the Y_e - s -plane (colour coding in units of M_\odot according to the colour bar). The corresponding panels above and to the right show the marginal distributions with blue and red bars indicating $Y_e < 0.5$ and $Y_e > 0.5$, respectively. Considerably more neutron-rich matter is ejected due to the fast expansion of the ECSN-like explosion (Figure from Stockinger et al. 2020; ©Oxford University Press on behalf of the RAS. Reproduced with permission)

expand freely. In contrast, in CCSNe of more massive stars with higher mass-infall rates a neutrino-driven wind does not develop until many seconds after the onset of the explosion (Bollig et al., 2021). Instead, in those cases long-lasting accretion downflows reach down to the close vicinity of the PNS during all of this long period of post-bounce evolution (Figure 5). The downdrafts are supplied with matter swept up by the outgoing SN shock. Because of their heavy mass loading they remain intact when they dive inward towards the PNS and return outward only after having

absorbed enough energy from the intense neutrino fluxes to become buoyant. Thus they increase the blast-wave energy to values of order 10^{51} erg as needed to explain observed energies of canonical CCSNe (see Müller et al., 2017; Bollig et al., 2021, and Section 2.1.1).

As in region 2, the charged-current β -processes of Eqs. (1)–(4) set the Y_e in the neutrino-driven wind of region 3. However, because of the low densities (high entropies) and rapid expansion cooling of the wind, the absorption reactions of ν_e and $\bar{\nu}_e$ dominate quickly over the inverse processes. If the ν_e and $\bar{\nu}_e$ capture rates on nucleons (Eqs. 1 and 2) are in equilibrium, the asymptotic electron fraction Y_e in the wind can be estimated as (Qian & Woosley, 1996)

$$Y_e \approx \left[1 + \frac{L_{\bar{\nu}_e} \varepsilon_{\bar{\nu}_e}}{L_{\nu_e} \varepsilon_{\nu_e}} Q(\varepsilon_{\nu_e}, \varepsilon_{\bar{\nu}_e}) C(\varepsilon_{\nu_e}, \varepsilon_{\bar{\nu}_e}) \right]^{-1}, \quad (10)$$

where L_{ν_i} is the luminosity of neutrino species ν_i and ε_{ν_i} is again the ratio of neutrino spectral moments, $\varepsilon_{\nu_i} \equiv \langle E_{\nu_i}^2 \rangle / \langle E_{\nu_i} \rangle$. The factors $Q(\varepsilon_{\nu_e}, \varepsilon_{\bar{\nu}_e})$ and $C(\varepsilon_{\nu_e}, \varepsilon_{\bar{\nu}_e})$ in the denominator of this expression depend on the mean neutrino energies; Q is a correction factor that accounts for the neutron-proton mass difference, $\Delta = 1.29$ MeV, in the β -reactions, and C contains corrections due to nucleon recoil and weak magnetism effects (Horowitz & Li, 1999; Horowitz, 2002). These factors can be conveniently approximated by

$$Q(\varepsilon_{\nu_e}, \varepsilon_{\bar{\nu}_e}) \approx \frac{1 - 2\Delta/\varepsilon_{\bar{\nu}_e} + 1.2(\Delta/\varepsilon_{\bar{\nu}_e})^2}{1 + 2\Delta/\varepsilon_{\nu_e} + 1.2(\Delta/\varepsilon_{\nu_e})^2}, \quad (11)$$

$$C(\varepsilon_{\nu_e}, \varepsilon_{\bar{\nu}_e}) \approx \frac{1 - 8.66 \varepsilon_{\bar{\nu}_e}/(mc^2)}{1 + 1.22 \varepsilon_{\nu_e}/(mc^2)}, \quad (12)$$

with m being the nucleon mass. The absorption of ν_e and $\bar{\nu}_e$ in the ejecta drives Y_e to the neutron-rich side, i.e., $Y_e < 0.5$, if $L_{\bar{\nu}_e} \varepsilon_{\bar{\nu}_e} \cdot C \cdot Q > L_{\nu_e} \varepsilon_{\nu_e}$. If one ignores the factor C , considers only the linear dependence of Q on $\Delta/\varepsilon_{\nu_e}$, and assumes $L_{\bar{\nu}_e} = L_{\nu_e}$, for example, one finds the condition $\varepsilon_{\bar{\nu}_e} > \varepsilon_{\nu_e} + 4\Delta$. This means that electron antineutrinos need to be emitted by the PNS with significantly harder spectra.

In early numerical models the neutrino-driven wind was found to reach entropies of several $100 k_B$ per nucleon and Y_e values well below 0.4 after several seconds, both with trends to more extreme conditions (higher entropies and higher neutron excess) at later times (Woosley et al., 1994). Therefore the wind environment has been discussed as possible site of r-process nucleosynthesis for more than a decade (e.g., Takahashi et al., 1994; Hoffman et al., 1997; Otsuki et al., 2000; Arnould et al., 2007, and references therein). However, modern, more elaborate SN and PNS cooling simulations with better neutrino transport showed that PNS winds do not reach sufficiently high entropies and also remain proton-rich instead of developing a large neutron excess (e.g., Hühdepohl et al., 2010; Fischer et al., 2010; Roberts et al., 2010; Mirizzi et al., 2016, and references therein), at least when strong magnetic fields and rapid rotation do not play a relevant role in the PNS. Interestingly, in proton-rich ejecta, in particular in those of the neutrino-driven wind but potentially

also in the neutrino-processed early ejecta of region 2, a νp -process might take place when the proton-rich matter is exposed to intense neutrino fluxes. Such a possibility requires that the entropy is sufficiently high and the expansion time scale is long enough to permit an efficient conversion of protons to neutrons by frequent $\bar{\nu}_e$ absorption reactions (Fröhlich et al., 2006; Pruet et al., 2006; Wanajo, 2006; Arcones et al., 2012; Wanajo et al., 2018).

2.2.4 Region 4: preshock helium shell and metal core

Region 4 denotes the helium shell and the different layers (Si, O/Ne, C) of the metal core prior to the passage of the outgoing SN shock. Well before the shock reaches these shells, which can take many seconds to minutes for the outermost of the mentioned layers, the huge fluxes of neutrinos and antineutrinos of all flavors emitted by the PNS irradiate the nuclei in these regions. This bombardment can cause interesting transmutations via neutrino-induced reactions (Domogatsky & Nadyozhin, 1977; Woosley, 1977; Domogatskii & Nadezhin, 1978, 1980; Woosley & Haxton, 1988; Woosley et al., 2002), mainly through charged-current (of ν_e and $\bar{\nu}_e$) and neutral-current excitation of nuclei that subsequently decay by the emission of light particles (neutrons, protons, α -particles). Thus rare isotopes, e.g., ^{11}B , ^{19}F , ^{138}La , and ^{180}Ta , can be produced directly by the neutrino interactions with abundant target nuclei, and, in addition, the increased abundance of light particles can lead to the nucleosynthesis of some species such as ^7Li and ^{26}Al through a network of charged-particle reactions. Of course, when the shock passes through the outer layers, the neutrino-processed abundances will experience some reprocessing by the shock, which has to be taken into account in detailed calculations (Woosley et al., 1990).

For recent results, accounting for the latest understanding of neutrino-nucleus cross sections and the crucial neutrino properties, i.e., the time-dependent luminosities and spectra of all emitted neutrino species, deduced from state-of-the-art CCSN models, see Sieverding et al. (2018) and, in particular, Sieverding et al. (2019). Since the production of key species by the neutrino process requires neutrino energies that are high enough to facilitate neutrino-nucleus interactions and nucleus excitation, the efficiency of this process is very sensitive to the spectral temperature of the neutrinos. The synthesis of isotopes through the ν -process is therefore a potential thermometer for the neutrinos emitted by CCSNe.

2.2.5 Closing remarks

Naturally, all the nucleosynthesis and the dissemination of its products in regions 1–4 hinge on the success of the CCSN explosion. This implies that the nuclear EoS should not lead to fast BH formation but instead it must allow for ample energy release by neutrinos and/or magnetorotational effects involving a sufficiently long-

lived PNS. Alternatively, it could mean that a hadron-quark phase transition releases enough energy to trigger the explosion, implying special EoS properties.

More specifically, the EoS has a significant influence on the characteristic features of the neutrino emission by the PNS. These, in turn, are crucial for the neutrino heating and thus for the viability of the neutrino-driven mechanism. Also the blast-wave energy of the SN explosion, which determines the nucleosynthesis in region 1, depends on the time evolution of the neutrino luminosities and spectra. The same holds true for the efficiency of the neutrino process in region 4; and it also holds true for the neutron-to-proton ratio in the neutrino-heated ejecta (region 2) and for the conditions (Y_e , entropy, expansion velocity) in the neutrino-driven wind (region 3). Therefore, since the nuclear EoS controls the cooling and deleptonization of the PNS from its hot and proton-rich initial state to the final, cold compact remnant, it is also of great importance for the nucleosynthesis in CCSNe.

The next section will elaborate on these aspects.

2.3 Role of the equation of state

Over decades, a large number of works has investigated the influence of the high-temperature nuclear and super-nuclear EoS on the mass limit when PNSs collapse to BHs (e.g., Keil & Janka, 1995; O’Connor & Ott, 2011; Steiner et al., 2013; da Silva Schneider et al., 2020), on the neutrino emission prior to and after the CCSN explosion (e.g., Pons et al., 1999, 2001; Marek et al., 2009; O’Connor & Ott, 2013; Schneider et al., 2019b; Sumiyoshi et al., 2019; Nakazato & Suzuki, 2019, 2020; Reed & Horowitz, 2020), and on the GW signals from the death events of massive stars (e.g., Marek et al., 2009; Zha et al., 2020; Eggenberger Andersen et al., 2021; Kuroda et al., 2022). The relevant literature cannot be comprehensively listed here. Many of the mentioned studies —except those for GW predictions— were done in 1D, because corresponding codes are publicly available and because such calculations are relatively inexpensive and can be performed for large sets of models, thus systematically exploring parameter dependencies, for example on the nuclear saturation density, isoscalar incompressibility modulus, symmetry energy, and effective mass of nucleons. However, although basic sensitivities of the considered phenomena to variations of the nuclear inputs may be carved out, 1D results can also be highly misleading, quantitatively as well as qualitatively. Therefore they can provide only limited information on the behavior of more realistic, multi-dimensional systems and the real phenomena in Nature (examples will be discussed below). Conclusive results that are valid for astrophysical interpretation are not abundantly available as yet. In particular, such results are still missing w.r.t. the question how CCSN nucleosynthesis depends on the EoS of PNS matter. Little research has been done on this problem so far.

Figure 9 provides an overview of the EoS constraining parameter values of density, temperature, and electron fraction Y_e (minimum and maximum values) that were obtained during different phases and in different regions of a collapsing

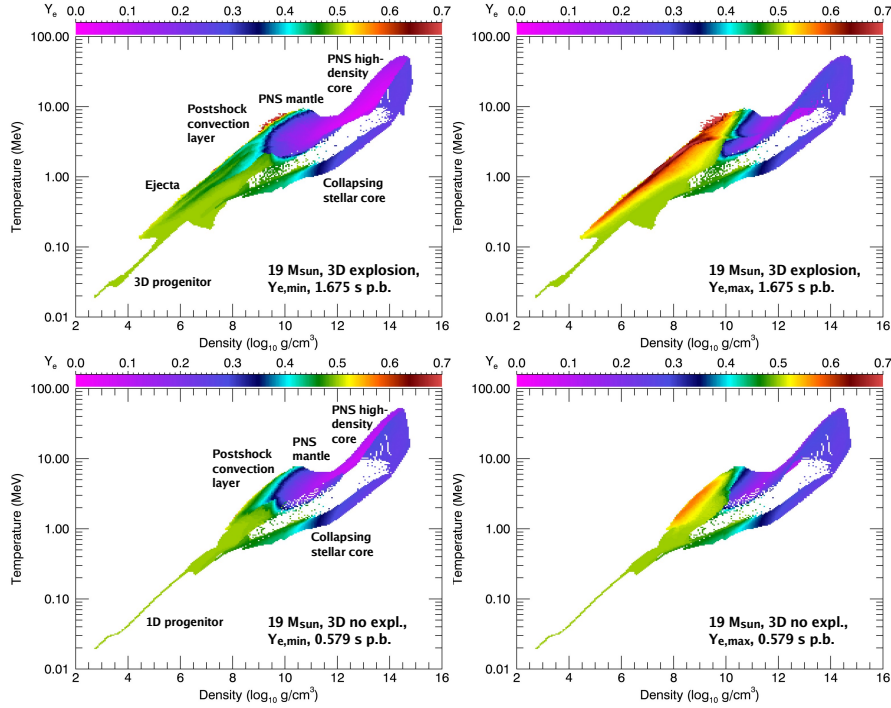


Fig. 9 Overview of thermodynamically relevant conditions in CCSNe by means of the minimum (*left*) and maximum (*right*) values of the electron fraction (Y_e) as functions of density and temperature in successfully exploding (*top*) and non-exploding (*bottom*) 3D simulations of a $19 M_{\odot}$ progenitor (Bollig et al., 2021) with the LS220 EoS (Lattimer & Swesty, 1991). The two 3D CCSN calculations were evaluated for the entire evolution periods until the post-bounce times mentioned in the panels. Note that the empty region between the conditions in the interior of the PNS and the conditions in the collapsing stellar core as well as the high-density, low-temperature region below the stellar core-collapse branch will be filled during the neutrino-cooling evolution of the PNS (Figure courtesy of Robert Bollig)

$\sim 19 M_{\odot}$ progenitor star, its newly formed NS, and the ejecta of its CCSN explosion. These 3D simulations led to successful neutrino-driven explosions when they were started from the 3D pre-collapse structure of the progenitor, thus taking into account the density and velocity perturbations in the convective oxygen-burning shell, but they ended in failed explosions when the initial conditions were taken from 1D progenitor profiles (Bollig et al., 2021). The stellar core is characterized by low-entropy, low-temperature conditions in the infall phase, the core of the PNS (above a density of roughly $10^{13} \text{ g cm}^{-3}$) and the mantle region of the PNS (above a density of several $10^{10} \text{ g cm}^{-3}$) develop low electron fractions, the convective postshock layer (above about 10^8 g cm^{-3}) exhibits a mix of low- Y_e and high- Y_e matter in low-entropy accretion downflows and high-entropy buoyant plumes, respectively. The neutrino-heated CCSN ejecta stick out by their high temperatures and entropies

and by Y_e values ranging from close to 0.5 to considerably higher numbers (see also Figure 6).

The main topic of this section is the question how the properties of these ejecta and the associated nucleosynthesis are connected to the properties of the high-density EoS inside the PNS. This interesting problem is only superficially and fragmentarily explored, because only very few self-consistent, first-principle SN simulations, in particular in 3D, have so far been carried out with different high-density EoS models. Moreover, in order to study the impact on the chemical element production, the explosion simulations need to be followed to sufficiently late times to determine all ejecta components and to follow them through the density-temperature regime that is relevant for the nucleosynthesis. The discussion of this section can therefore only highlight some essential connections between the EoS-dependent PNS properties, the corresponding neutrino emission, and the explosion and ejecta conditions that hinge on the physics playing a role in the center of the SN blast.

2.3.1 Neutron excess in early ejecta of ECSN-like explosions

In Section 2.2.2 it was mentioned that the neutron-to-proton ratio in neutrino-heated ejecta differs considerably between ECSN-like explosions and CCSNe of more massive progenitors. The ejecta expand more slowly in the latter events and therefore frequent absorptions of ν_e and $\bar{\nu}_e$ lead to an increase of Y_e from pre-ejection conditions of $Y_e \ll 0.5$ to values around 0.5 and even higher. Most of the CCSN ejecta therefore possess $Y_e \gtrsim 0.5$ (Figures 6 and 9 and Wanajo et al., 2018). In contrast, the extremely fast expansion of the SN shock and of the earliest ejecta in ECSN-like explosions permits this matter to retain a considerable neutron excess with Y_e possibly as low as 0.35, which could enable the formation of light r-process elements up to the palladium and silver region; see Section 2.2.2, Figures 7 and 8, and references Wanajo et al. (2011), Wanajo et al. (2018), and Stockinger et al. (2020).

The mass distribution of Y_e in the ejecta of ECSN-like explosions depends on the dimension of the simulations: expelled material with $Y_e < 0.45$ is not present in 1D models (Wanajo et al., 2011; Zha et al., 2022). Also the details of the core structure of the progenitor (e.g., whether it was computed in 1D or multi-D) has some noticeable influence, in particular on the question whether a small amount of matter is expelled with $0.35 \lesssim Y_e \lesssim 0.40$ (Zha et al., 2022). This last aspect is also sensitive to the nuclear EoS applied in the core-collapse and explosion modeling, because the ejection of the fastest material hinges extremely sensitively on the subtleties of the early postbounce dynamics of the SN shock and on the rapid development of convective overturn in the postshock layer. Also the details of the neutrino emission in the first 100–150 milliseconds after core bounce have an influence on the Y_e distribution in the quickly expanding, buoyant plumes (Figure 10). This was witnessed by von Groote (2014) in general relativistic 2D simulations with state-of-the-art neutrino transport when considering a small sample of different EoSs for the hot PNS medium. More investigations of this aspect with larger sets of EoS models are desirable.

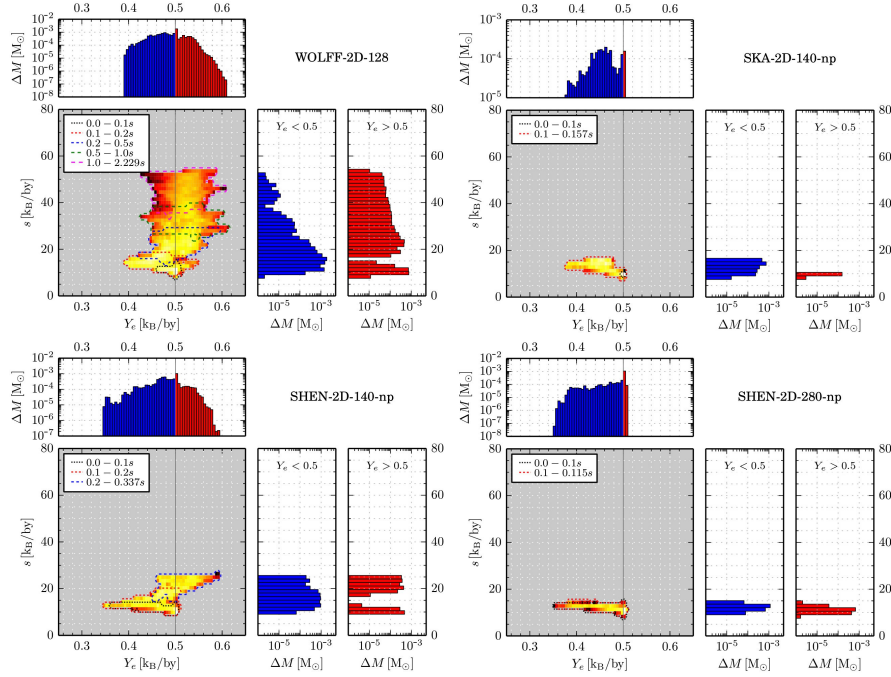


Fig. 10 Mass distributions of ejecta as functions of Y_e and entropy per nucleon s , plotted similarly to Figure 8, for 2D simulations of ECSN explosions of an $8.8 M_\odot$ ONeMg-core progenitor (von Groote, 2014) with three different nuclear EoS: STOS (labelled SHEN) of Shen et al. (1998, 2011), WOLFF of Hillebrandt et al. (1984) and Hillebrandt & Wolff (1985), and LS-SKa (labelled SKA; Lattimer & Swesty, 1991, J. Lattimer, 2009, private communication; EoS tables available at <http://www.astro.sunysb.edu/lattimer/EOS/main.html>). The time evolution is visualized by dashed and dotted lines of different colors in the Y_e - s -plane, which indicate matter that is ejected in different time intervals. This shows that the most neutron-rich material is expelled earliest. Except for the simulation with the WOLFF EoS, the models were carried only to the onset of the explosion to identify the most neutron-rich ejecta. Fast-moving, early ejecta with $0.35 \lesssim Y_e \lesssim 0.40$, which are expelled in rising convective plumes during the first 100–150 ms after core bounce, exhibit a clear sensitivity to the nuclear EoS, whereas the angular resolution (1.286° versus 0.643° lateral zone size with 140 and 280 equidistant angular zones in the range $[0^\circ, 180^\circ]$, respectively) has no crucial effect on the minimum value of Y_e (*lower panels*) (Figure courtesy of Janina von Groote)

2.3.2 Relevance of the proto-neutron star radius

In order to have astrophysical consequences, microscopic EoS properties must lead to macroscopic effects in CCSNe. The radius evolution of the hot PNS after core bounce, which depends on the nonzero-temperature EoS, is one example of such a macroscopic influence of relevance for the SN evolution. Early 2D simulations of stellar core collapse and the neutrino-driven mechanism using a state-of-the-art treatment of neutrino transport and different prescriptions for the nuclear EoS suggested that a faster contraction of the PNS facilitates shock revival by neutrino heating and the onset of an explosion (Janka, 2012). This result was confirmed with a

more approximate description of the neutrino physics by Suwa et al. (2013). The basic reason is that stronger PNS contraction releases compression work, which heats the PNS mantle layer and leads to higher virial temperatures at the neutrinospheres of all neutrino species. Moreover, because of the steepening density gradient near the PNS surface, the neutrinospheres move to smaller radii. These effects in combination permit higher luminosities and harder spectra of the emitted neutrinos, both of which enhance the energy deposition by neutrinos in the gain layer behind the stalled shock. Therefore, if the PNS contracts faster, an explosion can set in more easily and earlier. This behavior is a generically multi-dimensional phenomenon, because in 1D the faster contraction of the PNS leads to stronger recession of the stagnating shock, despite more neutrino energy deposition by the higher luminosities and mean energies of the radiated neutrinos (Janka, 2012). In contrast, in the multi-dimensional case, the enhanced neutrino heating stirs more violent postshock convection (Murphy et al., 2013). The associated buoyancy (“turbulent”) pressure (Müller & Janka, 2015) pushes the shock farther out. This expansion of the shock increases the gain layer and thus facilitates a positive feedback for even more neutrino heating, enabling outward shock acceleration in a runaway process.

Latest 3D CCSN simulations with modern NS EoSs that are fully compatible with the observational constraints for NS radii and maximum NS mass reviewed in Section 1, support this tight correlation between the PNS radius evolution and the onset of the explosion (for the case of a $\sim 19 M_{\odot}$ star, see Figure 11, and also see Bollig et al., 2021, for a subset of published models). Remarkably, successful neutrino-driven explosions were obtained with all nuclear EoSs tested in the CCSN models, provided these simulations were started with 3D progenitor data, i.e., the initial conditions were adopted from 3D calculations of convective oxygen-shell burning during the last minutes before the core of the progenitor undergoes gravitational collapse (Yadav et al., 2020; Bollig et al., 2021). Corresponding 3D CCSN simulations using 1D progenitor data did not yield explosions in any of the considered cases.

Remarkably, 1D SN simulations with a parametric treatment for the time evolution of the turbulent kinetic energy associated with neutrino-driven convection (Boccioli et al., 2022) reveal major qualitative and quantitative differences compared to the 3D results of Figure 11. The 1D results of Boccioli et al. (2022) exhibit a different ordering of the “explodability” with varied EoS, for example they show only slow explosions for the SFHo EoS and none for the DD2 EoS, in contrast to the 3D models of Figure 11. These discrepancies are a warning that such 1D calculations should be taken with great caution. They do not only ignore the 3D nature of pre-collapse convection in the progenitors, but they also attempt to describe the effects of non-stationary, anisotropic, non-radial, large-scale and large-amplitude variations in convective down- and outflows in the postshock layer by time-dependent equations for averaged turbulent quantities in a linear approximation, using a mixing-length-theory (MLT) approach for the energy flux. Such approximations in spherically symmetric models oversimplify the physics of postshock turbulence in the non-perturbative regime in an uncontrolled manner. Moreover, the employed 1D treatment does not even conserve energy globally (Müller, 2019; Boccioli et al.,

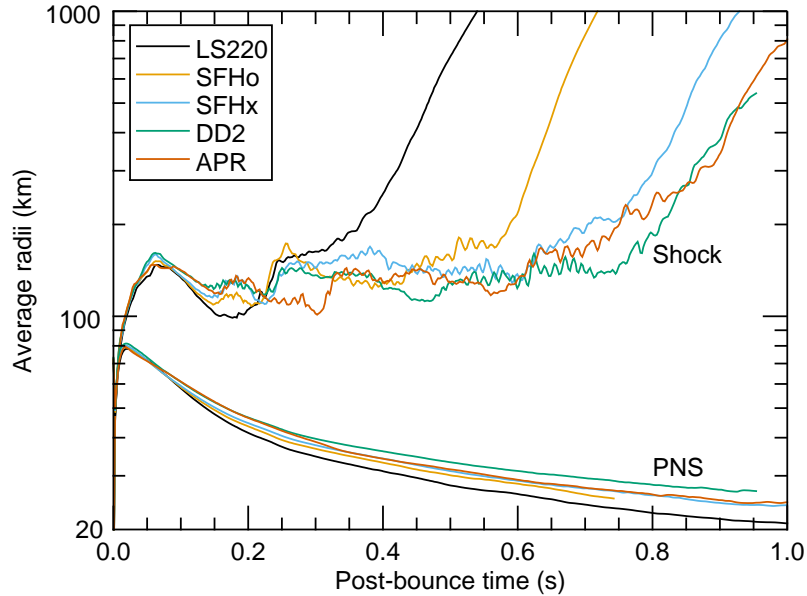


Fig. 11 Shock radii and PNS radii (spherically averaged) in 3D simulations of CCSN explosions of a $19 M_{\odot}$ progenitor for different nuclear EoSs widely used in SN simulations: LS220 of Lattimer & Swesty (1991), SFHo, SFHx of Steiner et al. (2013) and Hempel & Schaffner-Bielich (2010), DD2 of Typel et al. (2010); Hempel et al. (2012), and APR of Schneider et al. (2019a). In all cases successful explosions were obtained in 3D core-collapse simulations started from 3D progenitor conditions (Yadav et al., 2020; Bollig et al., 2021), but there is a clear correlation between the onset of the explosion and the contraction of the PNS. The faster the PNS contracts, the earlier the explosion sets in. This signals the dominant relevance of the PNS radius evolution over other EoS dependent effects (Figure courtesy of Robert Bollig)

2021), and its results depend highly sensitively on the values of the parameters used in the evolution equation for the turbulent energy. There is no guarantee, for example, that MLT parameter values adjusted by comparison to a specific 3D CCSN simulation are valid also for models with different progenitor masses and different nuclear EoSs.

The pivotal importance of the PNS radius evolution for the onset of explosion is mediated by a tight connection between the neutrino emission properties and the PNS radius as described above. This physical link was also witnessed when muons were included in the EoS of the hot PNS medium and in the neutrino transport, which caused a softening of the high-density EoS due to the production of additional particles with considerable rest mass (Bollig et al., 2017). And it was again found when strange-quark contributions to the nucleon spin were included in the neutral-current neutrino scattering rates with neutrons and protons (Melson et al., 2015). The overall effect of the latter modification was only on the order of 10% in a single reaction of neutrinos with the nucleons in the stellar plasma, leading to easier escape of muon and tau neutrinos and antineutrinos from the PNS. This causes a faster con-

traction of the PNS, a corresponding temperature rise in the neutrinospheric region also of electron neutrinos and antineutrinos, and thus again to more postshock heating by ν_e and $\bar{\nu}_e$ that leave the neutrinosphere and undergo a final charged-current interaction behind the SN shock through the β -processes of Eqs. (1) and (2). Although the influence of strange-quark corrections in the neutrino-nucleon scattering rates was assumed to be on the extreme side compared to the latest experimental and theoretical limits for such an effect, the 3D CCSN simulations by Melson et al. (2015) nevertheless demonstrated that such a moderate change in the neutrino opacities was sufficient to convert a failed $20 M_\odot$ CCSN explosion into a successful one.

In fact, the effective mass of nucleons at densities above roughly 10% of the nuclear saturation density was shown to have a strong influence on the radius of hot PNSs, although it plays a subdominant role for the properties of cold NSs (Schneider et al., 2019b; Yasin et al., 2020). Bigger values of the effective nucleon mass lead to reduced thermal pressure and thus more compact outer layers of the PNSs, smaller neutrinosphere and PNS radii, and therefore higher neutrinospheric temperatures. Correspondingly and consistently with the 3D models of Figure 11 as well as the works mentioned in the previous paragraph, Schneider et al. (2019b), Yasin et al. (2020), and Eggenberger Andersen et al. (2021) therefore also obtained easier and earlier explosions when the PNS contracts faster for greater values of the effective nucleon mass. Again, this is in conflict with the findings by Boccioli et al. (2022), who, applying their 1D treatment of turbulence, did not obtain any clear correlation between PNS (and neutrinosphere) radius, effective mass of nucleons, and explosion behavior, but instead reported a better correlation between the viability of the explosion and the value of the central entropy per nucleon 5 ms after core bounce. Once more we warn the reader that approximate descriptions of turbulent effects in spherically symmetric CCSN models may cause artifacts in disagreement with direct 3D simulations.

Summarizing the situation one can say that CCSN models with different input physics —except those of Boccioli et al. (2022)— agree in their result that a faster PNS contraction tightly correlates with a greater likelihood of explosion by the neutrino-driven mechanism. This outcome was obtained in a similar manner for a variety of physical effects that can trigger the accelerated shrinking of the PNS. In the specific case of varied effective nucleon masses in the super-nuclear EoS, it was also found that larger effective masses of the nucleons do not only lead to higher luminosities and mean energies of the radiated neutrinos (Schneider et al., 2019b) but also to bigger amplitudes and frequencies of the GW emission (Eggenberger Andersen et al., 2021) and to an earlier collapse of the hot PNS to a BH at a lower maximum mass, if the SN explosion fails (da Silva Schneider et al., 2020).

2.3.3 Relevance of the symmetry energy

The nuclear symmetry energy is another important parameter that determines the properties of the high-density EoS and that has a bearing on the evolution of PNSs in CCSNe (the impact of the symmetry energy during the post-merger phase of

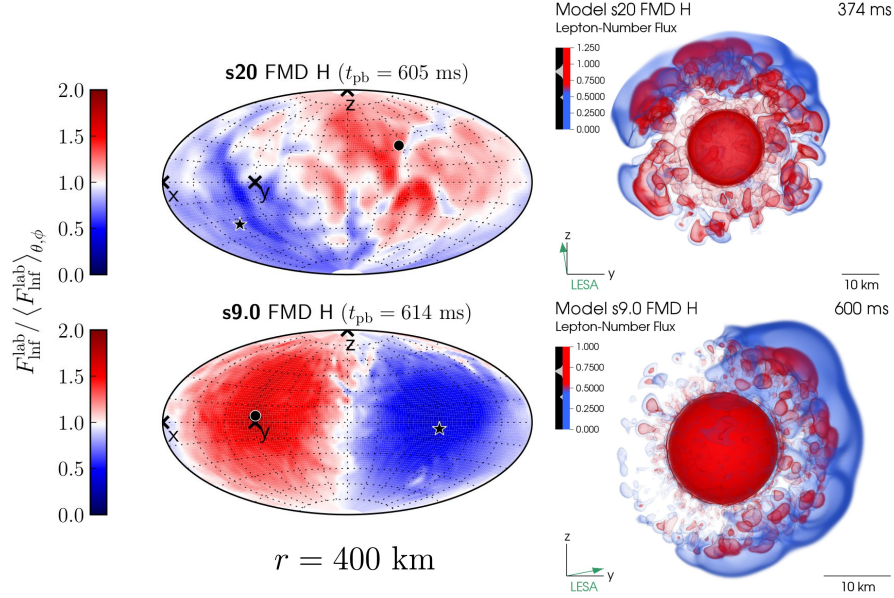


Fig. 12 Dipolar lepton-number emission asymmetry (LESA) of the neutrino lepton-number flux (electron neutrinos minus antineutrinos) in 3D CCSN simulations of $20 M_{\odot}$ (*top*) and $9.0 M_{\odot}$ (*bottom*) progenitors. The Aitoff projections on the *left* visualize the flux density in the lab frame normalized by the angular average at a radius of 400 km and about 0.6 s after core bounce with the bullets indicating the direction of the LESA dipole moments and the stars the opposite directions. The volume renderings on the *right* show the electron lepton-number flux density in the lab frame normalized by $10^{43} \text{ cm}^{-2} \text{ s}^{-1}$ in the interior of the PNS at the times labelled in the plots. The LESA dipole direction is indicated by the green arrow in the tripod in the lower left corner of each panel. The bubble-like structures are connected to PNS convection in a layer of roughly 10 km width and display a clear hemispheric asymmetry with stronger convection on the side of the LESA dipole direction (Figure from Glas et al. 2019; ©American Astronomical Society. Reproduced with permission)

coalescing binary NSs has recently been investigated, too, by Most & Raitel, 2021). It occurs in an expansion of the energy per nucleon of uniform matter composed of neutrons and protons at zero-temperature in terms of the isospin asymmetry $\delta = (n_n - n_p)/n_B = 1 - 2Y_q$ (e.g., Oertel et al., 2017):

$$E(n_B, \delta) = E_0(n_B) + E_{\text{sym}}(n_B) \delta^2 + \mathcal{O}(\delta^4), \quad (13)$$

where n_n, n_p, n_B, Y_q are the neutron number density, proton number density, baryon number density $n_B = n_n + n_p$, and hadronic charge fraction (or proton fraction) $Y_q = Y_p = n_p/n_B$ (which is equal to $Y_e = Y_{e^-} - Y_{e^+}$ for charge-neutral n - p - e matter), respectively. Close to nuclear saturation density n_0 , both the energy per nucleon of symmetric matter (i.e., equal numbers of neutrons and protons), $E_0(n_B)$, and the symmetry energy (i.e., the difference between the energy of symmetric matter and pure neutron matter), $E_{\text{sym}}(n_B)$, can be expanded in the deviation

$x = (n_B - n_0)/(3n_0)$ of the baryon density from n_0 :

$$E_0(n_B) = m_B c^2 - B_0 + \frac{1}{2} K x^2 + \frac{1}{6} Q x^3 + \dots, \quad (14)$$

$$E_{\text{sym}}(n_B) = J + Lx + \frac{1}{2} K_{\text{sym}} x^2 + \dots \quad (15)$$

Here, B_0 is the binding energy of symmetric matter at saturation, K the incompressibility, Q the skewness, J the symmetry energy at saturation, L the slope parameter of the symmetry energy, and K_{sym} the incompressibility of the symmetry energy at saturation density. At nuclear saturation density and for symmetric matter one has $\partial E / \partial n_B(n_B = n_0, \delta = 0) = 0$ by definition.

The symmetry energy has immediate influence on the structure, thermodynamic state, and composition of NS matter, because the pressure P , temperature T , and chemical potentials μ_i of the particles of species i are thermodynamically given by derivatives of the energy per baryon,

$$P = n_B^2 \left(\frac{\partial E}{\partial n_B} \right)_{s, Y_i}, \quad T = \left(\frac{\partial E}{\partial s} \right)_{n_B, Y_i}, \quad \mu_i = \left(\frac{\partial E}{\partial Y_i} \right)_{n_B, s, Y_{j \neq i}} = \left(\frac{\partial E_i}{\partial Y_i} \right)_{n_B, s_i}, \quad (16)$$

with s being the entropy per baryon and E_i and s_i denoting the energy per baryon and entropy per baryon of species i .

A particularly interesting aspect was first discussed by Roberts et al. (2012b), who investigated the effects of the symmetry energy on PNS convection during the SN explosion and the Kelvin-Helmholtz neutrino cooling phase of the hot compact remnant. The linear growth of Ledoux convection is driven by unstable gradients of composition (for n - p - e matter including neutrinos expressed in terms of the net electron-type lepton fraction $Y_l = Y_e + Y_{\nu_e} - Y_{\bar{\nu}_e}$) and entropy. It is governed by the Ledoux criterion:

$$C_L = - \left(\frac{\partial P}{\partial n_B} \right)_{s, Y_l}^{-1} \cdot \left[\left(\frac{\partial P}{\partial s} \right)_{n_B, Y_l} \frac{ds}{dr} + \left(\frac{\partial P}{\partial Y_l} \right)_{n_B, s} \frac{dY_l}{dr} \right], \quad (17)$$

where positive values of C_L indicate conditions that are unstable against Ledoux convection. PNS convection takes place in the optically thick regime for neutrinos, where neutrinos propagate via diffusion and are effectively in thermodynamic equilibrium with the stellar plasma. Therefore they provide a pressure component that contributes to establish pressure equilibrium between rising and sinking buoyant fluid elements and their surroundings, for which reason neutrino effects should be taken into account in the Ledoux criterion.

For $T \approx 0$ and provided neutrino contributions are negligible, i.e., $Y_q = Y_l = Y_e$, one gets

$$\left(\frac{\partial P}{\partial Y_l} \right)_{n_B} \cong \frac{\hbar c}{3} (3\pi^2)^{1/3} n_B^{4/3} Y_e^{1/3} - 4n_B^2 E'_{\text{sym}}(n_B) \delta, \quad (18)$$

where the first term on the rhs corresponds to the contribution by ultra-relativistic, extremely degenerate electrons. The second term is derived from Eq. (13), using the first relation in Eq. (16) for the pressure, and is the contribution from the nuclear medium with $E'_{\text{sym}}(n_B) = \partial E_{\text{sym}}/\partial n_B = (\partial E_{\text{sym}}/\partial x)(dx/dn_B) = (L + K_{\text{sym}}x)/(3n_0)$.

The partial derivatives of the pressure with respect to density and entropy in Equation (17) are always positive, which means that negative entropy gradients always tend to destabilize against convection. In contrast, Equation (18) implies that $(\partial P/\partial Y_l)_{n_B,s}$ can change its sign. It is positive for matter close to isospin symmetry (i.e., $\delta \sim 0$) and thus high Y_e , whereas for more neutron-rich conditions, i.e., small Y_e , it may become negative at high densities, depending on the slope of the nuclear symmetry energy $E_{\text{sym}}(n_B)$ around and above nuclear saturation density. Thus the symmetry energy can have a direct influence on the strength and duration of PNS convection. Roberts et al. (2012b) showed that for EoSs with a steeper increase of $E_{\text{sym}}(n_B)$ with density, convection in the PNS mantle ceases at an earlier time than in cases where $E'_{\text{sym}}(n_B)$ is smaller, because for steep $E_{\text{sym}}(n_B)$ the second term in Equation (18) becomes increasingly dominant when the PNS mantle contracts and Y_e drops. Eventually the term depending on $(\partial P/\partial Y_l)_{n_B,s}$ is able to stabilize convection. This EoS dependent difference in the convective activity leads to characteristic differences in the temporal decline of the neutrino emission, for example to distinctively different times for the break in the neutrino luminosities that signals the moment when convection ends within the PNS.

The impact of the nuclear symmetry energy on PNS convection has also a bearing on a phenomenon called lepton-emission self-sustained asymmetry (LESA), which was first witnessed in 3D CCSN simulations of the Garching group by Tamborra et al. (2014a) and Tamborra et al. (2014b), and which was later confirmed by other works (Janka et al., 2016; O'Connor & Couch, 2018; Glas et al., 2019; Powell & Müller, 2019; Vartanyan et al., 2019). The LESA phenomenon constitutes a global neutrino-emission asymmetry of the PNS, which manifests itself in a stable, long-lasting anisotropy of the electron lepton-number (electron neutrino minus electron antineutrino) emission, for which the dipole term can become the dominant multipole and even larger than the monopole component (Figure 12, left panels). This implies that the individual ν_e and $\bar{\nu}_e$ number fluxes exhibit hemispheric asymmetries on the level of some 10% such that in one hemisphere the emission of ν_e strongly dominates the $\bar{\nu}_e$ emission, whereas their relative magnitudes are much more similar (or even reversed) in the opposite hemisphere. Also the energy luminosities of the individual neutrino species and their summed luminosity show hemispheric differences on the level of several percent.

These emission asymmetries can be traced back to PNS convection that is stronger in the hemisphere of the LESA dipole direction than on the opposite side (Figure 12, right panels). The globally asymmetric convection builds up a hemispheric asymmetry of the Y_e distribution within the PNS with higher Y_e values in the convective layer and the surrounding neutrinospheric region on the side of the LESA dipole maximum. This hemispheric difference can be understood by the fact that strong convection replenishes the leptons lost through neutrino emission by convective transport of electrons out of the huge reservoir of the PNS core, whereas

in the hemisphere with weaker convection this supply with fresh electron lepton number is far less efficient.

The large-amplitude, large-scale directional variations of the neutrino emission associated with the LESA phenomenon have consequences for the detection of CCSN neutrinos (Tamborra et al., 2014b), for neutrino flavor oscillations (Glas et al., 2020; Abbar et al., 2021), and for neutrino-induced PNS kicks (Stockinger et al., 2020). Moreover, the different magnitudes of the electron neutrino flux relative to the electron antineutrino flux also lead to a contrast in the neutron-to-proton ratio (and thus Y_e) of the innermost, neutrino-heated SN ejecta on opposite sides of the PNS, because different amounts of ν_e and $\bar{\nu}_e$ are absorbed according to the reactions of Equations (1) and (2) (see Figure 7 and Stockinger et al., 2020).

It might be surmised that the nuclear symmetry energy through its impact on PNS convection could also have an influence on the LESA. If Y_e decreases faster in the hemisphere opposite to the LESA dipole direction, a steeper slope of $E_{\text{sym}}(n_B)$ will tend to stabilize convection in this hemisphere through a change in the sign of the pressure derivative in Equation (18), whereas Ledoux convection on the other side of the PNS, where Y_e is still higher, can continue without such a damping effect. This contrast in the Ledoux conditions in both hemispheres can therefore sustain the LESA dipole asymmetry. Such a possibility was already pointed out by Janka et al. (2016), and indeed 3D CCSN simulations with different nuclear EoSs (those of Figure 11) reveal that high LESA dipole amplitudes exist for longer post-bounce evolution periods if the symmetry energy of the EoS increases more steeply with density.

The fingerprints of LESA neutrino-emission asymmetries on the innermost ejecta must also be expected to have implications for CCSN nucleosynthesis. A detailed investigation of this possibility, based on 3D explosion models, has still to be performed; for preliminary results making use of 2D SN simulations, see Wanajo et al. (2018).

2.3.4 Relevance of the nucleon mean field potentials

The nuclear symmetry energy also plays a role for the charged-current reactions of neutrinos with unbound nucleons, because these processes are modified by the mean field potentials that describe the interactions of nucleons in dense media (for comprehensive discussions, see, e.g., Fischer et al., 2014; Hempel, 2015; Oertel et al., 2017). Within mean-field models the single-particle energies of nucleons are written as the sum of a kinetic part that depends on the effective nucleon mass m_i^* ($i = n, p$) and a mean-field interaction potential. In the nonrelativistic limit they are approximated by

$$E_i \cong m_i c^2 + \frac{p_i^2}{2m_i^*} + U_i, \quad (19)$$

and the nonrelativistic potential difference ΔU between neutrons and protons is given by the interaction part of the symmetry energy, $E_{\text{sym}}^{\text{int}}$, and corrections depend-

ing on higher orders in the asymmetry parameter $\delta = 1 - 2Y_p$:

$$\Delta U = U_n - U_p = 4(1 - 2Y_p)E_{\text{sym}}^{\text{int}}(n_B) + \mathcal{O}((\Delta Y_p)^2) \cong 4(1 - 2Y_p)E_{\text{sym}}^{\text{int},0}(n_B), \quad (20)$$

where $\Delta Y_p = Y_p - 0.5$, the quantity $E_{\text{sym}}^{\text{int},0}$ is the interaction part of the symmetry energy at zero temperature, and higher-order terms in Y_p are ignored in the last expression (Hempel, 2015). Similarly, for the chemical potential difference one obtains in the same approximation (Hempel, 2015; Most & Raithel, 2021)

$$\hat{\mu} = \mu_n - \mu_p \cong (m_n - m_p)c^2 + 4(1 - 2Y_p)E_{\text{sym}}^{\text{int}}(n_B). \quad (21)$$

Both of the quantities in Equations (20) and (21) enter the calculation of the charged-current reactions of Equations (1)–(4). In this way the nuclear symmetry energy has a direct bearing on the neutrino emission of the PNS and thus, indirectly, on the nucleosynthesis conditions in the CCSN ejecta.

In the neutron-rich conditions of the nascent NS, the mean-field potential difference between neutrons and protons is positive and can reach values up to several 10 MeV. Due to this difference of the neutron and proton energies, the energies of ν_e produced by electron captures are decreased and the energies of $\bar{\nu}_e$ created by positron captures are increased. Moreover, the mean-free-path for ν_e absorption is reduced. Overall, the spectral differences between the electron neutrinos and antineutrinos radiated by the PNS are amplified. Martínez-Pinedo et al. (2012) and Martínez-Pinedo et al. (2014) as well as Roberts et al. (2012a) and Roberts (2012) found that this leads to relatively enhanced absorption of $\bar{\nu}_e$ in the neutrino-driven wind and thus to slightly neutron-rich conditions at least during a transient period of the wind evolution. This effect is, however, reduced or even erased by PNS convection, because the convective flows carry electron lepton number from the non-convective central core of the PNS to the PNS mantle layers and thus enhance the emission of ν_e relative to $\bar{\nu}_e$ (Hüdepohl, 2013; von Groote, 2014; Mirizzi et al., 2016; Pascal et al., 2022). Robust r-process conditions in neutrino-driven winds of newly formed NSs are therefore not facilitated by the mean-field effects in the charged-current weak reactions.

2.3.5 Closing remarks

The EoS of hot PNS matter thus influences CCSN explosions and their ejecta properties in multiple ways, directly by determining the formation of either a NS or a BH, and indirectly by governing the time when the explosion sets in, the contraction of the new-born NS, and the characteristics of the neutrino emission of the compact remnant. In this section we reported on several examples how physical effects connected to the high-temperature nuclear EoS can affect the neutron-to-proton ratio in the innermost, neutrino-heated SN ejecta. But also the explosion energy and large-scale explosion asymmetries (e.g., connected to the LESA phenomenon) may depend on the nuclear EoS.

These questions are barely explored to date, mainly because the self-consistent, ab-initio 3D modelling of stellar collapse and explosion with elaborate neutrino transport methods has only recently become possible and such 3D simulations are still computationally demanding. Also the implications of 3D explosions with detailed neutrino physics for CCSN nucleosynthesis have still to be investigated. It is well possible that characteristic fingerprints in the chemical abundances of special types of SNe could provide clues on the high-temperature EoS in nascent NSs, for example the presence of weak r-process elements in ECSN-like explosions (Section 2.3.1) or the existence of third-peak r-process nuclei in CCSNe triggered by a hadron-quark phase transition (Section 2.1.3). Such special signatures might yield information on the finite-temperature EoS complementary to the messages carried by the GW and neutrino signals that will be measured for a future Galactic stellar collapse event and that will be deduced from the post-merger ring-down GW and kilonova emission of nearby binary NSs.

3 Compact-object mergers

This part of the article addresses the merging of two compact objects and, in particular, covers the mass ejection and nucleosynthesis of these events. The different phases and the general dynamics of a merger are described in Section 3.1. The various mass ejection processes are addressed in Section 3.2. Section 3.3 provides an overview on the rapid neutron-capture process (r-process). Messengers from COM and current observations are discussed in Sections 3.4 and 3.5. The EoS impact on the ejecta and nucleosynthesis is detailed in Section 3.6.

The presentation strives for a pedagogical introduction rather than a detailed review of the latest advances in the field or a description of the historical developments. The references in this handbook article are intentionally limited to a relatively small number to make it easier to navigate through and to present a selection as a start for more detailed reading. The reader is encouraged to follow up and to consult studies which could not fit here especially on more advanced or related topics which could not be addressed. Also, references are avoided for more general descriptions, e.g. in Sections 3.1 and 3.3, where a number of review articles are available. More literature can also be found in these reviews, e.g. Arnould et al. (2007); Sneden et al. (2008); Thielemann et al. (2011); Fernández & Metzger (2016); Baiotti & Rezzolla (2017); Metzger (2019); Horowitz et al. (2019); Siegel (2019); Bauswein & Stergioulas (2019); Shibata & Hotokezaka (2019); Radice et al. (2020); Ciolfi (2020); Nakar (2020); Perego et al. (2020); Cowan et al. (2021); Kyutoku et al. (2021); Rosswog & Korobkin (2022).

3.1 Merger Dynamics and Phases

The merging of two NSs proceeds through different phases and can produce different final objects. Various physical mechanisms govern the evolution in these stages of the merger and shape the observable signals. Figure 13 provides an overview, and Fig. 14 illustrates the evolution by snapshots from hydrodynamical simulations of the early dynamical merger phase.

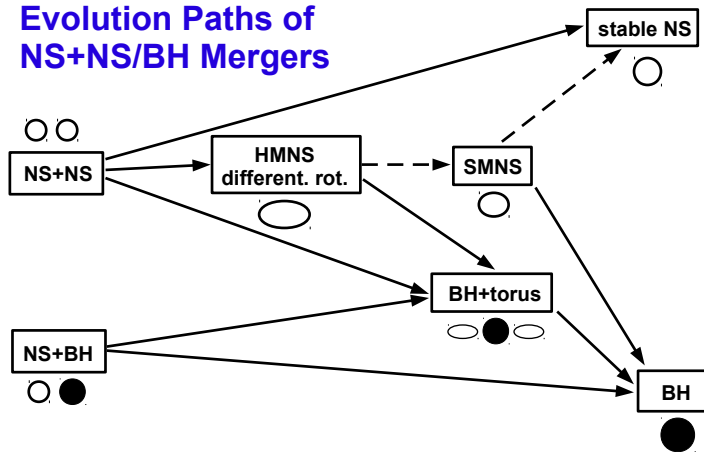


Fig. 13 Evolutionary paths of COMs. The fate of a compact object binary depends predominantly on its mass and the high-density EoS. The evolution involves many different time scales. SMNS refers to supermassive NSs, i.e. objects with a mass that exceeds the maximum mass of non-rotating NSs and which are stabilized against the gravitational collapse by rigid rotation. Differential rotation can provide even more stability, and differentially rotating neutrons stars whose mass exceeds the maximum mass of SMNSs are called hypermassive (HMNS). See main text for explanations. Figure from Just et al. (2015); ©Oxford University Press on behalf of the Royal Astronomical Society (RAS). Reproduced with permission

Binary evolution: The merger of NSs in a binary system is the result of continuous GW emission, reducing the angular momentum and energy of the system and leading to an “inspiral” of the binary components, i.e. a continuous and accelerated decline of the orbital separation. The inspiral is driven by point-particle dynamics, where post-Newtonian effects and general relativistic effects, respectively, become increasingly important as the binary components come closer and thus speed up. In the final phase of the inspiral, the orbital period decreases to a few milliseconds and the stellar components experience tidal deformations during the last revolutions. In general, the evolution is dominantly determined by the binary masses of the system and to some extent by the spins and the finite size of the stellar components.

Merger dynamics: The stars finally coalesce with a relatively large impact parameter since the system features a significant amount of angular momentum. For typical NS masses of 1.3 to 1.4 M_{\odot} (see e.g. Lattimer, 2012) the total mass of the

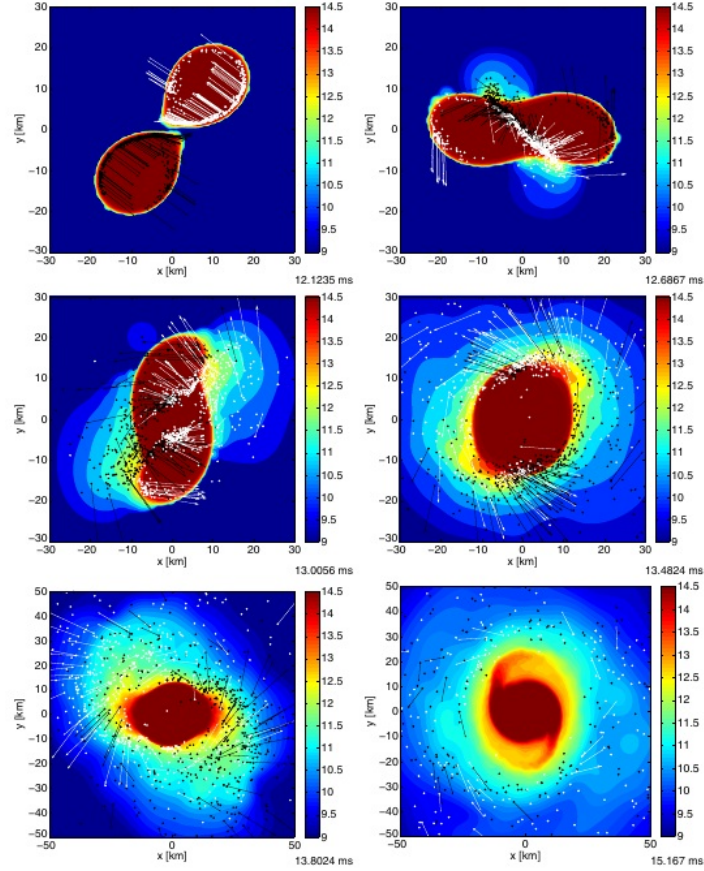


Fig. 14 Rest-mass density evolution (color-coded is the $\log_{10}\rho$ with ρ in g/cm^3) in the equatorial plane of a $1.35\text{-}1.35 M_{\odot}$ NS merger with the DD2 EoS (Hempel & Schaffner-Bielich, 2010; Typel et al., 2010). Dots trace fluid elements which become gravitationally unbound until the end of the simulation. Arrows indicate the current velocity of the fluid elements. Figure from Bauswein et al. (2013); ©American Astronomical Society. Reproduced with permission

system will likely exceed the maximum mass M_{max} of non-rotating NSs. The remnant may however avoid the gravitational collapse because of the rapid rotation. During the coalescence temperatures rise and can reach several 10 MeV providing additional thermal pressure support. Only if the total mass exceeds a threshold binary mass M_{thres} , the merger remnant collapses into a BH within less than a millisecond. In the case of such a “prompt collapse” most of the matter is swallowed by the forming event horizon but material with sufficient angular momentum forms a torus around the central BH. The exact threshold mass depends on the EoS and is not precisely known. It is also influenced by the binary mass ratio and the intrinsic spins of the binary components if sufficiently large. For currently viable EoS mod-

els M_{thres} ranges from about $2.8 M_{\odot}$ to $3.5 M_{\odot}$ (Bauswein et al., 2021). Considering this range the likely outcome of a merger with typical binary masses of $2.7 M_{\odot}$ is the formation of a rotating NS remnant.

Remnant evolution: The merger remnant is initially strongly deformed and oscillating. The cores of the binary components form a rotating double-core structure with a shearing layer in between, which is created during the first contact of the stars (see Fig. 14). In this contact layer the Kelvin-Helmholtz instability develops and highest temperatures are found there. The collision excites significant quasi-radial and quadrupolar oscillations of this remnant structure. During the merging process tidal arms form at the outer edges of the stars. For asymmetric binaries symmetry is broken and one primary tail forms from the tidally elongated lighter companion star, which is wrapped around the more massive component.

The tidal arms settle into a more axisymmetric inflated torus around the central region. The initially very complex velocity field of the double-core structure evolves into an axisymmetric differentially rotating object, while the oscillations are damped on time scales of several 10 milliseconds. After the initial dynamical merger stage a quasi-equilibrium is reached and the remnant enters a phase of secular evolution. Possibly, an $m = 1$ one-armed spiral instability develops, which breaks axisymmetry and which can persist for many dynamical time scales (Paschalidis et al., 2015). Literally, the remnant develops a “bump” which is wobbling around.

The evolution of the system is driven by angular momentum redistribution mostly by magnetic fields (generating turbulent motion) and losses of energy and angular momentum through GWs and neutrinos. These processes will drive the central remnant towards a state of uniform rotation, while centrifugal and thermal support is drained from the inner core. Redistribution and losses of angular momentum and energy destabilize the remnant, which can trigger a delayed gravitational collapse. This delayed BH formation can take place soon after merging, i.e. in the dynamical phase of the remnant evolution, or on longer secular time scales. The life time of the remnant depends sensitively on the total mass, i.e. how close it is to the threshold mass for prompt BH formation. Obviously, the binary mass ratio also affects the life time as it determines the total amount of angular momentum in the remnant and its initial distribution throughout the central object. If a delayed collapse occurs, matter of the outer parts of the remnant with sufficient centrifugal support will form a torus around the central BH.

Torus evolution: As in the case of a prompt collapse, the BH torus system created after a delayed collapse will undergo further evolution. Again, this stage is driven by angular momentum transport by viscous and magnetic effects in combination with neutrino radiation cooling of the torus. (Note that the literature often uses the term disk and torus interchangeable albeit the geometry is closer to an inflated torus rather than a thin disk). As a result of this evolution the largest fraction of the initial torus mass is accreted by the BH. However, as angular momentum is transported outwards and various processes heat the torus, a substantial amount of matter becomes gravitationally unbound (see discussion below). Typical time scales of the secular evolution before or after a delayed collapse can be coarsely estimated

to be of the order of one second (times scale of angular momentum redistribution in the remnant NS, accretion time scale of a viscous torus and the cooling time scale).

Remnant classification: For not too large total binary mass the system may avoid the gravitational collapse until it reaches a phase of uniform rotation. Ultimately, centrifugally supported torus material could partly fall back onto the central NS remnant such that an isolated, uniformly rotating, cold NS is left on longer time scales. The literature has established the term “supermassive” NS (SMNS) for a system with the mass exceeding M_{\max} but stabilized by *uniform* rotation (see Paschalidis & Stergioulas (2017) for a review on rotating NSs). Uniform rotation can stabilize stars up to roughly $1.2 M_{\max}$, where fast rotation (and thus more stabilization) is limited by mass shedding from the surface. Differential rotation allows for faster rotation in the center and can thus support more mass. Stars with a mass beyond the threshold of uniformly rotating NSs of about $1.2 M_{\max}$ are referred to as “hypermassive” (Baumgarte et al., 2000). The terms “supermassive” and “hypermassive” are often used in the context of merger remnants with hypermassive remnants being systems which cannot be stabilized by uniform rotation and which thus undergo a delayed collapse in contrast to supermassive remnants where uniform rotation is sufficient to prevent BH formation.

However, it is conceivable that a supermassive remnant, i.e. a uniformly rotating NS, will be magnetized, leading to magnetic dipole emission, and thus its rotation slows down (similar to the known pulsar spin-down). Hence, if the mass of the object exceeds M_{\max} , it may also collapse into a BH (Fig. 13). Only for very light binary systems the final object may be a stable NS, i.e. if the remnant’s mass after all mass loss episodes during the secular evolution (to be discussed in more detail below) is smaller than the maximum mass of non-rotating NSs. M_{\max} is probably not significantly above $2.0 M_{\odot}$ implying that at most the lightest binaries will result in a stable NS, e.g. (Lattimer, 2012; Oertel et al., 2017; Margalit & Metzger, 2017; Rezzolla et al., 2018; Ruiz et al., 2018; Shibata et al., 2019).

NS-BH mergers: This article focuses on NS mergers, but large parts of the discussion apply to NS-BH mergers as well. For these systems, it is reasonable to expect that the BH will be significantly more massive than the NS, and thus the binary mass ratios will be more extreme as compared to NS mergers. Also, for these systems the spin of the BH can have a significant impact on the dynamics, because it can be larger than that of NSs, which is usually assumed to be small (Tauris et al., 2017).

There can be two fundamentally different outcomes of a NS-BH merger depending on the EoS and the exact binary parameters including the BH spin (e.g. Janka et al., 1999; Janka & Ruffert, 2002; Rosswog, 2005; Shibata & Taniguchi, 2008; Duez et al., 2010; Foucart et al., 2011; Kyutoku et al., 2011; Etienne et al., 2012; Foucart et al., 2013, 2014; Bauswein et al., 2014; Kyutoku et al., 2015, 2021). If the binary mass ratio is not too extreme, the NS is tidally elongated and disrupted. The tidal arm forms a torus around the BH and some matter from the tip of the tidal tail may become gravitationally unbound. For more extreme mass ratios, however, the NS may be swallowed by the BH as a whole and no matter will remain outside the BH.

For a fixed mass ratio, systems with a faster spinning BH lead to more matter outside the BH. Generally, tidal effects are more pronounced in NS-BH mergers as compared to NS mergers because of the more extreme binary mass ratio, which leads to a more pronounced tidal disruption of the NS. For favorable binary parameters (high BH spin, less extreme mass ratio) a significant amount of matter may become gravitationally unbound during the disruption, i.e. on a dynamical time scale. As in the case of NS mergers, a substantial amount of matter may be ejected on secular time scales from the torus.

3.2 Mass ejection

As described above NS mergers can take different evolutionary paths and result in different final objects, depending on the high-density EoS, the total binary mass, the binary mass ratio and the spins. In particular the duration and detailed evolution of the different stages are determined by these dependencies (Fernández & Metzger, 2016; Baiotti & Rezzolla, 2017; Metzger, 2019; Siegel, 2019; Bauswein & Stergioulas, 2019; Radice et al., 2020; Shibata & Hotokezaka, 2019; Bernuzzi, 2020; Nakar, 2020; Perego et al., 2020; Rosswog & Korobkin, 2022). For a significant range of binary masses an initially very dynamical, violent merger evolves towards a more secular phase, which at some point undergoes another dramatic change when the NS remnant collapses to a BH. After most of the remnant has been swallowed by the BH on very short time scales ($< \text{ms}$), the BH torus system again enters a long-term evolution until all mass is either expelled or accreted by the remaining BH. During all these stages matter is ejected from the system, i.e. it becomes gravitationally unbound (Ruffert et al., 1997; Rosswog et al., 1999, 2000; Oechslin et al., 2007; Metzger et al., 2009, 2008; Dessart et al., 2009; Goriely et al., 2011; Korobkin et al., 2012; Fernández & Metzger, 2013; Bauswein et al., 2013; Hotokezaka et al., 2013b; Perego et al., 2014; Siegel et al., 2014; Metzger & Fernández, 2014; Just et al., 2015).

This scenario can serve as a prototype for the discussion of mass ejection bearing in mind that for higher total binary masses the remnant may collapse promptly or on relatively short time scales into a BH. In this case the dynamical and secular mass ejection from the NS remnant is either missing or limited by its life time. In contrast, a mass ejection episode from a BH torus configuration may be absent for very light binaries which avoid the gravitational collapse completely or sufficiently long. These basic considerations already exemplify that the characteristics and relative contributions of the different mass ejection episodes strongly depend on the parameters of the merger like binary masses and EoS, which determine its evolution and outcome.

Also, the mass ejection from NSBH mergers follows qualitatively the aforementioned stages with a strong tidal component producing dynamical ejecta during merging and the formation of a torus from which secular ejecta originate (Janka et al., 1999; Janka & Ruffert, 2002; Rosswog, 2005; Foucart et al., 2013; Bauswein

et al., 2014; Foucart et al., 2014; Kyutoku et al., 2015, 2021). Obviously, a phase of a quasi-stable NS remnant is missing in these systems.

The literature often distinguishes dynamical ejecta and secular, long-term ejecta, i.e. material becoming unbound on longer time scales and at a lower rate. The latter ejecta component is sometimes referred to as postmerger ejecta or disk/torus ejecta if it originates from the torus. The classification of dynamical and secular ejecta is not very strict and mostly refers to the different stages of the merger. In particular, it does not specify a specific ejection mechanism in detail yet. In fact, several mechanisms contribute to unbind matter during the different stages of the merger (Fig. 15).

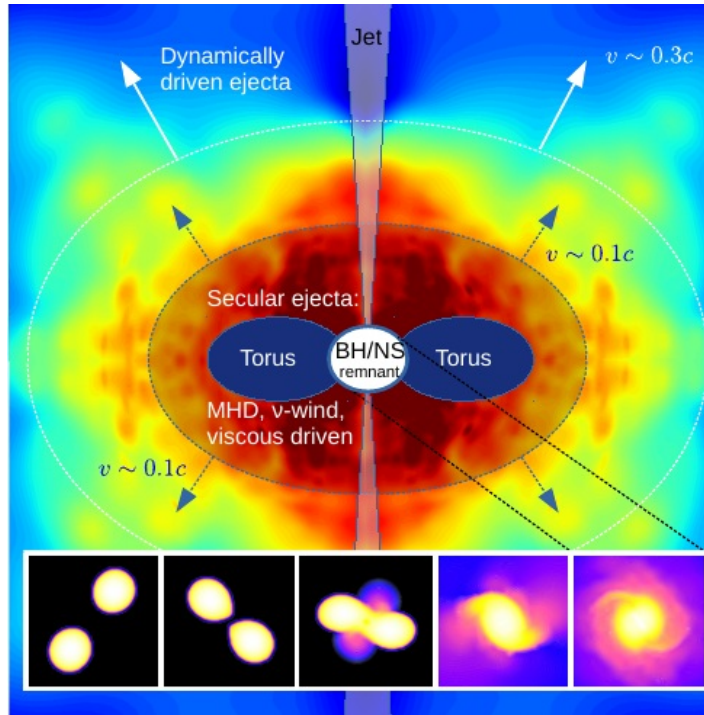


Fig. 15 Overview of different ejecta components and ejection mechanisms. Dynamical ejecta are launched first in a quasi-spherical manner with relatively high velocities of several ten per cent of the speed of light. Hence the dynamical component envelopes the secular ejecta, which typically feature somewhat lower velocities. If a jet emerges from the central object, it drills through the previously ejected material

Dynamical mass ejection: Figure 14 displays the phases of the early merger evolution by snapshots of the density distribution in the equatorial plane from a relativistic hydrodynamical simulation (Bauswein et al., 2013, which includes a description of the basic ejection mechanisms). The calculation follows the evolution

of two stars with a mass of $1.35 M_{\odot}$ and adopts the DD2 EoS (Hempel & Schaffner-Bielich, 2010; Typel et al., 2010). The dots trace fluid elements which eventually become gravitationally unbound during the dynamical evolution of the first 10 ms after merging. A majority of the ejecta originates from the contact interface between the two stars (upper right panel). This matter is shocked in the collisional layer and squeezed out in all directions, slipping over the respective other star (middle left panel). Right after the collision, the NS remnant bounces back and while expanding and rotating strongly, it pushes into the surrounding matter previously squeezed out and thereby, it unbinds a first massive wave of ejecta material (middle right panel). The rotating remnant undergoes several more cycles of contraction and expansion with decreasing amplitude, and thus the ejection of matter continues. Also, spiral arms form at the outer edges of the remnant and run into the surrounding low-density material (lower right panel). For rather asymmetric binary systems a sizable fraction of the ejecta stems from the tip of the massive tidal tail, which developed from the disruption of the lighter companion star.

These mechanisms can unbind several $10^{-3} M_{\odot}$ up to a few $0.01 M_{\odot}$ within only a few milliseconds, hence the term “dynamical” ejecta (e.g. Rosswog et al., 1999; Ruffert & Janka, 2001; Oechslin et al., 2007; Goriely et al., 2011; Korobkin et al., 2012; Hotokezaka et al., 2013b; Bauswein et al., 2013; Palenzuela et al., 2015; Sekiguchi et al., 2015, 2016; Kastaun et al., 2016; Foucart et al., 2016; Lehner et al., 2016; Radice et al., 2016; Ciolfi et al., 2017; Dietrich et al., 2017b,a; Bovard et al., 2017; Radice et al., 2018; Ardevol-Pulpillo et al., 2019; Vincent et al., 2020; Combi & Siegel, 2022). Since the remnant has not yet reached an equilibrium state, it continues to inject energy and angular momentum into its envelope, which can contribute to the mass ejection at a lower rate. For instance, the quadrupolar oscillation of the remnant persists for several 10 milliseconds and possibly a long-lived $m = 1$ deformation develops (Paschalidis et al., 2015). This may increase the ejecta mass by several $10^{-3} M_{\odot}$ on time scales of several 10 milliseconds if the instability and deformation persist sufficiently long and with sufficient strength (Nedora et al., 2019, 2021).

Obviously these mechanisms can only operate as long as the remnant NS does not collapse and they are absent if the merger leads to direct BH formation. If a BH promptly forms, dynamical mass ejection is greatly reduced as the support from the NS remnant is missing (Bauswein et al., 2013; Hotokezaka et al., 2013b; Kiuchi et al., 2019). Only small amounts of ejecta directly emerge from the collision interface. For direct-collapse cases of asymmetric mergers the tidal ejection may lead to unbound matter of several $10^{-3} M_{\odot}$ depending on the binary mass ratio.

The tori forming after a prompt gravitational collapse are less massive in comparison to systems that undergo a delayed collapse (e.g., Hotokezaka et al., 2011; Just et al., 2015; Radice et al., 2018; Kiuchi et al., 2019). Again, unequal-mass mergers lead to more torus material as more material is shed from the tidal arm of the lighter companion. Generally, the reduced torus mass in prompt collapse events implies that there is less secular mass ejection from these systems (see discussion below).

Secular ejecta: In systems that avoid the gravitational collapse, additional effects contribute to the unbound mass on longer time scales of hundreds of millisec-

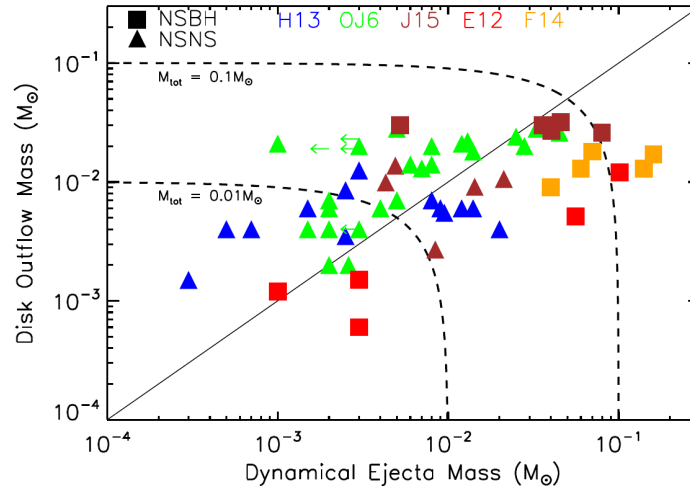


Fig. 16 Compilation of simulation results for the dynamical ejecta and unbound matter from a torus. Figure from Wu et al. (2016); ©Oxford University Press on behalf of the Royal Astronomical Society (RAS). Reproduced with permission

onds to several seconds. The NS remnant featuring temperatures of several 10 MeV emits copious amounts of neutrinos of all flavors with luminosities of the order of 10^{53} erg/sec (Ruffert et al., 1997; Rosswog et al., 1999; Sekiguchi et al., 2011, 2015; Palenzuela et al., 2015). A fraction of these neutrinos is reabsorbed in the outer layers of the remnant depositing sufficient energy to drive a wind (Duncan et al., 1986; Dessart et al., 2009; Perego et al., 2014; Martin et al., 2015; Fujibayashi et al., 2017). This wind ejection will be more pronounced closer to the rotational axis because for geometric reasons the neutrino emission is most intense above and below the oblate-shaped remnant, i.e. towards the polar directions. The neutrino driven ejecta can amount to several $10^{-3} M_{\odot}$ or more (see, e.g., Perego et al., 2014; Fujibayashi et al., 2020b; Nedora et al., 2021) while the exact quantity will strongly depend on the life time of the remnant. This ejecta component is less neutron rich because the rate of electron-neutrino absorptions is close to the rate of electron-antineutrino absorptions, resulting typically in a comparable number of neutrons and protons. It should be emphasized that it is not straightforward to unambiguously identify this ejecta component.

Energy deposition by neutrinos can also play a role in the subsequent BH-torus phase after the gravitational collapse of the remnant (Ruffert & Janka, 1999; Fernández & Metzger, 2013; Just et al., 2015). Naturally, neutrino-driven wind ejecta are significantly more massive during the life time of the NS remnant compared to the BH-torus phase, simply because the NS is much more massive and hotter, and therefore a stronger source of neutrinos than the torus.

Long-term simulations of the magnetized NS remnant indicate the possibility of winds driven by magnetic forces, although various mechanisms are discussed

and details of the ejection depend sensitively on the structure and strength of the magnetic field, which is an active field of research (Siegel et al., 2014; Metzger et al., 2018; Kiuchi et al., 2018; Ciolfi & Kalinani, 2020; Mösta et al., 2020). For instance, in the case that a strong, large-scale helical field develops in the NS remnant, it could drive a polar outflow that can become as massive as $\sim 0.01 M_{\odot}$ (Ciolfi & Kalinani, 2020). Magnetohydrodynamic simulations suggest that the role of magnetic fields in driving outflows depends to some extent on the geometry and strength of the initial magnetic fields carried by the merging NSs, which is not exactly known and may even vary in different binary systems.

At any rate magnetic fields are important because they govern the secular evolution of the torus before and after BH formation (e.g. Siegel & Metzger, 2018; Christie et al., 2019; Fernández et al., 2019; Miller et al., 2019; Murguía-Berthier et al., 2021; Hayashi et al., 2022; Fahlman & Fernández, 2022; Just et al., 2022a). A major source of ejecta stems from the torus either around the central NS or the BH if the former collapsed (e.g. Surman et al., 2008; Metzger et al., 2009; Lee et al., 2009; Fernández & Metzger, 2013; Perego et al., 2014; Metzger & Fernández, 2014; Just et al., 2015). Since matter in the torus is in nearly Keplerian motion and magnetized, the flow is expected to be unstable to the so-called magneto-rotational instability (MRI) (Balbus & Hawley, 1998). The MRI instigates turbulent matter motion, which drives angular momentum transport and generates heat through dissipation of kinetic into thermal energy (e.g. Siegel & Metzger, 2018; Fernández et al., 2019; Just et al., 2022a; Hayashi et al., 2022). Additionally, the recombination of nucleons into helium and heavier nuclei releases energy, which heats the material (Lee et al., 2005; Metzger et al., 2009).

These effects will unbind a significant fraction of the torus of about 10 to 40 per cent over the life time of the torus of seconds. Considering a typical torus mass of $0.1 M_{\odot}$ (e.g. Ruffert & Janka, 1999; Oechslin & Janka, 2006; Shibata & Taniguchi, 2006; Hotokezaka et al., 2013b), the torus or disk ejecta can be massive and in fact dominate other mass ejection channels. Figure 16 compiles data for the torus ejecta and the dynamical ejecta from different simulations providing an overview of typical numbers (Wu et al., 2016).

Since MRI-induced turbulence behaves like a viscosity when averaged over turbulent fluctuation length scales, the ejecta driven by this “turbulent viscosity” are often called viscously driven ejecta. The approximate similarity between a laminar and an MRI-turbulent flow is the reason why in practice many studies adopt the method of viscous hydrodynamics instead of a more complex magnetohydrodynamic description to model accretion disks in numerical simulations (e.g. Fernández & Metzger, 2013; Just et al., 2015; Fujibayashi et al., 2020a). The literature has established different terms referring to this type of mass ejection, and uses synonymously disk ejecta, torus ejecta, viscous ejecta, torus wind or more generally just post-merger ejecta, long-term ejecta, or secular ejecta. As indicated previously, hot accretion tori can also launch neutrino-driven winds, though with significant masses only for very massive tori with $M \gtrsim 0.1 M_{\odot}$. It should also be mentioned that viscous hydrodynamics are employed to study the evolution of massive NS remnants and their ejecta (e.g. Radice et al., 2018; Fujibayashi et al., 2018).

It is needless to say that the properties of the torus ejecta such as their mass do not only depend on the secular evolution of the torus but on the dynamical formation of the torus in the first place setting its initial conditions. This implies that the dynamical merger phase and the secular mass ejection processes are tightly interconnected and are not independent from each other, albeit many studies focus on individual ejecta components because of the tremendous complexity and computational challenge to model the different phases.

A **word of caution** is in order with regard to the ejecta masses and other ejecta or torus properties quoted here and in the literature in general. Most of the understanding of the mass ejection processes of NS mergers and their remnants relies on numerical simulations. These calculations model the relevant physics with different degrees of sophistication and employ different numerical schemes, details of which are beyond the scope of this text (see e.g. Baumgarte & Shapiro, 2010; Rezzolla & Zanotti, 2013; Martí & Müller, 2015; Rosswog, 2015; Shibata, 2015; Duez & Zlochower, 2019). Even by the aid of supercomputers it is challenging to achieve high numerical resolution to resolve for instance the steep density gradients of NSs, turbulent matter motion or the detailed structure and evolution of mass outflows, which typically expand away from the central object, i.e. into regions of coarser numerical resolution. Also, numerical simulations typically follow the evolution of a merger and its remnant only for a finite time, and hence ejecta properties can only be monitored during the simulated time but cannot be followed until the outflow is completely released from the system and reaches its final (so-called homologous) structure. This bears potentially two issues: matter becoming unbound after the end of the simulation is not taken into account and the analysis of ejecta relies on criteria to estimate which fluid elements would in fact become unbound. Typical choices are the assumption of ballistic motion or criteria which consider that internal energy may be converted to kinetic energy during the outflow (Bernoulli criterion) (e.g. Foucart et al., 2021). However, these criteria do not reliably model ejecta physics beyond the simulation time, e.g., the collision of a faster ejecta cloud catching up with slower moving material, or energy injection on longer time scales by nuclear heating or other processes (e.g. Grossman et al., 2014; Rosswog et al., 2014; Metzger et al., 2018; Nativi et al., 2021; Klion et al., 2022; Neuweiler et al., 2022; Haddadi et al., 2022). Unless BH formation is directly simulated, the analysis of torus properties is affected by similar limitations, e.g. different criteria to approximately identify torus material before BH formation actually took place (Oechslin & Janka, 2006; Shibata & Taniguchi, 2006).

In essence, all these considerations indicate that numbers quoted in the literature characterizing ejecta properties should be taken with a grain of salt. Uncertainties of, for instance, ejecta masses may coarsely be estimated to be at least some tens of per cent or possibly even more than a factor 2. This may be inferred by comparing calculations of the same system with different numerical resolutions or the results by different groups using different codes (e.g. Bauswein et al., 2013; Hotokezaka et al., 2013b; Dietrich et al., 2017b; Radice et al., 2018). Similarly, other ejecta properties may be affected by significant uncertainties including velocities, temperatures and the composition. For instance, the distribution of the electron fraction Y_e

as the crucial parameter determining the neutron-richness and thus the details of the r-process (see below), is influenced by the approximate treatment of neutrino radiation, incomplete or approximate sets of weak interaction rates, and the not fully reliable determination of the fluid temperature evolution, since weak reaction rates typically scale with high powers of the temperature (e.g. Foucart et al., 2018; Just et al., 2022a).

Further ejecta properties: It is common to all ejecta components that the matter expands very rapidly with up to several ten per cent of the speed of light (e.g. Hotokezaka et al., 2013b; Bauswein et al., 2013; Fernández & Metzger, 2013; Perego et al., 2014; Siegel et al., 2014; Metzger & Fernández, 2014; Just et al., 2015; Fujibayashi et al., 2017; Radice et al., 2018). This scale may not be surprising considering that the material needs to overcome the enormous gravitational attraction of the compact central object (the escape velocity from an isolated NS is several ten per cent of the speed of light). The different ejecta components usually feature a broad velocity distribution with dynamical ejecta typically being the fastest component. Being ejected first and quasi-spherically, i.e. in all directions, the outermost layers of the outflow are likely to be comprised of dynamical ejecta.

The majority of ejecta originates from deeper crust layers of the NSs, which are very neutron rich. Note that the less neutron-rich outer crust of a NS is not very massive ($< 10^{-4} M_{\odot}$) and can thus not contribute significantly to the unbound matter. The dynamical ejecta for instance mostly stem from the inner crust of the NSs with densities of about 10^{14} g/cm³, which has a proton fraction of less than five per cent, i.e. an electron fraction of $Y_e < 0.05$ adopting charge neutrality. The initial electron fraction is set by the condition of neutrino-less beta-equilibrium in the progenitor stars, i.e. by the balance of weak interactions. The initial composition, however, can change significantly by weak interactions. Even if matter expands fast like the dynamical ejecta, weak reactions can be sufficiently fast to significantly alter the initial electron fraction (e.g. Fernández & Metzger, 2013; Perego et al., 2014; Metzger & Fernández, 2014; Wanajo et al., 2014; Sekiguchi et al., 2015; Just et al., 2015; Goriely et al., 2015; Palenzuela et al., 2015; Wu et al., 2016; Foucart et al., 2016; Radice et al., 2016; Bovard et al., 2017; Fujibayashi et al., 2017; Papenfort et al., 2018; Radice et al., 2018; Martin et al., 2018; Ardevol-Pulpillo et al., 2019; Miller et al., 2019; Fujibayashi et al., 2020b,a; Just et al., 2022a; Combi & Siegel, 2022).

The most relevant weak interactions for setting the Y_e in outflows from COMs are given by Eqs. (1) to (4). During the violent collision in a NS merger, temperatures reach up to several 10 MeV, i.e. well above the rest mass of electrons and positrons. Under these conditions numerous electron-positron pairs are created, which can be captured by the protons and neutrons. Right after the sudden increase of the temperatures when both NSs coalesce, the newly created positrons are captured by neutrons. As there are more neutrons available, positron captures are favored and the initially low electron fraction increases. In addition, the matter is exposed to intense neutrino radiation. As a consequence, this material reabsorbs a large number of electron neutrinos and electron anti-neutrinos, which typically drives the electron fraction towards high values.

Usually the Y_e of most of the ejecta remains below 0.5 for all ejecta components, while the exact impact of weak interactions obviously depends on the (thermodynamic) history of the ejected fluid elements and thus on the mass ejection channel and its details.

For instance, the electron fraction in the dynamical ejecta shows a broad distribution ranging from about 0.05 to 0.45 (e.g. Wanajo et al., 2014; Sekiguchi et al., 2015; Goriely et al., 2015; Palenzuela et al., 2015; Foucart et al., 2016; Radice et al., 2016; Bovard et al., 2017; Radice et al., 2018; Papenfort et al., 2018; Martin et al., 2018; Ardevol-Pulpillo et al., 2019; Combi & Siegel, 2022). During the dynamical mass ejection material expanding along the poles is exposed to stronger neutrino irradiation as compared to the equatorial outflow (which is shielded by the massive torus). Consequently, polar ejecta are less neutron rich with Y_e being higher by roughly 0.1 compared to the equatorial ejecta. This can have a significant impact on the nucleosynthesis in the outflows.

Predominantly neutrino-driven ejecta along the poles are usually less neutron rich because the reabsorption of neutrinos raises the electron fraction in the wind to values above ~ 0.3 up to even 0.5 (e.g., Perego et al., 2014; Just et al., 2015; Fujibayashi et al., 2017, 2020a).

Weak interactions also play a very important role in hot accretion tori and in particular to regulate the Y_e of the corresponding ejecta (Fernández & Metzger, 2013; Just et al., 2015; Siegel & Metzger, 2018; Miller et al., 2019; Fujibayashi et al., 2020a,b; Murguía-Berthier et al., 2021; Just et al., 2022a). The conditions in a typical accretion torus are such that the electron fraction of the torus matter is roughly determined by a beta-equilibrium of the rates given in Eqs. 1 and 4. Since electrons are mildly degenerate in such a torus, positrons are suppressed, resulting in a beta-equilibrium characterized by moderately neutron rich conditions with $Y_e \sim 0.1 - 0.3$. Hot accretion tori emit numerous neutrinos, which is essential in reprocessing the outflowing material and setting its composition. During the expansion from the torus, material is subject to neutrino emission and absorption reactions, which both tend to increase Y_e . As a result, the values of Y_e in the ejecta are higher than in the torus, and typically distributed within $0.25 \lesssim Y_e \lesssim 0.5$. See Just et al. (2022a) for a detailed discussion of the evolution of accretion tori and the conditions in their secular ejecta.

In Metzger (2019); Nakar (2020) tables can be found which summarize various properties of the different ejecta components and provide an overview.

3.3 Nucleosynthesis

All ejecta components provide favorable conditions for the r-process creating heavy elements through successive captures of neutrons onto seed nuclei (Burbidge et al., 1957; Cameron, 1959). See Lattimer & Schramm (1976, 1974); Symbalisty & Schramm (1982); Eichler et al. (1989) for the first suggestions of the r-process taking place in the ejecta of COMs, and Freiburghaus et al. (1999); Metzger et al.

(2010); Roberts et al. (2011); Goriely et al. (2011); Korobkin et al. (2012); Bauswein et al. (2013); Perego et al. (2014); Just et al. (2015); Wu et al. (2016) for some first r-process calculations based on simulation data. During the outflow basically the entire ejecta are converted to heavy nuclei of different nuclear mass numbers between $A = 60$ and $A = 240$ including elements like silver, gold, platinum and uranium. See, e.g., Arnould et al. (2007); Thielemann et al. (2011); Horowitz et al. (2019); Arnould & Goriely (2020); Cowan et al. (2021); Siegel (2022) for reviews on the r-process. The r-process is responsible for the formation of about half of all heavy elements beyond the iron group. This explains the significant scientific efforts in understanding this nucleosynthesis process and especially in elucidating the astrophysical production sites, which has been a major puzzle for decades with CCSNe being the most popular candidate for many years but less favored in the last decade (see Section 2).

Ejecta outflows from mergers expand very rapidly with up to a few ten per cent of the speed of light resulting in a rapid drop of the density by several orders of magnitude in the first few milliseconds, which is accompanied by a decrease of the temperature. Once the temperature falls below ~ 1 MeV (10 Giga-Kelvin), protons recombine with some of the neutrons to form seed nuclei. Because of the neutron-rich conditions there are hundred or more neutrons per seed left. The neutron density is so high that neutron captures are the dominant reaction, i.e., they are faster than β -decays and any seed nucleus becomes heavier and increasingly neutron-rich. The crucial role of this reaction explains the term *rapid* neutron-capture process. Notably, neutron captures are critical to form heavy nuclei because they do not experience the strong Coulomb repulsion of heavy nuclei, which prevents positively charged particles to be captured.

Nuclei cannot become arbitrarily neutron-rich because for too large neutron excess it is energetically unfavorable to bind additional neutrons. In the chart of the nuclei (see Fig. 17), seed nuclei “move” by successive neutron captures far away from the valley of stability to the very right, i.e. close to the so-called neutron drip line, beyond which no nuclei exist and no additional neutron captures can take place. Nuclei in the vicinity of the neutron drip line are highly unstable and quickly undergo a β^- -decay, i.e. a neutron inside a nucleus is converted to a proton. In the chart of the nuclei, a β^- -decay moves the nucleus one step diagonally to the upper left, i.e. a little away from the neutron drip line. Being away from the neutron drip line, neutron captures become possible again and will immediately take place as neutron captures are the dominant reaction in the neutron-rich environment of NS merger ejecta. By a sequence of these two consecutive reactions, i.e. neutron capture and β^- -decay, the seed nuclei will move along the neutron drip line to higher and higher mass number as long as enough neutrons are available for frequent neutron captures.

Once neutrons are exhausted and densities drop, the neutron capture rate decreases. At this point β^- -decays become the dominant reactions. Hence, the ensemble of nuclei that has been built up along the neutron drip line, moves diagonally to the upper left towards the valley of stability. The β^- -decay rates are faster further away from the valley of stability and the “freeze out” slows down as the nuclei ap-

proach the valley of stability. Also other reactions like α -decays may play a role during the freeze out. Neutrons are used up after about a second, which marks the end of the r-process, and nuclei move initially quickly towards the valley of stability. Closer to the valley of stability the nuclear half lives times increase and thus the freeze out takes place on many different time scales to reach the final abundance distribution only as very long-lived nuclei have decayed (up to Gyrs) (see e.g. Mendoza-Temis et al., 2015, for the time evolution of the abundance).

Following the path of the r-process along the neutron drip line, it is evident that the seeds pass nuclei with magic neutron numbers, i.e. closed neutron shells with $N = 50$, $N = 82$ and $N = 126$. For these nuclei being in comparison more stable, reaction rates are slower. Considering the “flow” of the immense number of nuclei moving along the r-process path, the nuclei will move slower through the region with magic neutron numbers. Consequently, during the flow nuclei with closed neutron shells will be in comparison more abundant. These overabundances will be dragged along during the freeze out. Hence, the final abundances will carry an imprint of the closed neutron shells once the freeze out reaches the valley of stability. The r-process path crosses the closed neutron shells close to the neutron drip line, where the magic nuclei have mass numbers A of about 80, 130 and 195, respectively. Beta decays do not change the mass number but convert roughly 15 to 25 protons to neutrons during the freeze out. Hence, the overabundances occur approximately at $A = 80$, $A = 130$ and $A = 195$ in the valley of stability with corresponding atomic numbers of $Z \approx 35$, $Z \approx 55$ and $Z \approx 80$. The respective peaks in the abundance distribution are referred to as the first, second and third r-process peak (see Fig. 18).

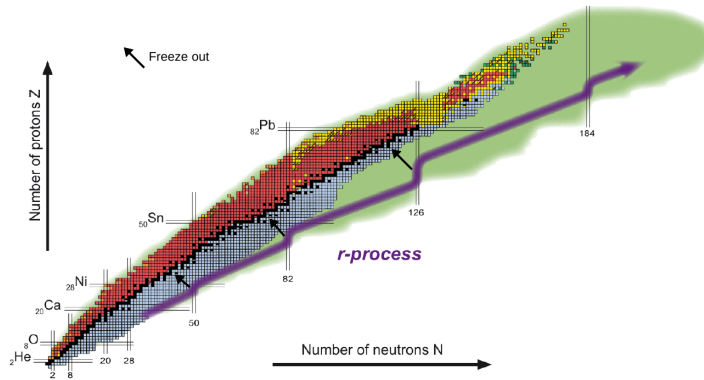


Fig. 17 Chart of the nuclei with the blue arrow indicating the path of the r-process crossing closed neutron shells at $N = 50$, $N = 82$ and $N = 126$. The black arrows visualize the nuclear flow during the “freeze out” towards the valley of stability by β^- decays. Colors of individual nuclei display dominant decay channels: blue β^- decay, red β^+ decay, yellow α decay, black stable nuclei. The green area roughly indicates unstable nuclei which have not yet been measured. In the vicinity of the path of the r-process these nuclei decay predominantly by β^- decays or fission for high mass numbers $A = N + Z$. Figure adapted from EMMI, GSI / Different Arts

Observed abundance pattern: This characteristic abundance pattern is universally found in nature and was for a long time in fact the most convincing argument for the r-process to take place although the astrophysical production site was not identified yet; see e.g. the reviews by Arnould et al. (2007); Sneden et al. (2008); Thielemann et al. (2011); Horowitz et al. (2019); Arnould & Goriely (2020); Cowan et al. (2021); Siegel (2022) for a more exhaustive discussion of the historical developments and the observations. The elemental distribution with distinct r-process peaks is for instance observed in the solar system (see Fig. 18) but also in so-called metal-poor stars, i.e. old stars that formed earlier in the Galactic evolution and were enriched by only a few or possibly a single nucleosynthesis event. The fact that the relative abundance distribution is so similar in these different observations (although with respectively very different absolute abundances) points to a certain robustness and universality of the r-process. It should be mentioned that the interpretation of abundance measurements often relies on subtracting the contributions by other nucleosynthesis processes such as, for instance, the slow neutron-capture process, which takes place in other sites, and is assumed to be sufficiently well known (Fig. 17).

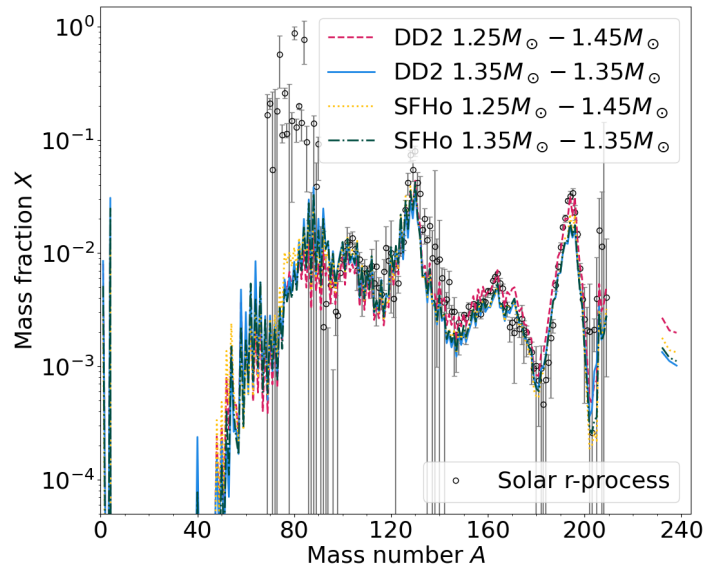


Fig. 18 Abundance distributions of the dynamical ejecta as functions of mass number A for simulations with different binary masses and varied EoS. The black dots display the observed solar r-process abundance pattern. Figure from Kullmann et al. (2022a); ©Oxford University Press on behalf of the Royal Astronomical Society (RAS). Reproduced with permission

R-process in mergers: The basic description of the r-process above illustrates why it is so important to reliably determine the ejecta composition in terms of Y_e . It

is the crucial parameter to set the initial neutron-to-seed ratio and thus the evolution of the r-process as it dictates the number of available neutrons to be captured. For smaller Y_e nuclei with larger mass numbers are reached by the nuclear flow through the chart of the nuclei. In order to create third-peak elements, the electron fraction should not exceed ≈ 0.25 (see e.g. Lippuner & Roberts, 2015, for a comprehensive parameter study). This is considered to be an important threshold because it similarly determines whether significant amounts of lanthanides are produced. Because of their atomic structure these elements feature a particularly high opacity, which strongly effects the electromagnetic emission of the ejecta (Barnes & Kasen, 2013; Kasen et al., 2013; Tanaka & Hotokezaka, 2013).

The ejecta produce electromagnetic emission in the optical, infrared and ultraviolet (Li & Paczyński (1998); Kulkarni (2005); Metzger et al. (2010), see Section 3.4). This astronomical transient is called kilonova referring to its luminosity being roughly thousand times higher than that of novae. The term “kilonova” was proposed in Metzger et al. (2010). Sometimes also “macronova” is used (Kulkarni, 2005). Generally, the kilonova will be redder and dimmer if lanthanides are present, while bluish emission components would require the absence of these elements (Barnes & Kasen, 2013; Kasen et al., 2013; Tanaka & Hotokezaka, 2013; Metzger & Fernández, 2014).

For the production of low-mass number elements, e.g. around the first peak, the electron fraction should not be too low because otherwise all seed nuclei are driven to higher mass numbers. Apart from Y_e , the r-process path is additionally affected by the entropy and the expansion time scale of the outflow, which influence the neutron-to-seed ratio and the reaction rates. See e.g. Lippuner & Roberts (2015) for a parameter study with analytic trajectories.

In addition to neutron captures and β^- -decays other nuclear reactions may become important under certain conditions. For instance, for high-entropy environments photo-dissociation may play a role and establish an equilibrium between neutron captures and dissociations by energetic photons (dubbed $n\text{-}\gamma$ $\gamma\text{-}n$ equilibrium). In this case the nuclear flow does not reach too close to the neutron drip line but proceeds to higher mass numbers somewhat closer to the valley of stability.

Under very neutron-rich conditions (Y_e below ~ 0.2 or even as low as just a few per cent) the neutron-to-seed ratio will significantly exceed 200, which would be the number of neutrons required to reach beyond the third r-process peak. In such a neutron-rich environment, nuclei will attain even higher mass numbers and enter a region in the chart of the nuclei, where fission processes (neutron-induced fission, spontaneous fission, β -delayed fission, photo-fission) become likely at about $A \sim 250$ (see, e.g., Goriely et al., 2013; Eichler et al., 2015; Mumpower et al., 2018; Vassh et al., 2019; Giuliani et al., 2020; Lemaître et al., 2021, for dedicated studies of fission in the context of merger ejecta). When a nucleus fissions, it splits in two fission fragments with mass number of roughly $A/2$ and a few free neutrons. The fission fragments follow some distribution and do not need to be equally heavy (asymmetric fission). In any case the fragments are located at mass numbers of roughly $A = 120$ and can thus start again capturing neutrons and proceed along the r-process path. Possibly the fragments reach the fission region again and a few

cycles can occur. The process is called fission recycling and yields generally very robust and solar-like r-process abundance patterns above $A \approx 130$.

It is important to emphasize that the nuclear reaction rates determining the r-process are not very well known (Arnould et al., 2007; Horowitz et al., 2019; Arnould & Goriely, 2020; Cowan et al., 2021). The r-process involves very neutron-rich, heavy, particularly short-lived nuclei, many of which can currently not be measured by laboratory experiments. Hence, describing reaction rates as necessary input for nuclear network calculations to model the r-process and to calculate the final abundance pattern, largely relies on theoretical models, which extrapolate properties of known nuclei. One of the most important ingredients is the nuclear mass model, which is why mass measurements of very neutron-rich nuclei are highly desirable to benchmark such theoretical calculations. In particular, the construction of the FAIR accelerator facility may allow to measure the properties of nuclei which are currently inaccessible (see, e.g., Cowan et al., 2021). Also, fission rates and the fission fragment distribution exhibit large uncertainties.

All nuclear models reproduce the gross structure of the abundance pattern with distinct peaks. The uncertainties of the abundances of individual elements or nuclei with a given mass number, however, can amount to factors of several for a given set of astrophysical conditions (see, e.g., Goriely et al., 2013; Eichler et al., 2015; Mendoza-Temis et al., 2015; Mumpower et al., 2015, 2016; Martin et al., 2016; Mumpower et al., 2018; Holmbeck et al., 2019; Vassh et al., 2019; Nikas et al., 2020; Giuliani et al., 2020; Lemaître et al., 2021; Barnes et al., 2021; Kullmann et al., 2022b, for sensitivity studies involving different nuclear physics input). The impact of the nuclear reaction models on the final properties of the merger ejecta (abundance pattern and heating rate) is thus sizable. It may therefore not be straightforward to disentangle these nuclear uncertainties from variations in the outflow properties resulting from the EoS or the binary masses. In addition, in theoretical studies the numerical error from the hydrodynamical simulations can be significant and one cannot expect to be able to determine the conditions in the ejecta ab initio for a given EoS and binary masses.

A significant number of studies employs hydrodynamical simulation data of individual or several ejecta components to compute the respective abundances in the outflow by nuclear network calculations (some examples include Freiburghaus et al., 1999; Goriely et al., 2011; Korobkin et al., 2012; Bauswein et al., 2013; Perego et al., 2014; Wanajo et al., 2014; Just et al., 2015; Martin et al., 2015; Wu et al., 2016; Lippuner et al., 2017; Radice et al., 2018; Curtis et al., 2021; Just et al., 2022a; Kullmann et al., 2022a; Perego et al., 2022; Kullmann et al., 2022b; Fujibayashi et al., 2022). In practice, a number of tracers particles in the ejecta monitor the thermodynamical evolution and composition of unbound fluid elements. These trajectories are then post-processed with a nuclear network code. Knowing how much mass a tracer represents one can compute the final elemental distribution by weighting the trajectory accordingly.

Generally, the different types of merger ejecta result in robust abundance patterns that closely follow the solar distribution in some range of mass numbers A . It is, however, also apparent in these calculations that the abundances of individual tra-

jectories extracted from ejecta simulations can in fact show significant differences from a solar-like distribution, and only the appropriate average resembles the solar abundance pattern. This observation cautions that calculations considering individual trajectories or too few tracers may not be representative of a particular astrophysical outflow, which can only be characterized by a distribution of trajectories with different properties (Y_e , entropy and expansion time scale) (e.g. Kullmann et al., 2022b). Note that typical dynamical merger simulations cover only a few 10 milliseconds and usually do not follow the ejecta outflow to very low densities. Hence, for network calculations capturing the r-process on time scales of seconds, trajectories need to be extrapolated which may introduce additional uncertainties. Also, it is important to include the heat generated by the r-process consistently in network calculations, i.e. considering the generation of thermal energy by the decay products, which changes the reaction rates (see e.g. Mendoza-Temis et al., 2015).

Heating: The r-process is not only important for the formation of heavy elements but also because it provides the energy source for electromagnetic emission of the ejecta (Li & Paczyński, 1998; Kulkarni, 2005; Metzger et al., 2010; Roberts et al., 2011; Goriely et al., 2011; Korobkin et al., 2012; Metzger, 2019; Nakar, 2020). As described, the r-process involves sequences of many radioactive decays during the freeze-out process. These decays deposit heat in the ejecta as charged decay products thermalize in the surrounding medium (neutrinos escape unhindered in this stage; gamma rays deposit only a fraction of their energy). The energy release amounts to a few MeV per nucleon, where the major contributions come from beta decays, while alpha decays and fission contribute for very neutron-rich conditions. The decay chains include nuclei with a large spread in their half life times. This implies that the heating occurs on different time scales; and adding up the contributions of many exponential decays of different half life times effectively results in a power law decay of the heating rate. The heating rate, i.e. energy release per time per mass, follows approximately

$$\dot{Q}(t) = 2 \times 10^{10} \text{erg/g/s} \left(\frac{t}{1\text{d}} \right)^{-1.3} \quad (22)$$

(Metzger et al., 2010; Korobkin et al., 2012). This expression should be multiplied by a thermalization efficiency (see, e.g., Metzger et al., 2010; Barnes et al., 2016; Waxman et al., 2018; Hotokezaka & Nakar, 2020), which is of the order of about 0.5, to determine the actual energy deposition in the ejecta and account for the fact that not all energy is actually deposited in the ejecta. Because of the $t^{-1.3}$ behavior, the energy deposition drops by several orders of magnitude from minutes to weeks after merger. The composition of the ejecta as well as the nuclear model of the r-process have some moderate influence on the heating rate (e.g. Hotokezaka & Nakar, 2020). Network calculations show that the universal behavior is a result of an ensemble of trajectories, while the heating rate of individual fluid element histories can deviate significantly. This may suggest that the local energy deposition in a certain region of the ejecta may not necessarily follow a universal behavior but rather a local heating rate, see, e.g., Just et al. (2022b).

It has been pointed out that already a minor fraction of free neutrons that are not captured during the r-process may provide an early intense source of heating (Metzger et al., 2015). As little as $10^{-5} M_{\odot}$ of neutrons could significantly alter the electromagnetic emission during the first hours after merging (recall the half life of free neutrons of about 10 mins). Considering the challenges to resolve ejecta properties in simulations, it is not yet fully settled whether or not a part of the dynamical ejecta can have conditions such that neutrons are left after the r-process. See, e.g., Dean et al. (2021) and references therein.

At later times of weeks after the merger, the heating can be dominated by individual nuclei with half lives of this order, which leads to bumps in the heating rate and thus the bolometric light curve that are potentially observable with the James Webb Space Telescope, a space-borne infrared telescope (Zhu et al., 2018; Wu et al., 2019).

3.4 Messengers

One of the most fascinating aspects of NS mergers is the fact that they can be observed through very different messengers, which carry complementary information about the physical system and in particular about the EoS. Combining several messengers is thus especially informative.

Gravitational waves: The current network of ground-based GW detectors is sensitive to GWs with a frequency between a few 10 Hz and a few kHz (Aso et al., 2013; Acernese et al., 2015; Collaboration et al., 2015). During the inspiral the GW signal of a binary is largely dominated by the (point-particle) orbital motion, and the GW frequency equals twice the orbital frequency. This means that although the binary evolution is driven by GW emission over millions of years, only during the last minute before merging a binary will actually be detectable by a GW instrument. Only in this last phase the system reaches frequencies in the range that is accessible by ground-based instruments. Note that the projected spaceborne LISA GW detector is sensitive to lower frequencies and can thus detect binaries long before merging (Amaro-Seoane et al., 2022).

The signal of a binary, in particular its frequency evolution, is predominantly governed by a single parameter with the dimension of a mass (see for instance Maggiore, 2008; Sathyaprakash & Schutz, 2009; Creighton & Anderson, 2011; Blanchet, 2014). This chirp mass,

$$\mathcal{M} = \frac{(M_1 M_2)^{3/5}}{(M_1 + M_2)^{1/5}}, \quad (23)$$

is given by the masses of the two binary components, and the term chirp mass refers to the increase of the frequency and amplitude with time. Being the dominating parameter describing the signal, \mathcal{M} is measured with very good precision. For not too large mass asymmetries $M_1 \neq M_2$, the chirp mass mostly scales with the total

mass and is less sensitive to the mass ratio q . Hence, a measurement of \mathcal{M} informs approximately about the total mass of a NS binary.

At higher post-Newtonian order additional parameters like the binary mass ratio, spins, and finite-size effects influence the binary evolution and the GW signal. These effects only appear when the velocity reaches a fraction of the speed of light. Hence, they affect the signal only during the late inspiral, when orbital frequencies and thus velocities increase. In this phase the binary evolves very fast, and detectors are less sensitive in this frequency range, which is why the corresponding parameters are more difficult to measure.

Combining \mathcal{M} and the mass ratio $q = M_1/M_2$ one can compute the individual masses of the binary components and thus the total mass. Obtaining the mass ratio and the total mass is important since both clearly affect the dynamics during and after merging and in particular the mass ejection.

The spins of the NSs enter through an effective spin parameter, which contains the contributions from both NSs. It is generally difficult to measure the effective spin parameter and in particular the individual spins through GWs (Farr et al., 2016). In addition, the effective spin and the mass ratio are degenerate. It is often assumed, based on stellar and binary evolution arguments, that spins of NSs in binary systems are rather small, i.e. compared to the orbital motion (Tauris et al., 2017). In fact, the rotation periods of pulsars in known binary NSs are long compared to the orbital period (the fastest known pulsar in a binary has a spin period of 17 ms Stovall et al., 2018). Also note that tidal locking during the late inspiral phase is estimated not to play a role (Bildsten & Cutler, 1992; Kochanek, 1992; Lai, 1994). If this generally holds true for all binaries, spin effects are less relevant for the dynamics of a NS merger.

EoS constraints from the GW inspiral: Finite-size effects on the GW signal are described by the tidal deformability Λ , which quantifies the quadrupolar deformation of a star by a given tidal field (Flanagan & Hinderer, 2008; Hinderer, 2008; Hinderer et al., 2010; Damour & Nagar, 2010; Damour et al., 2012). In the case of a binary the tidal field is created by the respective companion star. The tidal deformability is defined as property of an isolated static NS and is fully determined by the EoS and mass. For this reason the measurement of the tidal deformability is of immense interest to constrain the high-density EoS. The tidal deformability (also called tidal polarizability) of a NS is given by

$$\Lambda = \frac{2}{3}k_2 \left(\frac{c^2 R}{GM} \right)^5 \quad (24)$$

with the tidal Love number k_2 and the stellar mass M and radius R . The definition of Λ illustrates that tidal effects strongly depend on the mass and the radius or the inverse compactness, respectively. The influence of k_2 is relatively minor, and for a fixed mass the tidal deformability provides a good proxy of the radius. Hence, a measurement of Λ effectively constrains the NS radius.

A larger tidal deformability leads to an accelerated inspiral (see, e.g., Chatziioannou, 2020; Dietrich et al., 2021, for reviews). In a binary system the effect is

described by a mass-weighted linear combination of the tidal deformabilities of the individual binary components. This combined tidal deformability is given by

$$\tilde{\Lambda} = \frac{16}{13} \frac{(M_1 + 12M_2)M_1^4\Lambda_1 + (M_2 + 12M_1)M_2^4\Lambda_2}{(M_1 + M_2)^5} \quad (25)$$

and is the parameter which is actually inferred from a measurement. The binary mass ratio does not affect $\tilde{\Lambda}$ too strongly, in the sense that binaries of the same chirp mass but with different q have very similar $\tilde{\Lambda}$ (e.g. De et al., 2018). Hence, for EoS constraints it is not too essential to measure the mass ratio accurately.

Postmerger GW emission: Gravitational waves are not only emitted during the binary inspiral, but also afterwards if a rapidly rotating NS remnant forms. The violent oscillations of the remnant generate GWs mostly in the range of a few kHz (Xing et al., 1994; Shibata & Taniguchi, 2006; Oechslin & Janka, 2007). If the remnant does not collapse, the signal can persist for several 10 ms over which the oscillations are slowly damped. The dominant oscillation mode of the remnant occurs as a pronounced peak in the GW spectrum and is potentially measurable, although the sensitivity of current detectors declines in this frequency range. Importantly, the frequency f_{peak} of the peak tightly scales with the NS radius and other NS parameters (Bauswein et al., 2012; Bauswein & Janka, 2012; Takami et al., 2015; Bernuzzi et al., 2015; Bauswein & Stergioulas, 2019). Hence, measuring f_{peak} can provide important constraints on the EoS.

The postmerger GW spectrum contains additional subdominant features (e.g. Stergioulas et al., 2011; Bauswein & Stergioulas, 2015; Takami et al., 2015; Bauswein & Stergioulas, 2019). Those can potentially also inform about the EoS although they may be harder to measure. Detecting such features can be rewarding because they may reveal the detailed dynamics of the remnant, which may be important to connect to the dynamical mass ejection. For instance, one of the subdominant peaks emerges from a coupling of the dominant quadrupolar oscillation and the quasi-radial mode (Stergioulas et al., 2011). Hence, this feature can in principle provide information on the radial oscillation of the remnant, which is relevant for the dynamical mass ejection (see above).

Finally, it should be emphasized that the presence or absence of postmerger GW emission informs about the outcome of the merger. Obviously, this is highly relevant for EoS constraints since combined with the mass measurement from the inspiral phase it allows to constrain the threshold binary mass for prompt collapse (Hotokezaka et al., 2011; Bauswein et al., 2013). As described above, the merger outcome is also important for mass ejection and thus the nucleosynthesis and the resulting kilonova signal, which exemplifies the importance to detect postmerger GWs. For a sufficiently loud GW signal it may in principle be possible to measure the life time of the remnant. The ring down of the BH forming during the gravitational collapse of the remnant occurs at several kHz and is thus unlikely to be measured (Shibata & Taniguchi, 2006).

Extrinsic parameters: Detecting GWs is vital in the context of nucleosynthesis because the signal carries important information about additional properties of the

binary which are not intrinsic to the source (Sathyaprakash & Schutz, 2009). The GW amplitude scales with the luminosity distance of the source, which is largely degenerate with the inclination angle of the binary. Obviously both parameters are invaluable to interpret kilonovae and to link the electromagnetic signal to the mass ejection. At typical distances of several 10 Mpc to some 100 Mpc cosmological redshift plays a role (Maggiore, 2008; Sathyaprakash & Schutz, 2009; Creighton & Anderson, 2011). For instance, the chirp mass inferred from the frequency evolution, which is measured by the detector, has to be corrected by adopting a value for the Hubble constant or using, if available, the redshift of the host galaxy (Abbott et al., 2019).

The GW signal also provides a rough localization of the event on the sky (mostly through the different arrival times in the network of detectors), which can be used to trigger and guide electromagnetic follow-up observations to search for the kilonova (Abbott et al., 2020a). More generally, GW detections will yield an estimate of the merger rate in the local universe and the properties of the binary population such as the distribution of masses. The former is obtained by knowing the sensitivity of the GW instruments and thus the volume which is monitored by the detectors, for a given duration of the observing run (Abbott et al., 2017b). These data on the rate and masses of the binaries are essential to quantify the overall production of heavy elements by mergers in the local universe. This may help to assess whether mergers are the dominant contributors of heavy elements or if there are other sites producing significant amounts of r-process elements.

Kilonovae: The most important messenger for accessing the nucleosynthesis of COMs are kilonovae (Li & Paczyński, 1998; Kulkarni, 2005; Metzger et al., 2010; Roberts et al., 2011; Goriely et al., 2011; Metzger, 2019; Nakar, 2020). Based on the properties inferred from simulations one can expect that the majority if not the entire ejecta undergo the r-process. As described above this includes many radioactive decays like beta-decays, gamma-decays, alpha-decays and fission, which deposit heat in the expanding ejecta cloud. This leads to quasi-thermal emission peaking at optical and infrared wavelength. As a result of the many contributions from decays with different half lives, the total heating rate follows roughly a power-law decline and most of the energy is generated in the first seconds.

Very soon after the merger (< 1 second) the ejecta expand homologously, i.e. fluid elements move with a constant velocity except for small changes by working against the gravitational potential and gaining energy through the radioactive decays (Rosswog et al., 2014; Grossman et al., 2014; Kawaguchi et al., 2021; Klion et al., 2022; Neuweiler et al., 2022; Haddadi et al., 2022). Possibly, there could also be additional heating contributions or large scale reconfigurations of the ejecta by energy injection from the remnant (e.g. Metzger et al., 2018; Nativi et al., 2021). Homologous expansion implies that the distribution of mass as function of velocity $m(v)$ remains constant (self-similar), which means that the ejecta have arranged themselves such that faster moving material is ahead of the more slowly expanding shells. A typical distribution $m(v)$ shows the bulk of the ejecta with a velocity of about $0.1 c$ with a steep decline at higher velocities (e.g. Metzger et al., 2015; Radice et al., 2018).

At early times, i.e., in the first hours after the merger, the densities in the ejecta are so high that a major fraction of the expanding outflow is optically thick. Radiation can only escape from the surface layers and most of the radioactive energy is used for expansion work in this phase of the explosion. The photosphere as the area from where photons can stream out, is located in the surface layers, i.e. at very high velocities. As the ejecta expand the density drops and so does the optical depth. Hence, the photosphere moves further inside the ejecta to lower velocities and a larger fraction of the outflow becomes transparent. Here the term “moving inside” does not refer to a radial location in a fixed reference frame but to a frame comoving with the expanding ejecta.

Basic dependencies: A first quantitative assessment is made by comparing the expansion time scale and an estimate of the photon diffusion time (see Arnett, 1980; Metzger et al., 2010; Metzger, 2019). An average radius of the ejecta is given by $R = vt$ with t being the time since merging and with a constant mean velocity v adopting homologous expansion. The mean density of the ejecta is given by $\rho = \frac{3M}{4\pi R^3}$ with M being the mass of the ejecta. Here spherical symmetry is assumed. The photon diffusion time scale can be estimated by $t_{\text{diff}} \sim \frac{R}{c} \tau$ with the optical depth τ . The latter is given by $\tau = \rho \kappa R$ with the opacity κ . The opacity is a material constant and depends on the composition and temperature of the ejecta.

Equating the expansion time scale $t_{\text{ex}} = R/v$ and the diffusion time scale yields $t = \frac{3M\kappa}{4\pi c v}$, which describes the situation when most of the radiation can escape from the outflow. This phase is reached after

$$t_{\text{peak}} = \sqrt{\frac{3}{4\pi c}} \sqrt{M} \sqrt{\kappa} \sqrt{\frac{1}{v}} \quad (26)$$

and determines a time scale for the emission peak of the kilonova as the time when most of the outflow reaches transparency, while the heating continuously declines. For typical values of the ejecta properties this simple estimate yields typical time scales of hours and days for the evolution of the kilonova.

The luminosity at t_{peak} is given by the radioactive heating at that time, i.e., only the contributions from those decay products which efficiently thermalize in the ejecta. Hence, $L_{\text{peak}} \sim M \dot{Q}(t_{\text{peak}})$, recalling that $\dot{Q}(t)$ roughly follows a power law with index -1.3 (with \dot{Q} giving the energy output per time per mass). Inserting t_{peak} yields a typical peak luminosity of 10^{41} to 10^{42} erg/s as order of magnitude estimate.

The temperature of the emission can be obtained from the Stefan-Boltzmann law as

$$T_{\text{peak}} = \left(\frac{L_{\text{peak}}}{4\pi\sigma R^2(t_{\text{peak}})} \right)^{1/4} \quad (27)$$

with the Stefan-Boltzmann constant σ . Hence, the radiation temperature can also be estimated by M , v and κ with typical values of several 1000 K, i.e., an emission peaking in the wavebands between the UV and the infrared. These considerations show that kilonovae are a phenomenon which is accessible by optical telescopes.

These estimates provide the order of magnitude of the kilonova properties. A more refined calculation takes into account the structure of the ejecta, i.e., a distribution $m(v)$. This yields an estimate of

$$t_{\text{peak}} \approx 1.6 \text{d} \left(\frac{M}{10^{-2} M_{\odot}} \right)^{1/2} \left(\frac{v}{0.1c} \right)^{-1/2} \left(\frac{\kappa}{1 \text{ cm}^2/\text{g}} \right)^{1/2} \quad (28)$$

and

$$L_{\text{peak}} \approx 10^{41} \frac{\text{erg}}{\text{s}} \left(\frac{\epsilon_{\text{th}}}{0.5} \right) \left(\frac{M}{10^{-2} M_{\odot}} \right)^{0.35} \left(\frac{v}{0.1c} \right)^{0.65} \left(\frac{\kappa}{1 \text{ cm}^2/\text{g}} \right)^{-0.65} \quad (29)$$

(see (Metzger, 2019)). The luminosity expression contains an additional factor ϵ_{th} accounting for the thermalization efficiency of the radioactive decay products to deposit their energy in the surrounding plasma. Although assumed to be constant here, it in fact follows some time evolution and depends on the exact composition (see Barnes et al., 2016; Hotokezaka & Nakar, 2020).

Overall, these expressions illustrate that the observable kilonova features strongly depend on the properties of the ejecta and r-process. This implies, in turn, that observations of kilonovae can provide information on the ejecta and by this on the EoS, which strongly affects the mass ejection.

The basic dependencies of the above formulae are straightforward to understand. The opacity determines how easily light can escape from the ejecta and thus affects the time the outflow needs to reach transparency. More massive ejecta imply a higher density and thus the emission will peak later since the outflow needs to expand for a longer time to reach a sufficiently low density. Similarly, a higher velocity yields a short peak time scale as the dilution proceeds faster and the ejecta reaches a stage of transparency earlier. Reaching transparency earlier implies a higher luminosity because radioactive heating is stronger at earlier times. Obviously, a more massive ejecta cloud produces a higher luminosity since the total energy output is higher.

Kilonova modeling and opacities: The equations above clearly demonstrate the significant impact of the opacity of the ejecta. It is important to emphasize that the opacity sensitively depends on the composition of the ejecta (Barnes & Kasen, 2013; Kasen et al., 2013; Tanaka & Hotokezaka, 2013). In particular, lanthanides and actinides feature very high opacities, which are two orders of magnitude above typical opacities of iron group elements ($0.1 \text{ cm}^2/\text{g}$). Therefore, the initial electron fraction of the ejecta has a critical influence on the kilonova since it determines the production of lanthanides. For $Y_e < 0.2$ significant amounts of these elements are produced and a typical opacity is of the order of $30 \text{ cm}^2/\text{g}$, whereas for $Y_e > 0.3$ the lanthanide fraction is very small and a typical value of the opacity is about $3 \text{ cm}^2/\text{g}$ (see Tanaka et al., 2020). This exemplifies that kilonova properties in principle provide access to the composition of the ejecta.

Various further refinements and more advanced models exist to predict the bulk properties of kilonovae, which cannot be described in detail here (e.g. Grossman et al., 2014; Villar et al., 2017; Perego et al., 2017; Waxman et al., 2018, 2019; Metzger, 2019; Nakar, 2020; Hotokezaka & Nakar, 2020, and references therein). These

models can for instance include an angle-dependence, a structure of the density and composition in the ejecta, several ejecta components with different velocities and composition (opacity or lanthanide fraction) and a time dependence of the thermalization efficiency. Also, these calculations can predict the time dependence of the light curve or the emission in certain filter bands, i.e. the luminosity in a certain range of wavelength. Such filters are used by telescopes and provide information on the color evolution of an astronomical transient.

The most sophisticated modeling of kilonovae is based on radiative transfer calculations, which follow the propagation of photons through the ejecta cloud partially taking into account detailed atomic interactions (e.g. Kasen et al., 2013; Tanaka & Hotokezaka, 2013; Kasen et al., 2015; Kasen et al., 2017; Tanaka et al., 2018; Wollaeger et al., 2018; Kawaguchi et al., 2018; Bulla, 2019; Watson et al., 2019; Kawaguchi et al., 2021; Domoto et al., 2021; Perego et al., 2022; Just et al., 2022b; Gillanders et al., 2022; Collins et al., 2022; Neuweiler et al., 2022; Vieira et al., 2022). This allows a detailed modeling of the spectra of kilonovae beyond black body emission and provides means to interpret features, which can be connected to specific elements. In a further step the presence or absence of certain elements may be related to details of the mass ejection and the underlying EoS.

In this regard it is important to emphasize that for a large fraction of the heavy r-process elements none or only incomplete atomic data are available. The complexity of the atomic structure of these elements represents a challenge, which is important to be addressed for a full comprehension of the spectral properties of kilonovae and the determination of elemental abundances in the outflow (Kasen et al., 2013; Tanaka & Hotokezaka, 2013; Tanaka et al., 2020; Fontes et al., 2020).

Kilonovae contain a wealth of information about the merger ejecta and thus the underlying physics and especially the EoS, which will be further discussed in Section 3.6. But it should not remain unmentioned that kilonova observations and their interpretation are important in a broader scientific context. The localization of a merger event by GWs is relatively coarse (typically many square degrees), and only by detecting the electromagnetic counterpart the exact position can be determined (Abbott et al., 2017b; Abbott et al., 2020a). This allows to identify the host galaxy and its cosmological redshift. This information can be used to constrain the Hubble constant and to be incorporated in the parameter estimation of the GW signal (Abbott et al., 2017, 2020a). Also, it can be instructive to connect to the properties of the host galaxy and to interpret the spatial offset between merger and host galaxy. These relate to questions of star formation, stellar evolution and binary evolution like the delay time between NS binary formation and merger (Hotokezaka et al., 2018; Tauris et al., 2017; Beniamini & Piran, 2019). The emission of the kilonova features a certain angle dependence, which is why a detailed interpretation can reveal the orientation of the merger, which is, for instance, helpful for GW data analysis. Finally, finding kilonovae in so-called blind surveys, i.e. without GW trigger but by regular wide-field observations, may provide better estimates of the rates of mergers, which is important to address the overall contribution of COM for r-process nucleosynthesis.

Other electromagnetic counterparts: In addition to kilonovae, NS mergers also lead to other phenomena that produce electromagnetic emission, which will be briefly mentioned for completeness (Metzger & Berger, 2012; Nakar, 2020). Driven by magnetic fields and possibly aided by neutrino annihilation, powerful relativistic outflows may be launched from a BH torus system that forms after a NS merger. These outflows are concentrated in a small solid angle around the rotational axis and are referred to as jets. Some models consider jet formation from magnetized NS remnants. In any case, these relativistic jets are launched after mass ejection has started, and thus the jet drills through the ejecta. Farther out internal shocks in the jet produce intense forward-beamed gamma-ray emission, which is observable from cosmological distances (see e.g. Eichler et al., 1989; Nakar, 2007; Berger, 2014; Nakar, 2020). These so-called short GRBs are already observed for decades by gamma-ray satellites. The attribute “short” refers to the length of the gamma-ray emission (below two seconds) and distinguishes the short bursts from the long GRBs, which originate from the collapse of massive stars (see Section 2.1.2).

The relativistic jets run into the interstellar medium and produce the so-called afterglow by synchrotron emission, which is observable from radio to X-rays. Very similar processes are expected to occur when the mildly relativistic ejecta from a merger interact with the interstellar medium resulting in radio remnants, which evolve on time scales of weeks to many years (Nakar & Piran, 2011; Piran et al., 2013; Nakar, 2020). These phenomena are called radio flares or radio remnants and are in principle observable from all directions, whereas short GRBs can only be detected if the jet points towards the earth. In the context of r-process nucleosynthesis, short GRBs and potentially radio remnants are interesting to estimate the rates of mergers and to study the environments in which mergers occur. Also, short GRBs have been used as trigger to identify kilonova emission with GRB130603B being a famous example (Tanvir et al., 2013; Berger et al., 2013).

Neutrinos: Neutron star mergers are very strong emitters of neutrinos since the forming remnant features temperatures of a few to several 10 MeV. Typical neutrino luminosities are of the order of a few 10^{52} to 10^{53} erg/s (Ruffert et al., 1997; Rosswog et al., 1999; Sekiguchi et al., 2011, 2015; Palenzuela et al., 2015; Foucart et al., 2016; Lehner et al., 2016; Radice et al., 2016; Bovard et al., 2017; Radice et al., 2018; Ardevol-Pulpillo et al., 2019; Vincent et al., 2020; Combi & Siegel, 2022). The emission of electron anti-neutrinos dominates over electron neutrinos and heavy-flavor neutrinos. Mean energies of the neutrinos are roughly 15 MeV. Although these numbers are roughly comparable to those of CCSNe (see Section 2), it is unlikely to directly detect a neutrino signal from a NS merger. The reason is that COMs are much less frequent than SNe and will thus on average take place at larger distances. While neutrino signals from CCSNe can be detected for events from the neighborhood of the Milky Way, it is statistically very unlikely that a COM will occur at a similar distance. Hence, the neutrino emission of COMs should not be considered as direct messenger but it does have a very strong observational imprint on the kilonova by determining the electron fraction of the ejecta and thus their opacity.

There is also the possibility that high-energy neutrinos (in the range of $10^{13} - 10^{17}$ eV) are produced in the relativistic jet of a short gamma-ray burst (Waxman & Bahcall, 1997; Tamborra & Ando, 2016; Pitik et al., 2021), but their production depends sensitively on the jet properties and has not been confirmed by IceCube Neutrino Observatory detections yet.

3.5 Observations: GW170817 and more

There is a general agreement in the astrophysical community that the very first measurement of a NS merger with GWs marks a breakthrough. Not only it was the first unambiguous detection of a nearby NS merger but also it was a multi-messenger observation with electromagnetic emission discovered throughout the whole electromagnetic spectrum from gamma-rays to radio. The interpretation of these observations settled many open questions in the context of COMs and in particular gave new insights into the properties of high-density matter, r-process nucleosynthesis, and the connection between mergers and high-energy phenomena such as short GRBs.

System parameters and EoS constraints: In August 2017, the network of GW instruments consisting of Advanced LIGO and Advanced Virgo detected a NS merger at a distance of about 40 Mpc (Abbott et al., 2017b, 2019). The event was dubbed GW170817 with the number referring to the detection date. The system had a chirp mass of $1.186 M_{\odot}$ and a binary mass ratio of $0.7 < q = M_1/M_2 < 1$ (Abbott et al., 2019). These parameters correspond to the mass ranges of $1.17 - 1.36 M_{\odot}$ and $1.36 - 1.59 M_{\odot}$ for the individual component masses of the binary. These masses are in line with those typically found in NS binary systems that are observed by radio telescopes. The spins of the individual NSs are consistent with zero but generally not very well constrained for the analysis adopting a high-spin prior.

The combined tidal deformability $\tilde{\Lambda}$ was determined to be roughly in the range of $100 < \tilde{\Lambda} < 700$ (Abbott et al., 2019). The exact value depends to some extent on the waveform models and the chosen priors which are employed in the parameter estimation. This is a relatively broad range of values for $\tilde{\Lambda}$, but in particular the upper limit represents a valuable constraint on the properties of high-density matter. The tidal deformability scales tightly with the NS radius, and the observation can thus be translated to an upper limit on NS radii (Abbott et al., 2018; De et al., 2018). Note that this conversion is not significantly affected by the fact that the binary mass ratio was not well constrained, because for the given mass range NS radii are expected not to vary strongly. In essence, the inspiral GW signal constrains NS radii to be smaller than about 13.5 km and thus excludes very stiff nuclear matter. The measurement can be directly converted to a bound on the EoS, namely the pressure at twice nuclear saturation density should not exceed a value of about 6.2×10^{34} dyn/cm². The exact numbers of these limits depend on details and assumptions of the analysis (Abbott et al., 2018; Chatziioannou, 2020).

No postmerger GW signal was detected for GW170817 (Abbott et al., 2019). With the instrumental sensitivity at that time this is expected even if a postmerger GW signal was present. Hence, the non-detection does not permit any conclusions on the outcome of the merger, where the measurement of postmerger GWs represents a smoking-gun signature for the formation of a NS remnant as opposed to a direct gravitational collapse. With further improvements of the sensitivity in the kHz range in the future, the detection of postmerger GWs will come within reach and promises additional EoS constraints and insights into the merger outcome (e.g. Torres-Rivas et al., 2019).

Kilonova detection: Important information on the EoS but also on r-process nucleosynthesis was inferred from the identification of the electromagnetic counterpart in the optical (Soares-Santos et al., 2017; Cowperthwaite et al., 2017; Nicholl et al., 2017; Chornock et al., 2017; Arcavi et al., 2017; Smartt et al., 2017; Shappee et al., 2017; Kilpatrick et al., 2017; Pian et al., 2017; Kasliwal et al., 2017; Tanvir et al., 2017; Villar et al., 2017; Waxman et al., 2018, 2019). The GW signal provided a coarse localization of the event on the sky within an area of a few 10 square degrees and triggered an intensive follow-up campaign with optical telescopes. The electromagnetic counterpart was found about 11 hours after the GW detection and pinpointed the merger to a position near the galaxy NGC 4993, which has a distance consistent with the luminosity distance inferred from the GW amplitude and was thus identified as host galaxy of GW170817. In the following days and weeks essentially all major astronomical facilities including X-ray and radio telescopes observed the electromagnetic counterpart of GW170817 (Abbott et al., 2017a). The astronomical transient is referred to as AT 2017gfo. Independent of the GW detection a GRB was observed by the Fermi and INTEGRAL satellites about 1.7 seconds after the coalescence (Goldstein et al., 2017; Savchenko et al., 2017; Abbott et al., 2017c), which on its own would probably not have enabled the discovery of the kilonova because of the less well constrained position on the sky.

The bolometric luminosity of the kilonova, i.e. the total energy emission in the optical, ultraviolet and infrared, faded from 10^{42} erg/s to 10^{40} erg/s within about 10 days. The transient was observed in many different filter bands and several high-quality spectra, e.g. with the Very Large Telescope (VLT) X-Shooter instrument, have been recorded at different epoches (Pian et al., 2017; Smartt et al., 2017). The radiation resembled a black-body emission as expected for a kilonova with the peak of the emission shifting from initially bluish colors to red and infrared. See also Villar et al. (2017); Waxman et al. (2018) for a compilation of the different observations.

The color, the temporal evolution, and the luminosity of the transient are in excellent agreement with predicted properties of a kilonova, i.e. r-process heated, rapidly expanding outflows composed of heavy elements. Qualitatively the properties of the electromagnetic counterpart were clearly distinguished from other known astronomical transient phenomena such as, in particular, SNe. Overall, the observations provide very compelling evidence that r-process nucleosynthesis took place in the outflow of GW170817. NS mergers are therefore the first and so far only confirmed astrophysical site of r-process element formation.

As already indicated in the previous section, numerous models exist to describe the kilonova emission with different degrees of sophistication. Some of these models have been employed to extract the physical parameters of the ejecta, e.g., their mass, outflow velocity, and composition or opacity. Clearly, the interpretation and the inferred ejecta parameters depend on the details of these analyses and their assumptions.

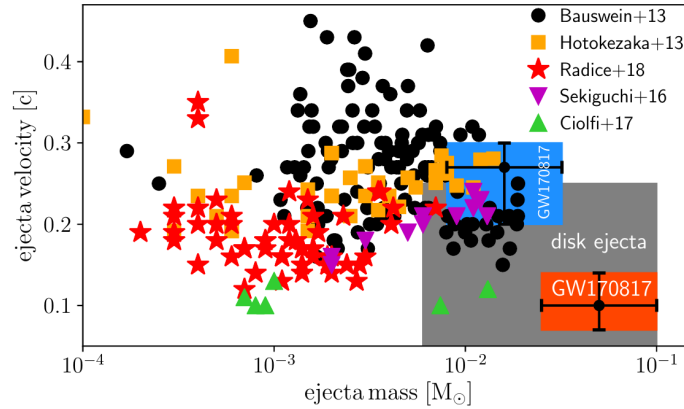


Fig. 19 Compilation of simulation results for the dynamical ejecta mass and outflow velocity in comparison to inferred values from the electromagnetic counterpart of GW170817. Figure from Siegel (2019); with kind permission of The European Physical Journal (EPJ)

Many models interpret the data as to show a faster moving blue component and a red low-velocity ejecta component (e.g. Cowperthwaite et al., 2017; Chornock et al., 2017; Evans et al., 2017; Kasen et al., 2017; Kasliwal et al., 2017; Kilpatrick et al., 2017; Perego et al., 2017; Tanaka et al., 2017; Villar et al., 2017; Smartt et al., 2017; Tanvir et al., 2017; Troja et al., 2017; Rosswog et al., 2018; Bulla, 2019). The colors “blue” and “red” refer to the opacity of the components and thus to their respective lanthanide fraction, which sensitively affects the opacity and is mostly determined by the electron fraction of the ejecta. These models obtain a velocity of 0.2–0.3 c and mass in the range of about $0.02 M_{\odot}$ for the blue component and $v \sim 0.15 c$ and a mass of roughly $0.03 M_{\odot}$ for the red component. However, also models with only a single component involving a range of velocities in combination with the time evolution of the opacity as a result of the temperature and density evolution do fit the data well (Smartt et al., 2017; Waxman et al., 2018). Essentially all models do infer a total ejecta mass of about 0.03 to $0.06 M_{\odot}$. See, e.g., Côté et al. (2018) for a compilation of literature results on the ejecta mass. Notably these numbers are too high to be explained by the dynamical ejecta alone if one considers literature values from simulations. Figure 19 compares estimated ejecta properties of GW170817 with data from simulations for dynamical mass ejection (Siegel, 2019).

The interpretation of the color evolution of the kilonova as a result of the opacity and the lanthanide content hints to the underlying nucleosynthesis and electron fraction of the ejecta. Lanthanide-poor conditions imply that the r -process did not proceed to very high mass numbers, i.e. a blue component would not have a typical solar r -process abundance pattern including a significant fraction of lanthanides. A red, high-opacity ejecta component may be associated with the formation of heavy r -process elements in a low- Y_e environment. This provides some clues on the composition of the outflow (Fig. 20).

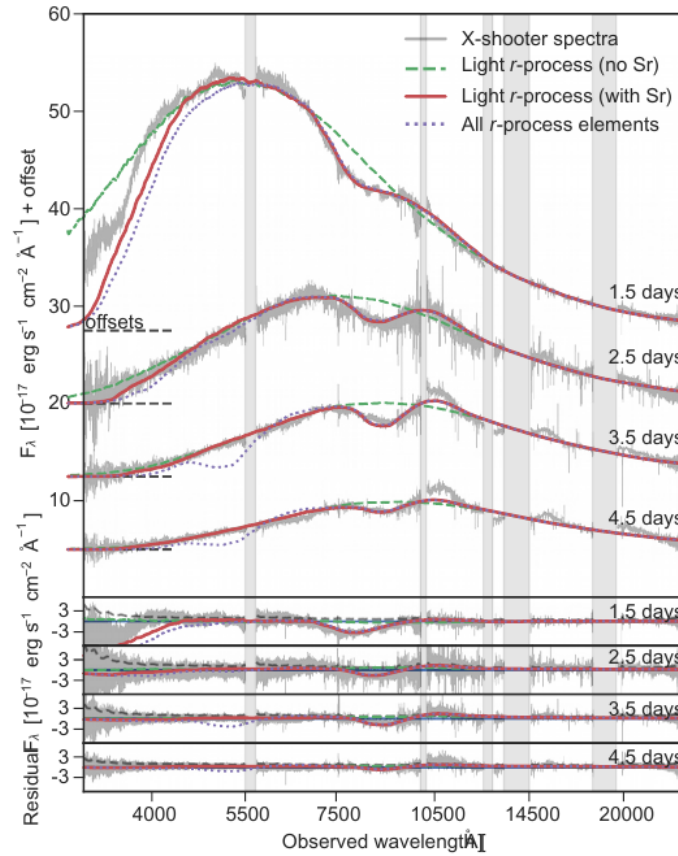


Fig. 20 Spectra of the electromagnetic counterpart of GW170817 at different epochs. The figure shows data from VLT/X-Shooter, which roughly reveal black-body emission with additional features imprinted. The emission peak shifts to redder colors. Credit: D. Watson & J. Selsing from data taken at the ESO telescopes. See also Watson et al. (2019)

A direct probe of the elemental distribution may be obtained from interpreting spectral signatures of the kilonova (Pian et al., 2017; Smartt et al., 2017). While

the emission roughly resembles a black body, the spectrum of AT2017gfo clearly contains additional spectral features. For instance, the spectrum at 1.5 days shows a prominent absorption feature at 810 nm (Fig. 20). This has been interpreted by Watson et al. (2019) to be blue-shifted strontium lines moving with a velocity of about 0.25 to 0.3 c , see also Domoto et al. (2021); Gillanders et al. (2022); Domoto et al. (2022); Vieira et al. (2022). At later epochs the dip in the spectrum moves to larger wavelengths indicating a slower expansion velocity consistent with the expectation that deeper ejecta layers become visible at later times. Strontium is produced by the slow neutron-capture process as well as the r-process. With a mass number of about $A \approx 88$ strontium is a rather light r-process element indicating the presence of an ejecta component with relatively high Y_e , which is required to create such lighter elements.

More merger detections: GW170817 was clearly an outstanding event, the interpretation of which is still ongoing. But there were about a handful more GW observations of COMs likely involving NSs apart from the numerous BH-BH binary detections (Abbott et al., 2021; Abbott et al., 2021). For none of the detections an electromagnetic counterpart was found, which, considering the estimated distances, did not come as a surprise. From a nucleosynthesis point of view these events may not be very informative.

However, considering the small number of events, the inferred binary masses are somewhat surprising as they do not follow the commonly expected distribution of NS masses in compact binaries. For instance, GW190425 had an unusually high total mass of about $3.4 M_\odot$ (Abbott et al., 2020). Here, “unusual” refers to the mass typically found in double NS systems containing a pulsar, which have system masses in the range of about 2.7 to $2.8 M_\odot$ (e.g. Lattimer, 2012). Also GW190814 was unusual with one binary component having a mass of $23.2 M_\odot$ (obviously a BH) and the companion having a mass of $2.6 M_\odot$ (Abbott et al., 2020b). For the latter it is not obvious whether it was a BH or a NS. If it was a NS, it either implies a rather high maximum NS mass M_{\max} or it was rapidly spinning, which may challenge typical evolution scenarios and is surprising since among the few thousand known NSs none is rotating that fast. If the companion was a BH, the detection is challenging the notion that there may be a “mass gap” between NSs and BHs. There are also some candidate events with relatively low signal-to-noise ratio, which were not classified as confirmed detections.

In any case the next observing runs of the GW detector network are very likely to discover several more COMs with the prospect to find electromagnetic counterparts as the instrumental sensitivity increases and thus provides more accurate localizations. Also the capabilities of optical and infrared observatories are increasing with, for instance, the James Webb Space Telescope or the European Extremely Large Telescope, which promise better observational data of more distant events.

While GW detections are the primary tool to identify nearby COMs, it should be mentioned that also short GRBs can in principle be used to infer kilonova data from on average more distant events. For example, GRB130603B features excess emission in the afterglow light curve of the GRB, which is consistent with kilonova emission from a few $0.01 M_\odot$ of ejecta (Tanvir et al., 2013; Berger et al., 2013).

3.6 *Equation-of-state impact*

Motivation: As already mentioned, the EoS is the entity which most sensitively affects the merger dynamics and thus the mass ejection apart from the binary masses. Hence, the nucleosynthesis and the kilonova carry a strong imprint of the EoS, while the GW inspiral signal constrains the binary masses with good accuracy for near-by mergers. Addressing the impact of the EoS on mass ejection and nucleosynthesis serves two purposes, which are connected but follow different directions.

(1) While GWs do provide information on the EoS (Sect. 3.4), there is still need for additional and complementary constraints from interpreting kilonovae, which is only possible through the modeling and interpretation of these transients. A growing number of studies in fact combines constraints from different messengers including GWs and kilonovae (e.g. Margalit & Metzger, 2017; Bauswein et al., 2017; Shibata et al., 2017; Radice et al., 2018; Coughlin et al., 2018; Ruiz et al., 2018; Most et al., 2018; Rezzolla et al., 2018; Capano et al., 2020; Dietrich et al., 2020; Bauswein et al., 2021; Raaijmakers et al., 2021; Huth et al., 2022).

(2) In turn, adopting current knowledge about the EoS from merger observations, from other astronomical measurements, from laboratory experiments or from theoretical developments, the comprehension of the EoS influence is critical to predict the outcome of COMs. This is relevant to assess the total production of r-process elements throughout the cosmic history and to interpret for instance the abundances of metal-poor, i.e., old stars in the Milky Way and its neighborhood. The nucleosynthetic yields per merger event are a specific input for modeling the chemical evolution of the Galaxy and the Universe (see, e.g., Cowan et al., 2021) for a review and specific references on chemical evolution aspects). Clearly, these far-reaching goals require more information beyond the EoS influence such as the mass distribution of the binary populations, their merger rates and their delay times until coalescence. These ingredients may be obtained from a large sample of future merger observations and their interpretation. Also, a theoretical understanding of the EoS dependence is necessary to predict and bracket the possible range of kilonova properties. This may be useful for example in blind astronomical surveys, i.e., observing campaigns which are not triggered by specific events, to identify and classify COMs.

Simulations: The influence of the EoS on the mass ejection is only accessible through numerical simulations. Considering the complexity of the mass ejection through different channels, the modeling of the ejecta and their EoS dependence represents a major challenge and is still subject to uncertainties as described in Section 3.2. To date mass ejection in COMs is qualitatively very well understood and the EoS dependence of several properties is quantitatively described, albeit usually within some uncertainty range, which on its own may not yet be fully quantified. At the same time it should be appreciated that there exists only a small subset of simulations which cover the whole mass ejection process from the dynamical merger phase to the late secular postmerger evolution in a fully consistent calculation or connect the different phases of mass ejection by some sort of mapping between different codes (e.g., Perego et al., 2014; Just et al., 2015; Martin et al., 2015; Fernández et al., 2017; Hossein Nouri et al., 2018; Fujibayashi et al., 2020b; Most et al., 2021;

Hayashi et al., 2022; Fujibayashi et al., 2022). But generally, there is some decoupling between the modeling of different merger stages, in particular in large-scale surveys based on many calculations with a systematic variation of the input parameters like binary masses and EoS. For this reason the discussion below follows the current status in the literature and addresses specific aspects and questions of the EoS and binary-mass dependence referring to Section 3.2 for the detailed description of the different mass ejection channels. The discussion largely focuses on the ejecta mass as one of the most important properties and the quantity that shows the largest variations with respect to the EoS influence.

Describing the EoS impact quantitatively requires not only to numerically quantify ejecta parameters but also to define characteristics of the EoS to express functional dependencies. EoSs used in merger simulations are derived within different models and there is no commonly used overarching framework to define universal model parameters. However, it is possible to extract nuclear parameters from the EoS such as the symmetry energy and its slope or the incompressibility. These parameters are useful to describe the EoS but are only characteristic of a certain density range (at saturation density). Hence, it is obligatory to employ the stellar properties of cold, non-rotating NSs to characterize a given EoS (but see Most & Raithel, 2021, for an exploration of the impact of the slope of the symmetry energy). Stellar parameters such as the radius, compactness, tidal deformability or maximum mass are uniquely linked to the EoS through the Tolman-Oppenheimer-Volkoff equations of stellar structure. As integrated bulk properties these quantities characterize well the behavior of the EoS across a larger density range and, in particular, they are useful to describe the dynamics of a COM.

Stellar parameters of cold, non-rotating NSs are determined by the cold EoS in neutrinoless beta-equilibrium, whereas COMs reach finite temperatures and finite neutrino chemical potentials during merging. Therefore, in simulations the full temperature and composition dependence of the EoS has to be taken into account together with neutrino transport. Still, the EoS slice at $T = 0$ and beta-equilibrium describes the basic properties of the model, where finite temperature and composition changes add moderate deviations.

Merger outcome, threshold mass for prompt collapse: The EoS affects mass ejection and r-process nucleosynthesis in many, partially subtle ways. The most basic influence is on the immediate outcome of a NS merger, i.e., the EoS dictates if for a given binary mass configuration a NS remnant or a BH-torus system forms (Shibata & Taniguchi, 2006; Baiotti et al., 2008). This obviously has significant impact on the ejecta properties, since it influences the very early dynamical mass ejection and it determines if there is a phase of mass ejection from a NS remnant at all. This very basic characteristic of a NS merger is quantitatively described by the threshold binary mass M_{thres} for prompt collapse (Hotokezaka et al., 2011; Bauswein et al., 2013). Systems with a total binary mass M_{tot} exceeding M_{thres} directly form a BH, whereas binaries with $M_{\text{tot}} < M_{\text{thres}}$ lead to the formation of an at least transiently stable rotating NS remnant.

Using numerical simulations M_{thres} is found to depend in a systematic way on the EoS, which can be expressed through stellar parameters of non-rotating NSs.

With good accuracy M_{thres} follows

$$M_{\text{thres}}(R_{1.6}, M_{\text{max}}, q) = c_1 M_{\text{max}} + c_2 R_{1.6} + c_3 + c_4 (1 - q)^3 M_{\text{max}} + c_5 (1 - q)^3 R_{1.6} \quad (30)$$

with $c_1 = 0.578$, $c_2 = 0.161$, $c_3 = -0.218$, $c_4 = 8.987$ and $c_5 = -1.767$ (Bauswein et al., 2021). In Equation (30) the EoS dependence is expressed through the maximum mass of non-rotating NSs, M_{max} , and the radius of a non-rotating NS with a mass of $1.6 M_{\odot}$. The latter may be replaced by other quantities like, for instance, the tidal deformability at a given mass, which similar to the radius is a measure of the NS compactness. The fact that M_{thres} correlates with M_{max} may not be surprising since M_{max} determines the threshold for BH formation of non-rotating NSs. Equation (30) also contains an explicit dependence on the binary mass ratio q . For small deviations from $q = 1$ the threshold mass does not change strongly compared to the equal-mass case. For systems with significant mass asymmetry, i.e. $q \lesssim 0.8$, the threshold mass is significantly reduced reflecting the fact that the merger remnant in this case features less total angular momentum and an angular momentum distribution with less rotation in the center. Based on these insights one may expect that generally NS merger remnants of asymmetric binaries are less stable as compared to the equal-mass case of the same total mass.

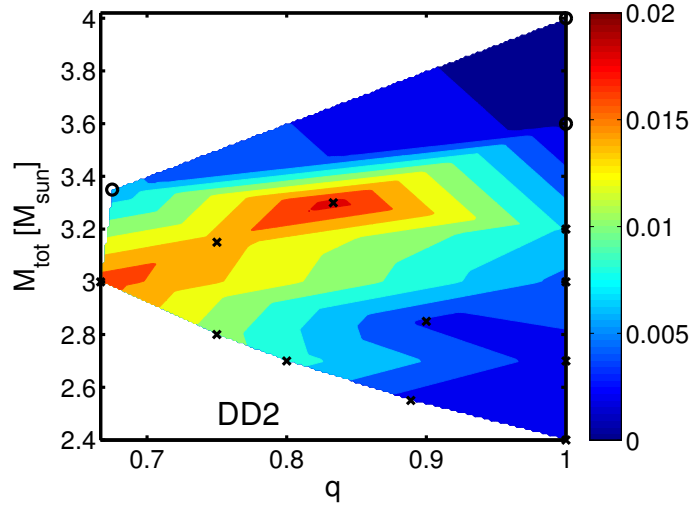


Fig. 21 Dynamical ejecta mass (color-coded in M_{\odot}) as function of the binary mass ratio q and the total binary mass M_{tot} . Figure from Bauswein et al. (2013); ©American Astronomical Society. Reproduced with permission

Dynamical ejecta dependencies: Already early studies of the impact of the EoS and binary masses on the dynamical ejecta identified basic dependencies by evaluating a large sample of simulations with different high-density models (Hotokezaka

et al., 2013b; Bauswein et al., 2013; Dietrich et al., 2017b). (i) For a fixed EoS the ejecta mass increases with the binary mass asymmetry. (ii) Typically, for a fixed EoS the ejecta mass mildly increases with the total binary mass. (iii) If a prompt collapse occurs ($M_{\text{tot}} > M_{\text{thres}}$), the dynamical ejecta mass is strongly reduced. These dependencies are visualized for an exemplary EoS model in Fig. 21. As described in more detail in Section 3.2, simulation results do show some uncertainties, which should be kept in mind when one quantitatively interprets such ejecta properties and relations. (iv) For a fixed binary mass configuration, soft EoSs typically lead to more ejecta, if the binary mass asymmetry is not too large and the system does not directly form a BH. Mergers with softer EoSs resulting in smaller NS radii collide with a larger impact velocity and feature more violent postmerger oscillations (see, e.g., Bauswein et al., 2013). This leads to enhanced mass ejection.

While all of these dependencies are physically understandable it should be emphasized that especially the EoS dependence is not an exact relation but features some scatter of at least several ten per cent.

Some studies have summarized these simulation results and dependencies by developing fit formulae, which provide the ejecta mass or other ejecta properties as functions of the binary masses and parameters describing the EoS, i.e., NS parameters (e.g. Dietrich & Ujevic, 2017; Coughlin et al., 2018; Krüger & Foucart, 2020; Nedora et al., 2022). Some of those models include results from several different sets of simulations, which on the one hand might trigger the question of consistency (different resolution, numerical treatment, physical effects, ways of defining and extracting ejecta) but on the other hand provides a better and more representative overview. Henkel et al. (2022) collect and review several of such fit formulae.

Following this study to exemplify the EoS dependence, Fig. 22 shows the ejecta mass as function of the NS radius of a $1.35 M_{\odot}$ NS. See e.g. Henkel et al. (2022) for more details. For this plot binary masses are chosen such that they represent the ones of GW170817 with the solid curves assuming an equal-mass binary and the dashed lines referring to a mass ratio of $q = 0.7$. The different colors refer to different fit formulae developed in the literature. It should be noted that additional assumptions and relations (Timmes et al., 1996; De et al., 2018; Bauswein et al., 2021) were adopted in order to compose the various fit formulae in a single plot like Fig. 22. For instance, some relations are not given as function of the NS radius or compactness but of the tidal deformability, which can be converted to a radius estimate using the relations of (e.g. De et al., 2018).

For equal-mass binaries the relations broadly agree with each other with the main difference being that the fit formula of Krüger & Foucart (2020) displays a reduction of ejecta mass for soft EoSs, i.e., models with small NS radii. Systems with a binary mass asymmetry show a significantly larger scatter, which results from the chosen simulation models entering the fit formula. Note that for the sake of clarity, Fig. 22 does not display error bars, which for some of the fit formulae have been estimated and are usually relatively large (several ten per cent). The importance of such fit formulae lies in the fact that they can be seen as a form of meta-study summarizing simulation results and that they can be employed to constrain EoS parameters, when ejecta properties such as the ejecta mass are estimated by an interpretation of

the kilonova (see above). Numerous studies have followed this route, often incorporating estimates of the ejecta velocity and including contributions from the secular ejecta (e.g., Coughlin et al., 2018, 2019; Radice & Dai, 2019; Capano et al., 2020; Dietrich et al., 2020; Breschi et al., 2021; Raaijmakers et al., 2021; Huth et al., 2022).

The fit formulae for the averaged ejecta velocities show that one typically expects an increase of the velocity for soft EoSs, i.e., small NS radii (e.g., Nedora et al., 2022). This may be expected because as argued before, those systems lead to a more violent merging and strongly excited remnant oscillations, which enhances the outflow velocity. There also seems to be the tendency that asymmetric binaries lead to somewhat smaller ejecta velocities for the same total mass and the same EoS model, which may again be explained by the remnant dynamics being less violent in these cases. Typical average outflow velocities are between roughly $0.15 c$ and $0.35 c$.

The electron fraction of the dynamical ejecta shows typically a broad distribution between about 0.05 and 0.45 with a mildly pronounced maximum in the range between 0.2 and 0.3 (e.g. Palenzuela et al., 2015; Sekiguchi et al., 2015; Foucart et al., 2016; Lehner et al., 2016; Radice et al., 2016; Bovard et al., 2017; Radice et al., 2018; Ardevol-Pulpillo et al., 2019; Combi & Siegel, 2022; Vincent et al., 2020). The distributions of Y_e exhibit a mild dependence on the EoS, but it is not straightforward to identify a clear systematic dependence. Tentatively the outflow becomes less neutron rich with larger binary mass asymmetry and with the EoS stiffness parameterized e.g. by the NS radius or its tidal deformability. Overall, there is a significant scatter in these tentative relations (see, e.g., the compilation in Nedora et al., 2022, and the fit formulae therein), and one should keep in mind that only simulations which include the reabsorption of neutrinos in some way can yield a reliable distribution of the electron fraction in the dynamical ejecta. Moreover, the variations in the distribution are so modest that the impact on the final r-process abundance patterns is usually small (Kullmann et al., 2022a; Radice et al., 2018). This can be seen in Fig. 18, which shows the outcome of nuclear network calculations for merger simulations with different EoSs and binary mass ratios. A rather robust feature in most simulations is that the electron fraction is higher in directions towards to poles where neutrino reabsorption is more effective (e.g. Palenzuela et al., 2015; Sekiguchi et al., 2015; Foucart et al., 2016; Lehner et al., 2016; Bovard et al., 2017; Radice et al., 2018; Ardevol-Pulpillo et al., 2019; Vincent et al., 2020; Combi & Siegel, 2022; Kullmann et al., 2022a).

Torus mass and secular ejecta: Another important and possibly even dominant component of the ejecta stems from the secular evolution of a torus around the central object (either a BH or a rotating NS). Identifying torus material and thus defining torus properties can be ambiguous before the gravitational collapse of the remnant, because one attempts to estimate the amount of matter escaping the forming BH, which may only form after some further dynamical evolution. Nonetheless, one can observe some clear dependencies of the torus mass (e.g. Shibata & Taniguchi, 2006; Oechslin & Janka, 2006; Oechslin et al., 2007; Hotokezaka et al., 2013b; Dietrich et al., 2017b; Radice et al., 2018). For the same EoS and the same total binary mass,

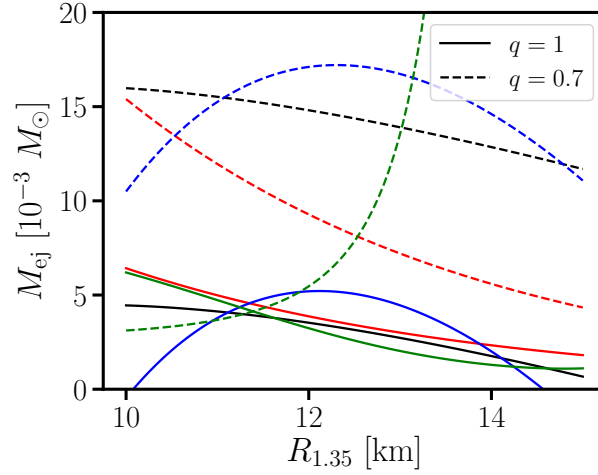


Fig. 22 Dynamical ejecta mass as function of the radius $R_{1.35}$ of a $1.35 M_{\odot}$ NS (representing the EoS dependence) as predicted by different fit formulae (black: Dietrich & Ujevic 2017; red: Coughlin et al. 2018; blue: Krüger & Foucart 2020; green: Nedora et al. 2022; additional assumptions are adopted to present all fit formulae as functions of $R_{1.35}$). A total mass of $2.73 M_{\odot}$ is assumed, where the solid curves refer to a mass ratio of $q = 1$ and the dashed curves to $q = 0.7$. This roughly spans the possible range of binary mass ratios of GW170817

asymmetric systems lead to more massive tori, which is understandable from the fact that these mergers lead to a tidal disruption of the lighter binary component with its larger fraction of the system's orbital angular momentum. For fixed binary masses, mergers with stiffer EoSs corresponding to larger NS radii typically result in higher torus masses. These systems are less strongly bound and they are associated with longer remnant life times and hence there is more time to redistribute angular momentum from the central regions of the remnant to the outer layers. Typical torus masses range from several $10^{-3} M_{\odot}$ to a few $0.1 M_{\odot}$ if no direct collapse occurs.

The torus mass is strongly reduced for systems where prompt BH formation takes place (e.g., Shibata & Taniguchi, 2006; Just et al., 2015; Radice et al., 2018). In these cases the torus mass may not exceed $10^{-3} M_{\odot}$ unless the binary system is strongly asymmetric such that the tidal disruption of the lighter component directly produces a massive torus in the merging phase. If the remnant survives for only a short period of time, the torus mass can easily reach $0.1 M_{\odot}$ especially for asymmetric binaries (see also Kiuchi et al., 2019) for a detailed exploration of the transition region). In combination with the considerations about the dynamical ejecta, this suggests a pronounced difference in the kilonova properties of prompt-collapse and delayed-collapse systems and emphasizes the importance to understand the exact threshold mass for direct BH formation.

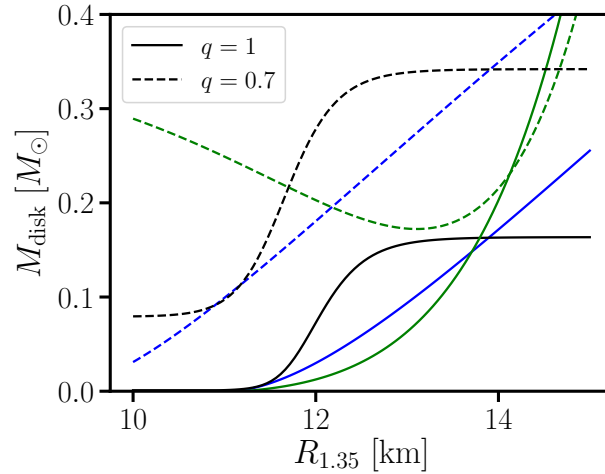


Fig. 23 Torus mass as function of the radius $R_{1.35}$ of a $1.35 M_{\odot}$ NS (representing the EoS dependence) as predicted by different fit formulae (black: Dietrich et al. 2020; blue: Krüger & Foucart 2020, green: Nedora et al. 2022; additional assumptions are adopted to present all fit formulae as functions of $R_{1.35}$). A total mass of $2.73 M_{\odot}$ is assumed, where the solid curves refer to a mass ratio of $q = 1$ and the dashed curves to $q = 0.7$. This roughly spans the possible range of binary mass ratios of GW170817

Fit formulae have also been developed for the torus mass expressing the binary mass and EoS dependence (e.g. Radice et al., 2018; Dietrich et al., 2020; Krüger & Foucart, 2020; Nedora et al., 2022). The differences between different relations that are available in the literature can be significant (factor two). See, e.g., Henkel et al. (2022) for a more detailed discussion and references to various formulae. It is clear that the different relations are not only affected by which function is chosen for the fit, but in particular also by the set of models included. Figure 23 displays torus masses obtained from different fit formulae. Again, there is a rough agreement between the different relations for $q = 1$, while there is a larger scatter for asymmetric binaries.

Most of the torus material will be accreted onto the BH on a longer time scale. Only a fraction of roughly 20 per cent becomes gravitationally unbound during this evolution (Just et al., 2015; Fernández et al., 2015; Siegel & Metzger, 2018; Fernández et al., 2020; Fujibayashi et al., 2020a; Just et al., 2022a). For typical torus masses of $\sim 0.1 M_{\odot}$ one can thus expect a few $10^{-2} M_{\odot}$ of torus ejecta. Hence, the amounts of torus ejecta may exceed the dynamical ejecta mass (see also Fig. 16).

It is important to note that it is challenging to compute the exact fraction of unbound torus material since it depends on a detailed modeling of magneto-hydrodynamic processes and of neutrino transport effects. In addition, the fraction of the torus which is ejected, does depend on physical parameters of the system and

through this on the initial binary masses and the EoS. Just et al. (2022a) for instance provide a systematic study of the impact of the torus properties on the ejecta as well as an assessment of various modeling ingredients. For instance, more massive or faster spinning BHs increase the fraction of the torus material becoming unbound. Similarly, the average electron fraction of the ejected torus matter is dependent on the properties of the system. Typically, the electron fraction of the torus ejecta is slightly above 0.3 and thus the r-process creates predominantly nuclei of the first and second r-process abundance peaks, whereas species with higher mass number are less abundant in these outflows.

Phase transition to deconfined quark matter: A particular EoS aspect which is hardly explored yet, is the impact of a hadron-quark phase transition on the mass ejection. If deconfined quark matter occurs in a NS, it can alter the stellar structure significantly and thus, in principle, also affect the merger dynamics and mass ejection. Current studies of the dynamical phase suggest that there may not be an unambiguous imprint in the sense that the occurrence of a phase transition would lead to a characteristic increase or decrease of the mass ejection or significantly alter the elemental abundance pattern (Bauswein et al., 2019; Prakash et al., 2021). But more work is required on this aspect.

EOS constraints: The EoS dependence as discussed is the basis for various constraints on the properties of NSs and high-density matter, which are derived from the multi-messenger observation of GW170817. These approaches can be roughly classified according to how and which information from the kilonovae is made use of. The methodology and the detailed assumptions within these classes partially differ, which if why the quantitative results can show some differences. Also, the association of a specific work to one of these classes below is not always unambiguous.

(i) Some works conclude that because of the brightness of the kilonova no direct BH formation took place in GW170817, and, hence, the threshold binary mass for prompt BH formation is larger than the measured total binary mass of GW170817. This can be translated into a lower bound on NS radii or the tidal deformability since more compact NSs yielding a prompt collapse would lead to a dimmer electromagnetic emission (Bauswein et al., 2017; Radice et al., 2018; Most et al., 2018; Bauswein et al., 2019; Köppel et al., 2019; Capano et al., 2020; Bauswein et al., 2021). In summary, this argument leads to the conclusion that nuclear matter cannot be very soft and NS radii should be roughly larger than about 11 km.

(ii) A number of studies rely on the conclusion that GW170817 did form a NS remnant and employ additional information or assumptions, e.g., from the detailed properties of the ejecta or the observation of a short GRB about 2 seconds after merging. The latter suggest that a BH formed at some point during the remnant evolution (Margalit & Metzger, 2017; Shibata et al., 2017; Rezzolla et al., 2018; Ruiz et al., 2018; Margalit & Metzger, 2019; Capano et al., 2020). This can be converted to an upper limit on the maximum mass M_{\max} of non-rotating NSs, which should be smaller than about $2.2 M_{\odot}$.

(iii) Another class of interpretations of the observational data directly connects the properties of the kilonova light curve and inferred ejecta properties to NS parameters employing empirical relations, which are obtained from simulations (e.g.

Coughlin et al., 2018, 2019; Radice & Dai, 2019; Dietrich et al., 2020; Breschi et al., 2021; Raaijmakers et al., 2021; Huth et al., 2022). These studies are based on fit formulae as described above. Clearly, this approach is in comparison more ambitious as the fit formulae include significant uncertainties and, moreover, the inference of ejecta properties from the observations introduces additional uncertainties. The bounds on NS radii are roughly in the range between 11 and 13 km. Note that most of the studies above actually combine EoS constraints from different sources, including, for instance, observations by NICER, the GW inspiral signal, theoretical calculations of nuclear matter properties, heavy-ion collisions, pulsar observations or the limits derived by the studies listed in class (ii).

3.7 Outlook - Mergers

These considerations of the different ejecta components show that the total yields, i.e., the combination of dynamical ejecta and secular ejecta from a massive NS evolution and the disk wind, depend sensitively on the EoS and the binary masses. The discussion also indicates that it is not easy to exactly determine the specific contributions of the individual mass ejection channels and thus the total yields of a given event. To date only a subset of models is striving for an inclusion or combination of all ejecta components, and a fully consistent, systematic broad survey is still missing (e.g., Perego et al., 2014; Just et al., 2015; Martin et al., 2015; Fernández et al., 2017; Hossein Nouri et al., 2018; Fujibayashi et al., 2020b; Most et al., 2021; Fujibayashi et al., 2022). Some of these studies (e.g., Fujibayashi et al., 2022) indicate that not every merger event may produce nucleosynthetic yields that follow the solar distribution, although some models result in a solar abundance pattern over a wide range of mass number. For instance, the calculations of Fujibayashi et al. (2022) suggest that the remnant life time may affect the abundance distribution and hence the nucleosynthetic output depends on the binary masses. It is clear that future work should further improve the modeling of individual ejecta components but in particular address how those can be consistently combined. Also, there is a growing number of studies that consider the impact of different types of possible neutrino flavor conversions on the nucleosynthesis in a merger environment. This aspect could not be covered here, and the reader is referred to the literature, e.g., Zhu et al. (2016); Malkus et al. (2016); Wu & Tamborra (2017); Richers et al. (2021); Li & Siegel (2021); Just et al. (2022) (and references therein).

Future GW detections of COMs and associated observations of electromagnetic counterparts will provide valuable information on the nucleosynthesis in these events. These measurements will improve the current estimates of the merger rate in the local Universe and the distribution of masses within the binary population. Also the identification of host galaxies can help to better understand the environments of mergers. This may possibly also provide clues on delay times until merging and kick velocities. The GW signal alone or in combination with the electromagnetic counterparts will further constrain the EoS and NS properties. More kilonova ob-

servations in combination with more advanced models will allow to determine bulk ejecta properties like their masses and potentially the elemental composition of the outflow. Combining this information will provide a more comprehensive picture of the nucleosynthetic yields of COMs clarifying whether mergers produce r-process elements with a solar distribution and whether they are the dominant source of r-process elements.

4 Summary and perspectives

The phenomena and multi-messenger signals connected to CCSNe and COMs described in this chapter render these violent astrophysical events superb and unique cosmic laboratories for nuclear physics and astro-particle physics, especially for testing and exploiting the processes in high-density matter at temperatures up to about 100 MeV. Neutrinos, GWs, and the products of explosive nucleosynthesis carry information of the physics inside and in the close vicinity of the hot NSs that are formed or collide in such environments. Their computational modeling in three dimensions, even including general relativity and magnetic fields, has made enormous progress over the past decade, and basic dependencies of these messengers on the properties of the nuclear EoS begin to emerge from systematic studies. However, further improvements of the models are needed for high-fidelity predictions of neutrinos and GWs, for example with respect to the numerical resolution especially in magnetohydrodynamic simulations or concerning the treatment of the neutrino transport, which still lags behind state-of-the-art CCSN models in the majority of elaborate COM models (e.g., Foucart, 2022, and references therein). Further theoretical exploration is also needed to solve the nagging problem of potential consequences of neutrino-flavor oscillations in the dense media of newly born and colliding NSs. Successively improved computational modeling and a deeper fundamental understanding of the neutrino physics will ultimately also permit to reliably connect the electromagnetically observable emission with the properties of the nuclear and super-nuclear EoS of hot NS matter, which governs the dynamical evolution, ejecta mass, neutrino production, and thus also the nucleosynthetic outputs as well as light curves, spectra, X-ray, and γ -ray signals of the explosive events.

Not being enshrouded by solar masses of stellar material, COMs may offer the cleaner astrophysical sites for addressing these questions, and in the era of GW astronomy they are certainly the more frequent observable multi-messenger sources compared to CCSNe. One COM per decade seen in GWs and electromagnetic emission seems likely and even a few events in this time span may be possible, whereas neutrinos and GWs from CCSNe will be measurable only for a stellar death in the Milky Way and its close cosmic neighborhood. With the considerable recent progress in the numerical model building, however, even the historical neutrino detection connected to SN 1987A has gained new interest and relevance for deriving tighter constraints on nuclear and particle processes in hot NS environments (e.g., Bollig et al., 2020; Caputo et al., 2022; Fiorillo et al., 2022), and the possible

detection of a NS in SN 1987A (Cigan et al., 2019; Page et al., 2020) will further propel these potentials. Moreover, CCSNe are enormously diverse and multifaceted producers of chemical elements and the far more abundant cosmic phenomena (presently 1–2 events per century in Milky Way type galaxies compared to maybe a few events per 100,000 years for COMs). Both circumstances define the outstanding role of SNe for the chemical evolution of galaxies and the creation of stars, planets, and life in the Universe. A next Galactic CCSN or stellar BH formation will happen, and we should get prepared for maximizing the harvest from the flood of its data.

Acknowledgements HTJ is grateful for support by the Deutsche Forschungsgemeinschaft (DFG, German Research Foundation) through Sonderforschungsbereich (Collaborative Research Center) SFB 1258 “Neutrinos and Dark Matter in Astro- and Particle Physics (NDM)” and under Germany’s Excellence Strategy through Cluster of Excellence ORIGINS (EXC-2094)-390783311. AB acknowledges support by the European Research Council (ERC) under the European Union’s Horizon 2020 research and innovation program under grant agreement No. 759253, support by DFG–Project-ID 279384907–SFB 1245 and DFG–Project-ID 138713538–SFB 881 (“The Milky Way System”, subproject A10) and support by the State of Hesse within the Cluster Project ELEMENTS.

References

- Abbar, S., Capozzi, F., Glas, R., Janka, H. T., & Tamborra, I. 2021, *Physical Review D*, 103, 063033, doi: 10.1103/PhysRevD.103.063033
- Abbott, B. P., Abbott, R., Abbott, T. D., & et al. 2017a, *Astrophys. J. Lett.*, 848, L12, doi: 10.3847/2041-8213/aa91c9
- , 2020, *Astrophys. J. Lett.*, 892, L3, doi: 10.3847/2041-8213/ab75f5
- Abbott, B. P., Abbott, R., Abbott, T. D., et al. 2017b, *Phys. Rev. Lett.*, 119, 161101, doi: 10.1103/PhysRevLett.119.161101
- , 2018, *Phys. Rev. Lett.*, 121, 161101, doi: 10.1103/PhysRevLett.121.161101
- , 2019, *Physical Review X*, 9, 011001, doi: 10.1103/PhysRevX.9.011001
- , 2017c, *Astrophys. J. Lett.*, 848, L13, doi: 10.3847/2041-8213/aa920c
- Abbott, B. P., Abbott, R., Abbott, T. D., et al. 2017, *Nature*, 551, 85, doi: 10.1038/nature24471
- , 2020a, *Living Reviews in Relativity*, 23, 3, doi: 10.1007/s41114-020-00026-9
- Abbott, R., et al., The LIGO Scientific Collaboration, the Virgo Collaboration, & the KAGRA Collaboration. 2021, arXiv e-prints, arXiv:2111.03606. <https://arxiv.org/abs/2111.03606>
- Abbott, R., Abbott, T. D., Abraham, S., et al. 2020b, *Astrophys. J. Lett.*, 896, L44, doi: 10.3847/2041-8213/ab960f
- , 2021, *Physical Review X*, 11, 021053, doi: 10.1103/PhysRevX.11.021053
- Acernese, F., Agathos, M., Agatsuma, K., et al. 2015, *Classical and Quantum Gravity*, 32, 024001, doi: 10.1088/0264-9381/32/2/024001
- Alekseev, E. N., Alekseeva, L. N., Volchenko, V. I., & Krivosheina, I. V. 1987, *Soviet Journal of Experimental and Theoretical Physics Letters*, 45, 589
- Aloy, M. Á., & Obergaulinger, M. 2021, *Mon. Not. R. Astron. Soc.*, 500, 4365, doi: 10.1093/mnras/staa3273
- Amaro-Seoane, P., Andrews, J., Arca Sedda, M., et al. 2022, arXiv e-prints, arXiv:2203.06016. <https://arxiv.org/abs/2203.06016>

- Antoniadis, J., Freire, P. C. C., Wex, N., et al. 2013, *Science*, 340, 448, doi: 10.1126/science.1233232
- Arcavi, I., Hosseinzadeh, G., Howell, D. A., et al. 2017, *Nature*, 551, 64, doi: 10.1038/nature24291
- Arcones, A., Fröhlich, C., & Martínez-Pinedo, G. 2012, *Astrophys. J.*, 750, 18, doi: 10.1088/0004-637X/750/1/18
- Ardevol-Pulpillo, R., Janka, H. T., Just, O., & Bauswein, A. 2019, *Mon. Not. Roy. Astron. Soc.*, 485, 4754, doi: 10.1093/mnras/stz613
- Arnett, W. D. 1980, *Astrophys. J.*, 237, 541, doi: 10.1086/157898
- Arnould, M., & Goriely, S. 2020, *Progress in Particle and Nuclear Physics*, 112, 103766, doi: 10.1016/j.pnpnp.2020.103766
- Arnould, M., Goriely, S., & Takahashi, K. 2007, *Physics Reports*, 450, 97, doi: 10.1016/j.physrep.2007.06.002
- Arzoumanian, Z., Brazier, A., Burke-Spolaor, S., et al. 2018, *Astrophys. J. Supp.*, 235, 37, doi: 10.3847/1538-4365/aab5b0
- Aso, Y., Michimura, Y., Somiya, K., et al. 2013, *Phys. Rev. D*, 88, 043007, doi: 10.1103/PhysRevD.88.043007
- Baiotti, L., Giacomazzo, B., & Rezzolla, L. 2008, *Phys. Rev. D*, 78, 084033, doi: 10.1103/PhysRevD.78.084033
- Baiotti, L., & Rezzolla, L. 2017, *Reports on Progress in Physics*, 80, 096901, doi: 10.1088/1361-6633/aa67bb
- Balbus, S. A., & Hawley, J. F. 1998, *Reviews of Modern Physics*, 70, 1, doi: 10.1103/RevModPhys.70.1
- Barnes, J., & Kasen, D. 2013, *Astrophys. J.*, 775, 18, doi: 10.1088/0004-637X/775/1/18
- Barnes, J., Kasen, D., Wu, M.-R., & Martínez-Pinedo, G. 2016, *Astrophys. J.*, 829, 110, doi: 10.3847/0004-637X/829/2/110
- Barnes, J., Zhu, Y. L., Lund, K. A., et al. 2021, *Astrophys. J.*, 918, 44, doi: 10.3847/1538-4357/ac0aec
- Baumgarte, T., & Shapiro, S. 2010, *Numerical Relativity: Solving Einstein's Equations on the Computer* (Cambridge University Press). <https://books.google.de/books?id=dxU10EinvRUC>
- Baumgarte, T. W., Shapiro, S. L., & Shibata, M. 2000, *Astrophys. J. Lett.*, 528, L29, doi: 10.1086/312425
- Bauswein, A., Ardevol Pulpillo, R., Janka, H. T., & Goriely, S. 2014, *Astrophys. J. Lett.*, 795, L9, doi: 10.1088/2041-8205/795/1/L9
- Bauswein, A., Baumgarte, T. W., & Janka, H. T. 2013, *Phys. Rev. Lett.*, 111, 131101, doi: 10.1103/PhysRevLett.111.131101
- Bauswein, A., Blacker, S., Lioutas, G., et al. 2021, *Phys. Rev. D*, 103, 123004, doi: 10.1103/PhysRevD.103.123004
- Bauswein, A., Goriely, S., & Janka, H. T. 2013, *Astrophys. J.*, 773, 78, doi: 10.1088/0004-637X/773/1/78
- Bauswein, A., & Janka, H. T. 2012, *Phys. Rev. Lett.*, 108, 011101, doi: 10.1103/PhysRevLett.108.011101
- Bauswein, A., Janka, H. T., Hebel, K., & Schwenk, A. 2012, *Phys. Rev. D*, 86, 063001, doi: 10.1103/PhysRevD.86.063001
- Bauswein, A., Just, O., Janka, H.-T., & Stergioulas, N. 2017, *Astrophys. J. Lett.*, 850, L34, doi: 10.3847/2041-8213/aa9994
- Bauswein, A., Oechslin, R., & Janka, H. T. 2010, *Phys. Rev. D*, 81, 024012, doi: 10.1103/PhysRevD.81.024012
- Bauswein, A., & Stergioulas, N. 2015, *Phys. Rev. D*, 91, 124056, doi: 10.1103/PhysRevD.91.124056
- . 2019, *Journal of Physics G Nuclear Physics*, 46, 113002, doi: 10.1088/1361-6471/ab2b90

- Bauswein, A., Bastian, N.-U. F., Blaschke, D., et al. 2019, in American Institute of Physics Conference Series, Vol. 2127, Xiamen-CUSTIPEN Workshop on the Equation of State of Dense Neutron-Rich Matter in the Era of Gravitational Wave Astronomy, 020013, doi: 10.1063/1.5117803
- Beniamini, P., & Piran, T. 2019, *Mon. Not. Roy. Astron. Soc.*, 487, 4847, doi: 10.1093/mnras/stz1589
- Berger, E. 2014, *Annual Review of Astronomy and Astrophysics*, 52, 43, doi: 10.1146/annurev-astro-081913-035926
- Berger, E., Fong, W., & Chornock, R. 2013, *Astrophys. J. Lett.*, 774, L23, doi: 10.1088/2041-8205/774/2/L23
- Bernuzzi, S. 2020, *General Relativity and Gravitation*, 52, 108, doi: 10.1007/s10714-020-02752-5
- Bernuzzi, S., Dietrich, T., & Nagar, A. 2015, *Phys. Rev. Lett.*, 115, 091101, doi: 10.1103/PhysRevLett.115.091101
- Bethe, H. A. 1990, *Reviews of Modern Physics*, 62, 801, doi: 10.1103/RevModPhys.62.801
- Bethe, H. A., & Wilson, J. R. 1985, *Astrophys. J.*, 295, 14, doi: 10.1086/163343
- Bildsten, L., & Cutler, C. 1992, *Astrophys. J.*, 400, 175, doi: 10.1086/171983
- Bionta, R. M., Blewitt, G., Bratton, C. B., et al. 1987, *Phys. Rev. Lett.*, 58, 1494, doi: 10.1103/PhysRevLett.58.1494
- Blanchet, L. 2014, *Living Reviews in Relativity*, 17, 2, doi: 10.12942/lrr-2014-2
- Blandford, R. D., & Znajek, R. L. 1977, *Mon. Not. R. Astron. Soc.*, 179, 433, doi: 10.1093/mnras/179.3.433
- Blondin, J. M., & Mezzacappa, A. 2007, *Nature*, 445, 58, doi: 10.1038/nature05428
- Blondin, J. M., Mezzacappa, A., & DeMarino, C. 2003, *Astrophys. J.*, 584, 971, doi: 10.1086/345812
- Boccioli, L., Mathews, G. J., & O'Connor, E. P. 2021, *Astrophys. J.*, 912, 29, doi: 10.3847/1538-4357/abe767
- Boccioli, L., Mathews, G. J., Suh, I.-S., & O'Connor, E. P. 2022, *Astrophys. J.*, 926, 147, doi: 10.3847/1538-4357/ac4603
- Bollig, R., DeRocco, W., Graham, P. W., & Janka, H.-T. 2020, *Phys. Rev. Lett.*, 125, 051104, doi: 10.1103/PhysRevLett.125.051104
- Bollig, R., Janka, H. T., Lohs, A., et al. 2017, *Physical Review Letters*, 119, 242702, doi: 10.1103/PhysRevLett.119.242702
- Bollig, R., Yadav, N., Kresse, D., et al. 2021, *Astrophys. J.*, 915, 28, doi: 10.3847/1538-4357/abf82e
- Bovard, L., Martin, D., Guercilena, F., et al. 2017, *Phys. Rev. D*, 96, 124005, doi: 10.1103/PhysRevD.96.124005
- Breschi, M., Perego, A., Bernuzzi, S., et al. 2021, *Mon. Not. Roy. Astron. Soc.*, 505, 1661, doi: 10.1093/mnras/stab1287
- Bugli, M., Guilet, J., & Obergaulinger, M. 2021, *Mon. Not. R. Astron. Soc.*, 507, 443, doi: 10.1093/mnras/stab2161
- Bulla, M. 2019, *Mon. Not. Roy. Astron. Soc.*, 489, 5037, doi: 10.1093/mnras/stz2495
- Burbidge, E. M., Burbidge, G. R., Fowler, W. A., & Hoyle, F. 1957, *Reviews of Modern Physics*, 29, 547, doi: 10.1103/RevModPhys.29.547
- Burrows, A. 1990a, *Annual Review of Nuclear and Particle Science*, 40, 181, doi: 10.1146/annurev.ns.40.120190.001145
- , 2013, *Reviews of Modern Physics*, 85, 245, doi: 10.1103/RevModPhys.85.245
- Burrows, A., Hayes, J., & Fryxell, B. A. 1995, *Astrophys. J.*, 450, 830, doi: 10.1086/176188
- Burrows, A., & Lattimer, J. M. 1986, *Astrophysical J.*, 307, 178, doi: 10.1086/164405
- Burrows, A., Radice, D., Vartanyan, D., et al. 2020, *Mon. Not. R. Astron. Soc.*, 491, 2715, doi: 10.1093/mnras/stz3223
- Burrows, A., & Vartanyan, D. 2021, *Nature*, 589, 29, doi: 10.1038/s41586-020-03059-w
- Burrows, A. S. 1990b, in *Supernovae*, ed. A. G. Petschek (Springer, New York (1990)), 143–181
- Cameron, A. G. W. 1959, *Astrophys. J.*, 129, 676, doi: 10.1086/146667

- Capano, C. D., Tews, I., Brown, S. M., et al. 2020, *Nature Astronomy*, 4, 625, doi: 10.1038/s41550-020-1014-6
- Caputo, A., Raffelt, G., & Vitagliano, E. 2022, *Phys. Rev. D*, 105, 035022, doi: 10.1103/PhysRevD.105.035022
- Chatziioannou, K. 2020, *General Relativity and Gravitation*, 52, 109, doi: 10.1007/s10714-020-02754-3
- Chornock, R., Berger, E., Kasen, D., et al. 2017, *Astrophys. J. Lett.*, 848, L19, doi: 10.3847/2041-8213/aa905c
- Christie, I. M., Lalakos, A., Tchekhovskoy, A., et al. 2019, *Mon. Not. Roy. Astron. Soc.*, 490, 4811, doi: 10.1093/mnras/stz2552
- Cigan, P., Matsuura, M., Gomez, H. L., et al. 2019, *Astrophys. J.*, 886, 51, doi: 10.3847/1538-4357/ab4b46
- Cioffi, R. 2020, *General Relativity and Gravitation*, 52, 59, doi: 10.1007/s10714-020-02714-x
- Cioffi, R., & Kalinani, J. V. 2020, *Astrophys. J. Lett.*, 900, L35, doi: 10.3847/2041-8213/abb240
- Cioffi, R., Kastaun, W., Giacomazzo, B., et al. 2017, *Phys. Rev. D*, 95, 063016, doi: 10.1103/PhysRevD.95.063016
- Colgate, S. A., & White, R. H. 1966, *Astrophys. J.*, 143, 626, doi: 10.1086/148549
- Collaboration, L. S., Aasi, J., Abbott, B. P., et al. 2015, *Classical and Quantum Gravity*, 32, 074001, doi: 10.1088/0264-9381/32/7/074001
- Collins, C. E., Bauswein, A., Sim, S. A., et al. 2022, arXiv e-prints, arXiv:2209.05246. <https://arxiv.org/abs/2209.05246>
- Combi, L., & Siegel, D. 2022, arXiv e-prints, arXiv:2206.03618. <https://arxiv.org/abs/2206.03618>
- Côté, B., Fryer, C. L., Belczynski, K., et al. 2018, *Astrophys. J.*, 855, 99, doi: 10.3847/1538-4357/aaad67
- Coughlin, M. W., Dietrich, T., Margalit, B., & Metzger, B. D. 2019, *Mon. Not. Roy. Astron. Soc.*, 489, L91, doi: 10.1093/mnrasl/slz133
- Coughlin, M. W., Dietrich, T., Doctor, Z., et al. 2018, *Mon. Not. Roy. Astron. Soc.*, 480, 3871, doi: 10.1093/mnras/sty2174
- Cowan, J. J., Sneden, C., Lawler, J. E., et al. 2021, *Reviews of Modern Physics*, 93, 015002, doi: 10.1103/RevModPhys.93.015002
- Cowperthwaite, P. S., Berger, E., Villar, V. A., et al. 2017, *Astrophys. J. Lett.*, 848, L17, doi: 10.3847/2041-8213/aa8fc7
- Creighton, J., & Anderson, W. 2011, *Gravitational-Wave Physics and Astronomy: An Introduction to Theory, Experiment and Data Analysis*, Wiley Series in Cosmology (Wiley). <https://books.google.de/books?id=jLRLVaR97AUC>
- Cromartie, H. T., Fonseca, E., Ransom, S. M., et al. 2020, *Nature Astronomy*, 4, 72, doi: 10.1038/s41550-019-0880-2
- Curtis, S., Mösta, P., Wu, Z., et al. 2021, arXiv e-prints, arXiv:2112.00772. <https://arxiv.org/abs/2112.00772>
- da Silva Schneider, A., O'Connor, E., Granqvist, E., Betranhandy, A., & Couch, S. M. 2020, *Astrophys. J.*, 894, 4, doi: 10.3847/1538-4357/ab8308
- Damour, T., & Nagar, A. 2010, *Phys. Rev. D*, 81, 084016, doi: 10.1103/PhysRevD.81.084016
- Damour, T., Nagar, A., & Villain, L. 2012, *Phys. Rev. D*, 85, 123007, doi: 10.1103/PhysRevD.85.123007
- De, S., Finstad, D., Lattimer, J. M., et al. 2018, *Phys. Rev. Lett.*, 121, 091102, doi: 10.1103/PhysRevLett.121.091102
- Dean, C., Fernández, R., & Metzger, B. D. 2021, *Astrophys. J.*, 921, 161, doi: 10.3847/1538-4357/ac1f20
- Dessart, L., Ott, C. D., Burrows, A., Rosswog, S., & Livne, E. 2009, *Astrophys. J.*, 690, 1681, doi: 10.1088/0004-637X/690/2/1681

- Diehl, R., Hallowin, H., Kretschmer, K., et al. 2006, *Nature*, 439, 45, doi: 10.1038/nature04364
- Dietrich, T., Bernuzzi, S., Ujevic, M., & Tichy, W. 2017a, *Phys. Rev. D*, 95, 044045, doi: 10.1103/PhysRevD.95.044045
- Dietrich, T., Coughlin, M. W., Pang, P. T. H., et al. 2020, *Science*, 370, 1450, doi: 10.1126/science.abb4317
- Dietrich, T., Hinderer, T., & Samajdar, A. 2021, *General Relativity and Gravitation*, 53, 27, doi: 10.1007/s10714-020-02751-6
- Dietrich, T., & Ujevic, M. 2017, *Classical and Quantum Gravity*, 34, 105014, doi: 10.1088/1361-6382/aa6bb0
- Dietrich, T., Ujevic, M., Tichy, W., Bernuzzi, S., & Brüggmann, B. 2017b, *Phys. Rev. D*, 95, 024029, doi: 10.1103/PhysRevD.95.024029
- Domogatskii, G. V., & Nadezhin, D. K. 1978, *Soviet Astronomy*, 22, 297
- , 1980, *Astrophysics and Space Science*, 70, 33, doi: 10.1007/BF00641663
- Domogatsky, G. V., & Nadyozhin, D. K. 1977, *Mon. Not. R. Astron. Soc.*, 178, 33P, doi: 10.1093/mnras/178.1.33P
- Domoto, N., Tanaka, M., Kato, D., et al. 2022, *Astrophys. J.*, 939, 8, doi: 10.3847/1538-4357/ac8c36
- Domoto, N., Tanaka, M., Wanajo, S., & Kawaguchi, K. 2021, *Astrophys. J.*, 913, 26, doi: 10.3847/1538-4357/abf358
- Duez, M. D., Foucart, F., Kidder, L. E., Ott, C. D., & Teukolsky, S. A. 2010, *Classical and Quantum Gravity*, 27, 114106, doi: 10.1088/0264-9381/27/11/114106
- Duez, M. D., & Zlochower, Y. 2019, *Reports on Progress in Physics*, 82, 016902, doi: 10.1088/1361-6633/aadb16
- Duncan, R. C., Shapiro, S. L., & Wasserman, I. 1986, *Astrophys. J.*, 309, 141, doi: 10.1086/164587
- Eggenberger Andersen, O., Zha, S., da Silva Schneider, A., et al. 2021, *Astrophys. J.*, 923, 201, doi: 10.3847/1538-4357/ac294c
- Eichler, D., Livio, M., Piran, T., & Schramm, D. N. 1989, *Nature*, 340, 126, doi: 10.1038/340126a0
- Eichler, M., Arcones, A., Kelic, A., et al. 2015, *Astrophys. J.*, 808, 30, doi: 10.1088/0004-637X/808/1/30
- Etienne, Z. B., Paschalidis, V., & Shapiro, S. L. 2012, *Phys. Rev. D*, 86, 084026, doi: 10.1103/PhysRevD.86.084026
- Evans, P. A., Cenko, S. B., Kennea, J. A., et al. 2017, *Science*, 358, 1565, doi: 10.1126/science.aap9580
- Fahlman, S., & Fernández, R. 2022, *Mon. Not. Roy. Astron. Soc.*, 513, 2689, doi: 10.1093/mnras/stac948
- Farr, B., Berry, C. P. L., Farr, W. M., et al. 2016, *Astrophys. J.*, 825, 116, doi: 10.3847/0004-637X/825/2/116
- Fattoyev, F. J., Piekarewicz, J., & Horowitz, C. J. 2018, *Phys. Rev. Lett.*, 120, 172702, doi: 10.1103/PhysRevLett.120.172702
- Fernández, R., Foucart, F., Kasen, D., et al. 2017, *Classical and Quantum Gravity*, 34, 154001, doi: 10.1088/1361-6382/aa7a77
- Fernández, R., Foucart, F., & Lippuner, J. 2020, *Mon. Not. Roy. Astron. Soc.*, 497, 3221, doi: 10.1093/mnras/staa2209
- Fernández, R., Kasen, D., Metzger, B. D., & Quataert, E. 2015, *Mon. Not. Roy. Astron. Soc.*, 446, 750, doi: 10.1093/mnras/stu2112
- Fernández, R., & Metzger, B. D. 2013, *Mon. Not. Roy. Astron. Soc.*, 435, 502, doi: 10.1093/mnras/stt1312
- Fernández, R., & Metzger, B. D. 2016, *Annual Review of Nuclear and Particle Science*, 66, 23, doi: 10.1146/annurev-nucl-102115-044819
- Fernández, R., Tchekhovskoy, A., Quataert, E., Foucart, F., & Kasen, D. 2019, *Mon. Not. Roy. Astron. Soc.*, 482, 3373, doi: 10.1093/mnras/sty2932

- Fiorillo, D. F. G., Raffelt, G. G., & Vitagliano, E. 2022, arXiv e-prints, arXiv:2209.11773. <https://arxiv.org/abs/2209.11773>
- Fischer, T., Hempel, M., Sagert, I., Suwa, Y., & Schaffner-Bielich, J. 2014, *European Physical Journal A*, 50, 46, doi: 10.1140/epja/i2014-14046-5
- Fischer, T., Whitehouse, S. C., Mezzacappa, A., Thielemann, F. K., & Liebendörfer, M. 2010, *Astron. Astrophys.*, 517, A80, doi: 10.1051/0004-6361/200913106
- Fischer, T., Wu, M.-R., Wehmeyer, B., et al. 2020, *Astrophys. J.*, 894, 9, doi: 10.3847/1538-4357/ab86b0
- Fischer, T., Bastian, N.-U. F., Wu, M.-R., et al. 2018, *Nature Astronomy*, 2, 980, doi: 10.1038/s41550-018-0583-0
- Flanagan, É. É., & Hinderer, T. 2008, *Phys. Rev. D*, 77, 021502, doi: 10.1103/PhysRevD.77.021502
- Foglizzo, T., Kazeroni, R., Guilet, J., et al. 2015, *Publications of the Astronomical Society of Australia*, 32, e009, doi: 10.1017/pasa.2015.9
- Fontes, C. J., Fryer, C. L., Hungerford, A. L., Wollaeger, R. T., & Korobkin, O. 2020, *Mon. Not. Roy. Astron. Soc.*, 493, 4143, doi: 10.1093/mnras/staa485
- Foucart, F. 2022, arXiv e-prints, arXiv:2209.02538. <https://arxiv.org/abs/2209.02538>
- Foucart, F., Duez, M. D., Kidder, L. E., et al. 2018, *Phys. Rev. D*, 98, 063007, doi: 10.1103/PhysRevD.98.063007
- Foucart, F., Duez, M. D., Kidder, L. E., & Teukolsky, S. A. 2011, *Phys. Rev. D*, 83, 024005, doi: 10.1103/PhysRevD.83.024005
- Foucart, F., Mösta, P., Ramirez, T., et al. 2021, *Phys. Rev. D*, 104, 123010, doi: 10.1103/PhysRevD.104.123010
- Foucart, F., Deaton, M. B., Duez, M. D., et al. 2013, *Phys. Rev. D*, 87, 084006, doi: 10.1103/PhysRevD.87.084006
- , 2014, *Phys. Rev. D*, 90, 024026, doi: 10.1103/PhysRevD.90.024026
- Foucart, F., Haas, R., Duez, M. D., et al. 2016, *Phys. Rev. D*, 93, 044019, doi: 10.1103/PhysRevD.93.044019
- Freiburghaus, C., Rosswog, S., & Thielemann, F. K. 1999, *Astrophys. J. Lett.*, 525, L121, doi: 10.1086/312343
- Fröhlich, C., Martínez-Pinedo, G., Liebendörfer, M., et al. 2006, *Phys. Rev. Lett.*, 96, 142502, doi: 10.1103/PhysRevLett.96.142502
- Fujibayashi, S., Kiuchi, K., Nishimura, N., Sekiguchi, Y., & Shibata, M. 2018, *Astrophys. J.*, 860, 64, doi: 10.3847/1538-4357/aabafd
- Fujibayashi, S., Kiuchi, K., Wanajo, S., et al. 2022, arXiv e-prints, arXiv:2205.05557. <https://arxiv.org/abs/2205.05557>
- Fujibayashi, S., Sekiguchi, Y., Kiuchi, K., & Shibata, M. 2017, *Astrophys. J.*, 846, 114, doi: 10.3847/1538-4357/aa8039
- Fujibayashi, S., Shibata, M., Wanajo, S., et al. 2020a, *Phys. Rev. D*, 101, 083029, doi: 10.1103/PhysRevD.101.083029
- Fujibayashi, S., Wanajo, S., Kiuchi, K., et al. 2020b, *Astrophys. J.*, 901, 122, doi: 10.3847/1538-4357/abafc2
- Gillanders, J. H., Smartt, S. J., Sim, S. A., Bauswein, A., & Goriely, S. 2022, *Mon. Not. Roy. Astron. Soc.*, 515, 631, doi: 10.1093/mnras/stac1258
- Giuliani, S. A., Martínez-Pinedo, G., Wu, M.-R., & Robledo, L. M. 2020, *Phys. Rev. C*, 102, 045804, doi: 10.1103/PhysRevC.102.045804
- Glas, R., Janka, H. T., Capozzi, F., et al. 2020, *Physical Review D*, 101, 063001, doi: 10.1103/PhysRevD.101.063001
- Glas, R., Janka, H. T., Melson, T., Stockinger, G., & Just, O. 2019, *Astrophys. J.*, 881, 36, doi: 10.3847/1538-4357/ab275c
- Goldstein, A., Veres, P., Burns, E., et al. 2017, *Astrophys. J. Lett.*, 848, L14, doi: 10.3847/2041-8213/aa8f41

- Goriely, S., Bauswein, A., & Janka, H.-T. 2011, *Astrophys. J. Lett.*, 738, L32, doi: 10.1088/2041-8205/738/2/L32
- Goriely, S., Bauswein, A., Just, O., Pllumbi, E., & Janka, H. T. 2015, *Mon. Not. Roy. Astron. Soc.*, 452, 3894, doi: 10.1093/mnras/stv1526
- Goriely, S., Sida, J. L., Lemaître, J. F., et al. 2013, *Phys. Rev. Lett.*, 111, 242502, doi: 10.1103/PhysRevLett.111.242502
- Gottlieb, O., Lalakos, A., Bromberg, O., Liska, M., & Tchekhovskoy, A. 2022a, *Mon. Not. Roy. Astron. Soc.*, 510, 4962, doi: 10.1093/mnras/stab3784
- Gottlieb, O., Liska, M., Tchekhovskoy, A., et al. 2022b, *Astrophys. J. Lett.*, 933, L9, doi: 10.3847/2041-8213/ac7530
- Grossman, D., Korobkin, O., Rosswog, S., & Piran, T. 2014, *Mon. Not. Roy. Astron. Soc.*, 439, 757, doi: 10.1093/mnras/stt2503
- Haddadi, M., Duez, M. D., Foucart, F., et al. 2022, arXiv e-prints, arXiv:2208.02367. <https://arxiv.org/abs/2208.02367>
- Halevi, G., & Mösta, P. 2018, *Mon. Not. R. Astron. Soc.*, 477, 2366, doi: 10.1093/mnras/sty797
- Hayashi, K., Fujibayashi, S., Kiuchi, K., et al. 2022, *Phys. Rev. D*, 106, 023008, doi: 10.1103/PhysRevD.106.023008
- Heger, A., Fryer, C. L., Woosley, S. E., Langer, N., & Hartmann, D. H. 2003, *Astrophys. J.*, 591, 288, doi: 10.1086/375341
- Heger, A., Woosley, S. E., & Spruit, H. C. 2005, *Astrophys. J.*, 626, 350, doi: 10.1086/429868
- Hempel, M. 2015, *Physical Review C*, 91, 055807, doi: 10.1103/PhysRevC.91.055807
- Hempel, M., Fischer, T., Schaffner-Bielich, J., & Liebendörfer, M. 2012, *Astrophys. J.*, 748, 70, doi: 10.1088/0004-637X/748/1/70
- Hempel, M., & Schaffner-Bielich, J. 2010, *Nuclear Physics A*, 837, 210, doi: 10.1016/j.nuclphysa.2010.02.010
- Henkel, A., Foucart, F., Raaijmakers, G., & Nisanke, S. 2022, arXiv e-prints, arXiv:2207.07658. <https://arxiv.org/abs/2207.07658>
- Herant, M., Benz, W., Hix, W. R., Fryer, C. L., & Colgate, S. A. 1994, *Astrophys. J.*, 435, 339, doi: 10.1086/174817
- Hillebrandt, W., Nomoto, K., & Wolff, R. G. 1984, *Astronomy & Astrophysics*, 133, 175
- Hillebrandt, W., & Wolff, R. G. 1985, in *Nucleosynthesis: Challenges and New Developments*, ed. W. D. Arnett & J. W. Truran (University of Chicago Press, Chicago (1985)), 131
- Hinderer, T. 2008, *Astrophys. J.*, 677, 1216, doi: 10.1086/533487
- Hinderer, T., Lackey, B. D., Lang, R. N., & Read, J. S. 2010, *Phys. Rev. D*, 81, 123016, doi: 10.1103/PhysRevD.81.123016
- Hirata, K., Kajita, T., Koshihara, M., et al. 1987, *Phys. Rev. Lett.*, 58, 1490, doi: 10.1103/PhysRevLett.58.1490
- Hoffman, R. D., Woosley, S. E., & Qian, Y. Z. 1997, *Astrophys. J.*, 482, 951, doi: 10.1086/304181
- Holmbeck, E. M., Sprouse, T. M., Mumpower, M. R., et al. 2019, *Astrophys. J.*, 870, 23, doi: 10.3847/1538-4357/aaefef
- Horowitz, C. J. 2002, *Phys. Rev. D*, 65, 043001, doi: 10.1103/PhysRevD.65.043001
- Horowitz, C. J., & Li, G. 1999, *Phys. Rev. Lett.*, 82, 5198, doi: 10.1103/PhysRevLett.82.5198
- Horowitz, C. J., Arcones, A., Côté, B., et al. 2019, *Journal of Physics G Nuclear Physics*, 46, 083001, doi: 10.1088/1361-6471/ab0849
- Hossein Nouri, F., Duez, M. D., Foucart, F., et al. 2018, *Phys. Rev. D*, 97, 083014, doi: 10.1103/PhysRevD.97.083014
- Hotokezaka, K., Beniamini, P., & Piran, T. 2018, *International Journal of Modern Physics D*, 27, 1842005, doi: 10.1142/S0218271818420051
- Hotokezaka, K., Kiuchi, K., Kyutoku, K., et al. 2013a, *Phys. Rev. D*, 88, 044026, doi: 10.1103/PhysRevD.88.044026
- . 2013b, *Phys. Rev. D*, 87, 024001, doi: 10.1103/PhysRevD.87.024001

- Hotokezaka, K., Kyutoku, K., Okawa, H., Shibata, M., & Kiuchi, K. 2011, *Phys. Rev. D*, 83, 124008, doi: 10.1103/PhysRevD.83.124008
- Hotokezaka, K., & Nakar, E. 2020, *Astrophys. J.*, 891, 152, doi: 10.3847/1538-4357/ab6a98
- Hüdepohl, L. 2013, Phd thesis, Technische Universität München, München
- Hüdepohl, L., Müller, B., Janka, H. T., Marek, A., & Raffelt, G. G. 2010, *Phys. Rev. Lett.*, 104, 251101, doi: 10.1103/PhysRevLett.104.251101
- Huth, S., Pang, P. T. H., Tews, I., et al. 2022, *Nature*, 606, 276, doi: 10.1038/s41586-022-04750-w
- Jakobus, P., Müller, B., Heger, A., et al. 2022, arXiv e-prints, arXiv:2204.10397. <https://arxiv.org/abs/2204.10397>
- Janka, H.-T. 2012, *Annual Review of Nuclear and Particle Science*, 62, 407, doi: 10.1146/annurev-nucl-102711-094901
- . 2017, in *Handbook of Supernovae*, ed. A. W. Alsabti & P. Murdin (Springer, Cham), 1095, doi: 10.1007/978-3-319-21846-5_109
- Janka, H. T., Eberl, T., Ruffert, M., & Fryer, C. L. 1999, *Astrophys. J. Lett.*, 527, L39, doi: 10.1086/312397
- Janka, H. T., Langanke, K., Marek, A., Martínez-Pinedo, G., & Müller, B. 2007, *Physics Reports*, 442, 38, doi: 10.1016/j.physrep.2007.02.002
- Janka, H.-T., Melson, T., & Summa, A. 2016, *Annual Review of Nuclear and Particle Science*, 66, 341, doi: 10.1146/annurev-nucl-102115-044747
- Janka, H. T., & Müller, E. 1996, *Astronomy and Astrophysics*, 306, 167
- Janka, H. T., & Ruffert, M. 2002, in *Astronomical Society of the Pacific Conference Series*, Vol. 263, *Stellar Collisions, Mergers and their Consequences*, ed. M. M. Shara, 333. <https://arxiv.org/abs/astro-ph/0101357>
- Janka, H.-T., Wongwathanarat, A., & Kramer, M. 2022, *Astrophys. J.*, 926, 9, doi: 10.3847/1538-4357/ac403c
- Just, O., Abbar, S., Wu, M.-R., et al. 2022, *Phys. Rev. D*, 105, 083024, doi: 10.1103/PhysRevD.105.083024
- Just, O., Aloy, M. A., Obergaulinger, M., & Nagataki, S. 2022, arXiv e-prints, arXiv:2205.14158. <https://arxiv.org/abs/2205.14158>
- Just, O., Bauswein, A., Ardevol Pulpillo, R., Goriely, S., & Janka, H. T. 2015, *Mon. Not. R. Astron. Soc.*, 448, 541, doi: 10.1093/mnras/stv009
- Just, O., Goriely, S., Janka, H. T., Nagataki, S., & Bauswein, A. 2022a, *Mon. Not. Roy. Astron. Soc.*, 509, 1377, doi: 10.1093/mnras/stab2861
- Just, O., Kullmann, I., Goriely, S., et al. 2022b, *Mon. Not. Roy. Astron. Soc.*, 510, 2820, doi: 10.1093/mnras/stab3327
- Kasen, D., Badnell, N. R., & Barnes, J. 2013, *Astrophys. J.*, 774, 25, doi: 10.1088/0004-637X/774/1/25
- Kasen, D., Fernández, R., & Metzger, B. D. 2015, *Mon. Not. Roy. Astron. Soc.*, 450, 1777, doi: 10.1093/mnras/stv721
- Kasen, D., Metzger, B., Barnes, J., Quataert, E., & Ramirez-Ruiz, E. 2017, *Nature*, 551, 80, doi: 10.1038/nature24453
- Kasliwal, M. M., Nakar, E., Singer, L. P., et al. 2017, *Science*, 358, 1559, doi: 10.1126/science.aap9455
- Kastaun, W., Ciolfi, R., & Giacomazzo, B. 2016, *Phys. Rev. D*, 94, 044060, doi: 10.1103/PhysRevD.94.044060
- Katsuda, S., Morii, M., Janka, H.-T., et al. 2018, *Astrophys. J.*, 856, 18, doi: 10.3847/1538-4357/aab092
- Kawaguchi, K., Fujibayashi, S., Shibata, M., Tanaka, M., & Wanajo, S. 2021, *Astrophys. J.*, 913, 100, doi: 10.3847/1538-4357/abf3bc
- Kawaguchi, K., Shibata, M., & Tanaka, M. 2018, *Astrophys. J. Lett.*, 865, L21, doi: 10.3847/2041-8213/aade02
- Keil, W., & Janka, H. T. 1995, *Astron. Astrophys.*, 296, 145

- Kilpatrick, C. D., Foley, R. J., Kasen, D., et al. 2017, *Science*, 358, 1583, doi: 10.1126/science.aag0073
- Kirsebom, O. S., Jones, S., Strömberg, D. F., et al. 2019, *Phys. Rev. Lett.*, 123, 262701, doi: 10.1103/PhysRevLett.123.262701
- Kiuchi, K., Kyutoku, K., Sekiguchi, Y., & Shibata, M. 2018, *Phys. Rev. D*, 97, 124039, doi: 10.1103/PhysRevD.97.124039
- Kiuchi, K., Kyutoku, K., Shibata, M., & Taniguchi, K. 2019, *Astrophys. J. Lett.*, 876, L31, doi: 10.3847/2041-8213/ab1e45
- Klion, H., Tchekhovskoy, A., Kasen, D., et al. 2022, *Mon. Not. Roy. Astron. Soc.*, 510, 2968, doi: 10.1093/mnras/stab3583
- Kochanek, C. S. 1992, *Astrophys. J.*, 398, 234, doi: 10.1086/171851
- Köppel, S., Bovard, L., & Rezzolla, L. 2019, *Astrophys. J. Lett.*, 872, L16, doi: 10.3847/2041-8213/ab0210
- Korobkin, O., Rosswog, S., Arcones, A., & Winteler, C. 2012, *Mon. Not. Roy. Astron. Soc.*, 426, 1940, doi: 10.1111/j.1365-2966.2012.21859.x
- Kozyreva, A., Baklanov, P., Jones, S., Stockinger, G., & Janka, H.-T. 2021, *Mon. Not. R. Astron. Soc.*, 503, 797, doi: 10.1093/mnras/stab350
- Kozyreva, A., Janka, H.-T., Kresse, D., Taubenberger, S., & Baklanov, P. 2022, *Mon. Not. R. Astron. Soc.*, 514, 4173, doi: 10.1093/mnras/stac1518
- Krüger, C. J., & Foucart, F. 2020, *Phys. Rev. D*, 101, 103002, doi: 10.1103/PhysRevD.101.103002
- Kulkarni, S. R. 2005, arXiv e-prints, astro. <https://arxiv.org/abs/astro-ph/0510256>
- Kullmann, I., Goriely, S., Just, O., et al. 2022a, *Mon. Not. Roy. Astron. Soc.*, 510, 2804, doi: 10.1093/mnras/stab3393
- Kullmann, I., Goriely, S., Just, O., Bauswein, A., & Janka, H. T. 2022b, arXiv e-prints, arXiv:2207.07421. <https://arxiv.org/abs/2207.07421>
- Kuroda, T., Fischer, T., Takiwaki, T., & Kotake, K. 2022, *Astrophys. J.*, 924, 38, doi: 10.3847/1538-4357/ac31a8
- Kyutoku, K., Ioka, K., Okawa, H., Shibata, M., & Taniguchi, K. 2015, *Phys. Rev. D*, 92, 044028, doi: 10.1103/PhysRevD.92.044028
- Kyutoku, K., Okawa, H., Shibata, M., & Taniguchi, K. 2011, *Phys. Rev. D*, 84, 064018, doi: 10.1103/PhysRevD.84.064018
- Kyutoku, K., Shibata, M., & Taniguchi, K. 2021, *Living Reviews in Relativity*, 24, 5, doi: 10.1007/s41114-021-00033-4
- Lai, D. 1994, *Mon. Not. Roy. Astron. Soc.*, 270, 611, doi: 10.1093/mnras/270.3.611
- Langanke, K., Martínez-Pinedo, G., Sampaio, J. M., et al. 2003, *Phys. Rev. Lett.*, 90, 241102, doi: 10.1103/PhysRevLett.90.241102
- Lattimer, J. M. 2012, *Annual Review of Nuclear and Particle Science*, 62, 485, doi: 10.1146/annurev-nucl-102711-095018
- Lattimer, J. M., & Prakash, M. 2001, *Astrophys. J.*, 550, 426, doi: 10.1086/319702
- Lattimer, J. M., & Schramm, D. N. 1974, *Astrophys. J. Lett.*, 192, L145, doi: 10.1086/181612
- , 1976, *Astrophys. J.*, 210, 549, doi: 10.1086/154860
- Lattimer, J. M., & Swesty, D. F. 1991, *Nuclear Physics A*, 535, 331, doi: 10.1016/0375-9474(91)90452-C
- Lee, W. H., Ramirez-Ruiz, E., & López-Cámara, D. 2009, *Astrophys. J. Lett.*, 699, L93, doi: 10.1088/0004-637X/699/2/L93
- Lee, W. H., Ramirez-Ruiz, E., & Page, D. 2005, *Astrophys. J.*, 632, 421, doi: 10.1086/432373
- Lehner, L., Liebling, S. L., Palenzuela, C., et al. 2016, *Classical and Quantum Gravity*, 33, 184002, doi: 10.1088/0264-9381/33/18/184002
- Lemaître, J. F., Goriely, S., Bauswein, A., & Janka, H. T. 2021, *Phys. Rev. C*, 103, 025806, doi: 10.1103/PhysRevC.103.025806
- Li, L.-X., & Paczyński, B. 1998, *Astrophys. J. Lett.*, 507, L59, doi: 10.1086/311680

- Li, S. W., Roberts, L. F., & Beacom, J. F. 2021, *Phys. Rev. D*, 103, 023016, doi: 10.1103/PhysRevD.103.023016
- Li, X., & Siegel, D. M. 2021, *Phys. Rev. Lett.*, 126, 251101, doi: 10.1103/PhysRevLett.126.251101
- Lippuner, J., Fernández, R., Roberts, L. F., et al. 2017, *Mon. Not. Roy. Astron. Soc.*, 472, 904, doi: 10.1093/mnras/stx1987
- Lippuner, J., & Roberts, L. F. 2015, *Astrophys. J.*, 815, 82, doi: 10.1088/0004-637X/815/2/82
- MacFadyen, A. I., & Woosley, S. E. 1999, *Astrophys. J.*, 524, 262, doi: 10.1086/307790
- MacFadyen, A. I., Woosley, S. E., & Heger, A. 2001, *Astrophys. J.*, 550, 410, doi: 10.1086/319698
- Maggiore, M. 2008, *Gravitational Waves: Volume 1: Theory and Experiments*, Gravitational Waves (OUP Oxford). <https://books.google.de/books?id=AqVpQgAACAAJ>
- Malkus, A., McLaughlin, G. C., & Surman, R. 2016, *Phys. Rev. D*, 93, 045021, doi: 10.1103/PhysRevD.93.045021
- Marek, A., Janka, H. T., & Müller, E. 2009, *Astron. Astrophysics*, 496, 475, doi: 10.1051/0004-6361/200810883
- Margalit, B., & Metzger, B. D. 2017, *Astrophys. J. Lett.*, 850, L19, doi: 10.3847/2041-8213/aa991c
- Margalit, B., & Metzger, B. D. 2019, *Astrophys. J. Lett.*, 880, L15, doi: 10.3847/2041-8213/ab2ae2
- Martí, J. M., & Müller, E. 2015, *Living Reviews in Computational Astrophysics*, 1, 3, doi: 10.1007/lrca-2015-3
- Martin, D., Arcones, A., Nazarewicz, W., & Olsen, E. 2016, *Phys. Rev. Lett.*, 116, 121101, doi: 10.1103/PhysRevLett.116.121101
- Martin, D., Perego, A., Arcones, A., et al. 2015, *Astrophys. J.*, 813, 2, doi: 10.1088/0004-637X/813/1/2
- Martin, D., Perego, A., Kastaun, W., & Arcones, A. 2018, *Classical and Quantum Gravity*, 35, 034001, doi: 10.1088/1361-6382/aa9f5a
- Martínez-Pinedo, G., Fischer, T., & Huther, L. 2014, *Journal of Physics G Nuclear Physics*, 41, 044008, doi: 10.1088/0954-3899/41/4/044008
- Martínez-Pinedo, G., Fischer, T., Lohs, A., & Huther, L. 2012, *Physical Review Letters*, 109, 251104, doi: 10.1103/PhysRevLett.109.251104
- Melson, T., Janka, H.-T., Bollig, R., et al. 2015, *Astrophys. J. Lett.*, 808, L42, doi: 10.1088/2041-8205/808/2/L42
- Mendoza-Temis, J. d. J., Wu, M.-R., Langanke, K., et al. 2015, *Phys. Rev. C*, 92, 055805, doi: 10.1103/PhysRevC.92.055805
- Metzger, B. D. 2019, *Living Reviews in Relativity*, 23, 1, doi: 10.1007/s41114-019-0024-0
- Metzger, B. D., Bauswein, A., Gorieli, S., & Kasen, D. 2015, *Mon. Not. Roy. Astron. Soc.*, 446, 1115, doi: 10.1093/mnras/stu2225
- Metzger, B. D., & Berger, E. 2012, *Astrophys. J.*, 746, 48, doi: 10.1088/0004-637X/746/1/48
- Metzger, B. D., & Fernández, R. 2014, *Mon. Not. Roy. Astron. Soc.*, 441, 3444, doi: 10.1093/mnras/stu802
- Metzger, B. D., Piro, A. L., & Quataert, E. 2008, *Mon. Not. Roy. Astron. Soc.*, 390, 781, doi: 10.1111/j.1365-2966.2008.13789.x
- . 2009, *Mon. Not. Roy. Astron. Soc.*, 396, 304, doi: 10.1111/j.1365-2966.2008.14380.x
- Metzger, B. D., Thompson, T. A., & Quataert, E. 2018, *Astrophys. J.*, 856, 101, doi: 10.3847/1538-4357/aab095
- Metzger, B. D., Martínez-Pinedo, G., Darbha, S., et al. 2010, *Mon. Not. Roy. Astron. Soc.*, 406, 2650, doi: 10.1111/j.1365-2966.2010.16864.x

- Miller, J. M., Ryan, B. R., Dolence, J. C., et al. 2019, *Phys. Rev. D*, 100, 023008, doi: 10.1103/PhysRevD.100.023008
- Miller, M. C., Lamb, F. K., Dittmann, A. J., et al. 2019, *Astrophys. J. Lett.*, 887, L24, doi: 10.3847/2041-8213/ab50c5
- Mirizzi, A., Tamborra, I., Janka, H. T., et al. 2016, *Nuovo Cimento Rivista Serie*, 39, 1, doi: 10.1393/ncr/i2016-10120-8
- Most, E. R., Papenfort, L. J., Tootle, S. D., & Rezzolla, L. 2021, *Mon. Not. Roy. Astron. Soc.*, 506, 3511, doi: 10.1093/mnras/stab1824
- Most, E. R., & Raithel, C. A. 2021, *Physical Review D*, 104, 124012, doi: 10.1103/PhysRevD.104.124012
- Most, E. R., Weih, L. R., Rezzolla, L., & Schaffner-Bielich, J. 2018, *Phys. Rev. Lett.*, 120, 261103, doi: 10.1103/PhysRevLett.120.261103
- Mösta, P., Radice, D., Haas, R., Schnetter, E., & Bernuzzi, S. 2020, *Astrophys. J. Lett.*, 901, L37, doi: 10.3847/2041-8213/abb6ef
- Mösta, P., Roberts, L. F., Halevi, G., et al. 2018, *Astrophys. J.*, 864, 171, doi: 10.3847/1538-4357/aad6ec
- Müller, B. 2016, *Publications of the Astronomical Society of Australia*, 33, e048, doi: 10.1017/pasa.2016.40
- . 2019, *Mon. Not. R. Astron. Soc.*, 487, 5304, doi: 10.1093/mnras/stz1594
- . 2020, *Living Reviews in Computational Astrophysics*, 6, 3, doi: 10.1007/s41115-020-0008-5
- Müller, B., & Janka, H. T. 2015, *Mon. Not. R. Astron. Soc.*, 448, 2141, doi: 10.1093/mnras/stv101
- Müller, B., Melson, T., Heger, A., & Janka, H.-T. 2017, *Mon. Not. R. Astron. Soc.*, 472, 491, doi: 10.1093/mnras/stx1962
- Mumpower, M. R., Kawano, T., Sprouse, T. M., et al. 2018, *Astrophys. J.*, 869, 14, doi: 10.3847/1538-4357/aaeaca
- Mumpower, M. R., Surman, R., Fang, D. L., et al. 2015, *Phys. Rev. C*, 92, 035807, doi: 10.1103/PhysRevC.92.035807
- Mumpower, M. R., Surman, R., McLaughlin, G. C., & Aprahamian, A. 2016, *Progress in Particle and Nuclear Physics*, 86, 86, doi: 10.1016/j.ppnp.2015.09.001
- Murguia-Berthier, A., Noble, S. C., Roberts, L. F., et al. 2021, *Astrophys. J.*, 919, 95, doi: 10.3847/1538-4357/ac1119
- Murphy, J. W., Dolence, J. C., & Burrows, A. 2013, *Astrophys. J.*, 771, 52, doi: 10.1088/0004-637X/771/1/52
- Nakar, E. 2007, *Physics Reports*, 442, 166, doi: 10.1016/j.physrep.2007.02.005
- . 2020, *Physics Reports*, 886, 1, doi: 10.1016/j.physrep.2020.08.008
- Nakar, E., & Piran, T. 2011, *Nature*, 478, 82, doi: 10.1038/nature10365
- Nakazato, K., & Suzuki, H. 2019, *Astrophys. J.*, 878, 25, doi: 10.3847/1538-4357/ab1d4b
- . 2020, *Astrophys. J.*, 891, 156, doi: 10.3847/1538-4357/ab7456
- Nativi, L., Bulla, M., Rosswog, S., et al. 2021, *Mon. Not. Roy. Astron. Soc.*, 500, 1772, doi: 10.1093/mnras/staa3337
- Nedora, V., Bernuzzi, S., Radice, D., et al. 2019, *Astrophys. J. Lett.*, 886, L30, doi: 10.3847/2041-8213/ab5794
- . 2021, *Astrophys. J.*, 906, 98, doi: 10.3847/1538-4357/abc9be
- Nedora, V., Schianchi, F., Bernuzzi, S., et al. 2022, *Classical and Quantum Gravity*, 39, 015008, doi: 10.1088/1361-6382/ac35a8
- Neuweiler, A., Dietrich, T., Bulla, M., et al. 2022, *arXiv e-prints*, arXiv:2208.13460. <https://arxiv.org/abs/2208.13460>
- Nicholl, M., Berger, E., Kasen, D., et al. 2017, *Astrophys. J. Lett.*, 848, L18, doi: 10.3847/2041-8213/aa9029
- Nikas, S., Martinez Pinedo, G., Sieverding, A., & Reiter, M. P. 2020, in *Journal of Physics Conference Series*, Vol. 1667, *Journal of Physics Conference Series*, 012030, doi: 10.1088/1742-6596/1667/1/012030

- Nishimura, N., Takiwaki, T., & Thielemann, F.-K. 2015, *Astrophys. J.*, 810, 109, doi: 10.1088/0004-637X/810/2/109
- Obergaulinger, M., & Aloy, M. Á. 2022, *Mon. Not. R. Astron. Soc.*, 512, 2489, doi: 10.1093/mnras/stac613
- O'Connor, E., & Ott, C. D. 2011, *Astrophys. J.*, 730, 70, doi: 10.1088/0004-637X/730/2/70
- . 2013, *Astrophys. J.*, 762, 126, doi: 10.1088/0004-637X/762/2/126
- O'Connor, E. P., & Couch, S. M. 2018, *Astrophys. J.*, 865, 81, doi: 10.3847/1538-4357/aadcf7
- Oechslin, R., & Janka, H. T. 2006, *Mon. Not. Roy. Astron. Soc.*, 368, 1489, doi: 10.1111/j.1365-2966.2006.10238.x
- Oechslin, R., & Janka, H. T. 2007, *Phys. Rev. Lett.*, 99, 121102, doi: 10.1103/PhysRevLett.99.121102
- Oechslin, R., Janka, H. T., & Marek, A. 2007, *Astron. Astrophys.*, 467, 395, doi: 10.1051/0004-6361:20066682
- Oertel, M., Hempel, M., Klähn, T., & Typel, S. 2017, *Reviews of Modern Physics*, 89, 015007, doi: 10.1103/RevModPhys.89.015007
- Otsuki, K., Tagoshi, H., Kajino, T., & Wanajo, S.-y. 2000, *Astrophys. J.*, 533, 424, doi: 10.1086/308632
- Page, D., Beznogov, M. V., Garibay, I., et al. 2020, *Astrophys. J.*, 898, 125, doi: 10.3847/1538-4357/ab93c2
- Palenzuela, C., Liebling, S. L., Neilsen, D., et al. 2015, *Phys. Rev. D*, 92, 044045, doi: 10.1103/PhysRevD.92.044045
- Papenfort, L. J., Gold, R., & Rezzolla, L. 2018, *Phys. Rev. D*, 98, 104028, doi: 10.1103/PhysRevD.98.104028
- Pascal, A., Novak, J., & Oertel, M. 2022, *Mon. Not. R. Astron. Soc.*, 511, 356, doi: 10.1093/mnras/stac016
- Paschalidis, V., East, W. E., Pretorius, F., & Shapiro, S. L. 2015, *Phys. Rev. D*, 92, 121502, doi: 10.1103/PhysRevD.92.121502
- Paschalidis, V., & Stergioulas, N. 2017, *Living Reviews in Relativity*, 20, 7, doi: 10.1007/s41114-017-0008-x
- Perego, A., Radice, D., & Bernuzzi, S. 2017, *Astrophys. J. Lett.*, 850, L37, doi: 10.3847/2041-8213/aa9ab9
- Perego, A., Rosswog, S., Cabezón, R. M., et al. 2014, *Mon. Not. Roy. Astron. Soc.*, 443, 3134, doi: 10.1093/mnras/stu1352
- Perego, A., Thielemann, F. K., & Cescutti, G. 2020, *r-Process Nucleosynthesis from Compact Binary Mergers* (Singapore: Springer Singapore), 1–56, doi: 10.1007/978-981-15-4702-7_13-1
- Perego, A., Vescovi, D., Fiore, A., et al. 2022, *Astrophys. J.*, 925, 22, doi: 10.3847/1538-4357/ac3751
- Pian, E., D'Avanzo, P., Benetti, S., et al. 2017, *Nature*, 551, 67, doi: 10.1038/nature24298
- Piran, T., Nakar, E., & Rosswog, S. 2013, *Mon. Not. Roy. Astron. Soc.*, 430, 2121, doi: 10.1093/mnras/stt037
- Pitlik, T., Tamborra, I., & Petropoulou, M. 2021, *Journal of Cosmology and Astroparticle Physics*, 2021, 034, doi: 10.1088/1475-7516/2021/05/034
- Pons, J. A., Reddy, S., Prakash, M., Lattimer, J. M., & Miralles, J. A. 1999, *Astrophys. J.*, 513, 780, doi: 10.1086/306889
- Pons, J. A., Steiner, A. W., Prakash, M., & Lattimer, J. M. 2001, *Phys. Rev. Lett.*, 86, 5223, doi: 10.1103/PhysRevLett.86.5223
- Powell, J., & Müller, B. 2019, *Mon. Not. R. Astron. Soc.*, 487, 1178, doi: 10.1093/mnras/stz1304
- Powell, J., Müller, B., & Heger, A. 2021, *Mon. Not. R. Astron. Soc.*, 503, 2108, doi: 10.1093/mnras/stab614

- Prakash, A., Radice, D., Logoteta, D., et al. 2021, *Phys. Rev. D*, 104, 083029, doi: 10.1103/PhysRevD.104.083029
- Pruet, J., Hoffman, R. D., Woosley, S. E., Janka, H. T., & Buras, R. 2006, *Astrophys. J.*, 644, 1028, doi: 10.1086/503891
- Qian, Y. Z., & Woosley, S. E. 1996, *Astrophys. J.*, 471, 331, doi: 10.1086/177973
- Raaijmakers, G., Greif, S. K., Hebeler, K., et al. 2021, *Astrophys. J. Lett.*, 918, L29, doi: 10.3847/2041-8213/ac089a
- Radice, D., Bernuzzi, S., & Perego, A. 2020, *Annual Review of Nuclear and Particle Science*, 70, 95, doi: 10.1146/annurev-nucl-013120-114541
- Radice, D., & Dai, L. 2019, *European Physical Journal A*, 55, 50, doi: 10.1140/epja/i2019-12716-4
- Radice, D., Galeazzi, F., Lippuner, J., et al. 2016, *Mon. Not. Roy. Astron. Soc.*, 460, 3255, doi: 10.1093/mnras/stw1227
- Radice, D., Perego, A., Hotokezaka, K., et al. 2018, *Astrophys. J. Lett.*, 869, L35, doi: 10.3847/2041-8213/aaf053
- Radice, D., Perego, A., Hotokezaka, K., et al. 2018, *Astrophys. J.*, 869, 130, doi: 10.3847/1538-4357/aaf054
- Radice, D., Perego, A., Zappa, F., & Bernuzzi, S. 2018, *Astrophys. J. Lett.*, 852, L29, doi: 10.3847/2041-8213/aaa402
- Rahman, N., Janka, H. T., Stockinger, G., & Woosley, S. E. 2022, *Mon. Not. R. Astron. Soc.*, 512, 4503, doi: 10.1093/mnras/stac758
- Reed, B., & Horowitz, C. J. 2020, *Physical Review D*, 102, 103011, doi: 10.1103/PhysRevD.102.103011
- Reichert, M., Obergaulinger, M., Aloy, M.-A., et al. 2022, arXiv e-prints, arXiv:2206.11914, <https://arxiv.org/abs/2206.11914>
- Rezzolla, L., Most, E. R., & Weih, L. R. 2018, *Astrophys. J. Lett.*, 852, L25, doi: 10.3847/2041-8213/aaa401
- Rezzolla, L., & Takami, K. 2016, *Phys. Rev. D*, 93, 124051, doi: 10.1103/PhysRevD.93.124051
- Rezzolla, L., & Zanotti, O. 2013, *Relativistic Hydrodynamics*, EBSCO ebook academic collection (OUP Oxford). <https://books.google.de/books?id=KU2oAAAAQBAJ>
- Richers, S., Willcox, D. E., Ford, N. M., & Myers, A. 2021, *Phys. Rev. D*, 103, 083013, doi: 10.1103/PhysRevD.103.083013
- Riley, T. E., Watts, A. L., Bogdanov, S., et al. 2019, *Astrophys. J. Lett.*, 887, L21, doi: 10.3847/2041-8213/ab481c
- Riley, T. E., Watts, A. L., Ray, P. S., et al. 2021, *Astrophys. J. Lett.*, 918, L27, doi: 10.3847/2041-8213/ac0a81
- Roberts, L. F. 2012, *Astrophys. J.*, 755, 126, doi: 10.1088/0004-637X/755/2/126
- Roberts, L. F., Kasen, D., Lee, W. H., & Ramirez-Ruiz, E. 2011, *Astrophys. J. Lett.*, 736, L21, doi: 10.1088/2041-8205/736/1/L21
- Roberts, L. F., & Reddy, S. 2017, in *Handbook of Supernovae*, ed. A. W. Alsabti & P. Murdin (Springer, Cham), 1605, doi: 10.1007/978-3-319-21846-5_5
- Roberts, L. F., Reddy, S., & Shen, G. 2012a, *Physical Review C*, 86, 065803, doi: 10.1103/PhysRevC.86.065803
- Roberts, L. F., Shen, G., Cirigliano, V., et al. 2012b, *Phys. Rev. Lett.*, 108, 061103, doi: 10.1103/PhysRevLett.108.061103
- Roberts, L. F., Woosley, S. E., & Hoffman, R. D. 2010, *Astrophys. J.*, 722, 954, doi: 10.1088/0004-637X/722/1/954
- Romani, R. W., Kandel, D., Filippenko, A. V., Brink, T. G., & Zheng, W. 2021, *Astrophys. J. Lett.*, 908, L46, doi: 10.3847/2041-8213/abe2b4
- . 2022, arXiv e-prints, arXiv:2207.05124. <https://arxiv.org/abs/2207.05124>
- Rosswog, S. 2005, *Astrophys. J.*, 634, 1202, doi: 10.1086/497062
- . 2015, *Living Reviews in Computational Astrophysics*, 1, 1, doi: 10.1007/lrca-2015-1

- Rosswog, S., Davies, M. B., Thielemann, F. K., & Piran, T. 2000, *Astron. Astrophys.*, 360, 171. <https://arxiv.org/abs/astro-ph/0005550>
- Rosswog, S., & Korobkin, O. 2022, arXiv e-prints, arXiv:2208.14026. <https://arxiv.org/abs/2208.14026>
- Rosswog, S., Korobkin, O., Arcones, A., Thielemann, F. K., & Piran, T. 2014, *Mon. Not. Roy. Astron. Soc.*, 439, 744, doi: 10.1093/mnras/stt2502
- Rosswog, S., Liebendörfer, M., Thielemann, F. K., et al. 1999, *Astron. Astrophys.*, 341, 499. <https://arxiv.org/abs/astro-ph/9811367>
- Rosswog, S., Sollerman, J., Feindt, U., et al. 2018, *Astron. Astrophys.*, 615, A132, doi: 10.1051/0004-6361/201732117
- Ruffert, M., & Janka, H. T. 1999, *Astron. Astrophys.*, 344, 573. <https://arxiv.org/abs/astro-ph/9809280>
- . 2001, *Astron. Astrophys.*, 380, 544, doi: 10.1051/0004-6361:20011453
- Ruffert, M., Janka, H. T., Takahashi, K., & Schaefer, G. 1997, *Astron. Astrophys.*, 319, 122. <https://arxiv.org/abs/astro-ph/9606181>
- Ruiz, M., Shapiro, S. L., & Tsokaros, A. 2018, *Phys. Rev. D*, 97, 021501, doi: 10.1103/PhysRevD.97.021501
- Sagert, I., Fischer, T., Hempel, M., et al. 2009, *Phys. Rev. Lett.*, 102, 081101, doi: 10.1103/PhysRevLett.102.081101
- Sana, H., de Mink, S. E., de Koter, A., et al. 2012, *Science*, 337, 444, doi: 10.1126/science.1223344
- Sandoval, M. A., Hix, W. R., Messer, O. E. B., Lentz, E. J., & Harris, J. A. 2021, *Astrophys. J.*, 921, 113, doi: 10.3847/1538-4357/ac1d49
- Sathyaprakash, B. S., & Schutz, B. F. 2009, *Living Reviews in Relativity*, 12, 2, doi: 10.12942/lrr-2009-2
- Savchenko, V., Ferrigno, C., Kuulkers, E., et al. 2017, *Astrophys. J. Lett.*, 848, L15, doi: 10.3847/2041-8213/aa8f94
- Schneider, A. S., Constantinou, C., Muccioli, B., & Prakash, M. 2019a, *Physical Review C*, 100, 025803, doi: 10.1103/PhysRevC.100.025803
- Schneider, A. S., Roberts, L. F., Ott, C. D., & O'Connor, E. 2019b, *Physical Review C*, 100, 055802, doi: 10.1103/PhysRevC.100.055802
- Sekiguchi, Y., Kiuchi, K., Kyutoku, K., & Shibata, M. 2011, *Phys. Rev. Lett.*, 107, 051102, doi: 10.1103/PhysRevLett.107.051102
- . 2015, *Phys. Rev. D*, 91, 064059, doi: 10.1103/PhysRevD.91.064059
- Sekiguchi, Y., Kiuchi, K., Kyutoku, K., Shibata, M., & Taniguchi, K. 2016, *Phys. Rev. D*, 93, 124046, doi: 10.1103/PhysRevD.93.124046
- Shappee, B. J., Simon, J. D., Drout, M. R., et al. 2017, *Science*, 358, 1574, doi: 10.1126/science.aag0186
- Shen, H., Toki, H., Oyamatsu, K., & Sumiyoshi, K. 1998, *Nuclear Physics A*, 637, 435, doi: 10.1016/S0375-9474(98)00236-X
- . 2011, *Astrophys. J. Suppl.*, 197, 20, doi: 10.1088/0067-0049/197/2/20
- Shibata, M. 2015, *Numerical Relativity, 100 years of general relativity* (World Scientific Publishing Company Pte Limited). <https://books.google.de/books?id=OyUjswEACAAJ>
- Shibata, M., Fujibayashi, S., Hotokezaka, K., et al. 2017, *Phys. Rev. D*, 96, 123012, doi: 10.1103/PhysRevD.96.123012
- Shibata, M., & Hotokezaka, K. 2019, *Annual Review of Nuclear and Particle Science*, 69, 41, doi: 10.1146/annurev-nucl-101918-023625
- Shibata, M., & Taniguchi, K. 2006, *Phys. Rev. D*, 73, 064027, doi: 10.1103/PhysRevD.73.064027
- . 2008, *Phys. Rev. D*, 77, 084015, doi: 10.1103/PhysRevD.77.084015
- Shibata, M., Zhou, E., Kiuchi, K., & Fujibayashi, S. 2019, *Phys. Rev. D*, 100, 023015, doi: 10.1103/PhysRevD.100.023015
- Siegel, D. M. 2019, *European Physical Journal A*, 55, 203, doi: 10.1140/epja/i2019-12888-9

- Siegel, D. M. 2022, *Nature Reviews Physics*, 4, 306, doi: 10.1038/s42254-022-00439-1
- Siegel, D. M., Barnes, J., & Metzger, B. D. 2019, *Nature*, 569, 241, doi: 10.1038/s41586-019-1136-0
- Siegel, D. M., Ciolfi, R., & Rezzolla, L. 2014, *Astrophys. J. Lett.*, 785, L6, doi: 10.1088/2041-8205/785/1/L6
- Siegel, D. M., & Metzger, B. D. 2018, *Astrophys. J.*, 858, 52, doi: 10.3847/1538-4357/aabaec
- Sieverding, A., Langanke, K., Martínez-Pinedo, G., et al. 2019, *Astrophys. J.*, 876, 151, doi: 10.3847/1538-4357/ab17e2
- Sieverding, A., Martínez-Pinedo, G., Huther, L., Langanke, K., & Heger, A. 2018, *Astrophys. J.*, 865, 143, doi: 10.3847/1538-4357/aadd48
- Smartt, S. J., Chen, T. W., Jerkstrand, A., et al. 2017, *Nature*, 551, 75, doi: 10.1038/nature24303
- Snedden, C., Cowan, J. J., & Gallino, R. 2008, *Annual Review of Astronomy and Astrophysics*, 46, 241, doi: 10.1146/annurev.astro.46.060407.145207
- Soares-Santos, M., Holz, D. E., Annis, J., et al. 2017, *Astrophys. J. Lett.*, 848, L16, doi: 10.3847/2041-8213/aa9059
- Steiner, A. W., Hempel, M., & Fischer, T. 2013, *Astrophys. J.*, 774, 17, doi: 10.1088/0004-637X/774/1/17
- Steiner, A. W., Lattimer, J. M., & Brown, E. F. 2010, *Astrophys. J.*, 722, 33, doi: 10.1088/0004-637X/722/1/33
- Stergioulas, N., Bauswein, A., Zagkouris, K., & Janka, H.-T. 2011, *Mon. Not. R. Astron. Soc.*, 418, 427, doi: 10.1111/j.1365-2966.2011.19493.x
- Stockinger, G., Janka, H. T., Kresse, D., et al. 2020, *Mon. Not. R. Astron. Soc.*, 496, 2039, doi: 10.1093/mnras/staa1691
- Stovall, K., Freire, P. C. C., Chatterjee, S., et al. 2018, *Astrophys. J. Lett.*, 854, L22, doi: 10.3847/2041-8213/aaad06
- Sumiyoshi, K., Nakazato, K., Suzuki, H., Hu, J., & Shen, H. 2019, *Astrophys. J.*, 887, 110, doi: 10.3847/1538-4357/ab5443
- Surman, R., McLaughlin, G. C., Ruffert, M., Janka, H. T., & Hix, W. R. 2008, *Astrophys. J. Lett.*, 679, L117, doi: 10.1086/589507
- Suwa, Y., Takiwaki, T., Kotake, K., et al. 2013, *Astrophys. J.*, 764, 99, doi: 10.1088/0004-637X/764/1/99
- Suzuki, T., Zha, S., Leung, S.-C., & Nomoto, K. 2019, *Astrophys. J.*, 881, 64, doi: 10.3847/1538-4357/ab2b93
- Symbalisty, E., & Schramm, D. N. 1982, *Astrophysical Letters*, 22, 143. <https://ui.adsabs.harvard.edu/abs/1982ApL...22..143S>
- Takahashi, K., Witt, J., & Janka, H. T. 1994, *Astron. Astrophys.*, 286, 857
- Takami, K., Rezzolla, L., & Baiotti, L. 2014, *Phys. Rev. Lett.*, 113, 091104, doi: 10.1103/PhysRevLett.113.091104
- , 2015, *Phys. Rev. D*, 91, 064001, doi: 10.1103/PhysRevD.91.064001
- Tamborra, I., & Ando, S. 2016, *Phys. Rev. D*, 93, 053010, doi: 10.1103/PhysRevD.93.053010
- Tamborra, I., Hanke, F., Janka, H.-T., et al. 2014a, *Astrophys. J.*, 792, 96, doi: 10.1088/0004-637X/792/2/96
- Tamborra, I., Raffelt, G., Hanke, F., Janka, H.-T., & Müller, B. 2014b, *Physical Review D*, 90, 045032, doi: 10.1103/PhysRevD.90.045032
- Tanaka, M., & Hotokezaka, K. 2013, *Astrophys. J.*, 775, 113, doi: 10.1088/0004-637X/775/2/113
- Tanaka, M., Kato, D., Gaigalas, G., & Kawaguchi, K. 2020, *Mon. Not. Roy. Astron. Soc.*, 496, 1369, doi: 10.1093/mnras/staa1576
- Tanaka, M., Utsumi, Y., Mazzali, P. A., et al. 2017, *Publ. Astron. Soc. of Japan*, 69, 102, doi: 10.1093/pasj/psx121

- Tanaka, M., Kato, D., Gaigalas, G., et al. 2018, *Astrophys. J.*, 852, 109, doi: 10.3847/1538-4357/aaa0cb
- Tanvir, N. R., Levan, A. J., Fruchter, A. S., et al. 2013, *Nature*, 500, 547, doi: 10.1038/nature12505
- Tanvir, N. R., Levan, A. J., González-Fernández, C., et al. 2017, *Astrophys. J. Lett.*, 848, L27, doi: 10.3847/2041-8213/aa90b6
- Tauris, T. M., Kramer, M., Freire, P. C. C., et al. 2017, *Astrophys. J.*, 846, 170, doi: 10.3847/1538-4357/aa7e89
- Thielemann, F. K., Arcones, A., Käppeli, R., et al. 2011, *Progress in Particle and Nuclear Physics*, 66, 346, doi: 10.1016/j.ppnp.2011.01.032
- Thompson, T. A., Burrows, A., & Meyer, B. S. 2001, *Astrophys. J.*, 562, 887, doi: 10.1086/323861
- Timmes, F. X., Woosley, S. E., & Weaver, T. A. 1996, *Astrophys. J.*, 457, 834, doi: 10.1086/176778
- Torres-Rivas, A., Chatziioannou, K., Bauswein, A., & Clark, J. A. 2019, *Phys. Rev. D*, 99, 044014, doi: 10.1103/PhysRevD.99.044014
- Troja, E., Piro, L., van Eerten, H., et al. 2017, *Nature*, 551, 71, doi: 10.1038/nature24290
- Typel, S., Röpke, G., Klähn, T., Blaschke, D., & Wolter, H. H. 2010, *Physical Review C*, 81, 015803, doi: 10.1103/PhysRevC.81.015803
- Vartanyan, D., Burrows, A., & Radice, D. 2019, *Mon. Not. R. Astron. Soc.*, 489, 2227, doi: 10.1093/mnras/stz2307
- Vassh, N., Vogt, R., Surman, R., et al. 2019, *Journal of Physics G Nuclear Physics*, 46, 065202, doi: 10.1088/1361-6471/ab0bea
- Vieira, N., Ruan, J. J., Haggard, D., et al. 2022, arXiv e-prints, arXiv:2209.06951. <https://arxiv.org/abs/2209.06951>
- Villar, V. A., Guillochon, J., Berger, E., et al. 2017, *Astrophys. J. Lett.*, 851, L21, doi: 10.3847/2041-8213/aa9c84
- Vincent, T., Foucart, F., Duez, M. D., et al. 2020, *Phys. Rev. D*, 101, 044053, doi: 10.1103/PhysRevD.101.044053
- von Groote, J. C. 2014, Phd thesis, Technische Universität München, München
- Wanajo, S. 2006, *Astrophys. J.*, 647, 1323, doi: 10.1086/505483
- Wanajo, S., Janka, H.-T., & Müller, B. 2011, *Astrophys. J. Lett.*, 726, L15, doi: 10.1088/2041-8205/726/2/L15
- , 2013a, *Astrophys. J. Lett.*, 767, L26, doi: 10.1088/2041-8205/767/2/L26
- , 2013b, *Astrophys. J. Lett.*, 774, L6, doi: 10.1088/2041-8205/774/1/L6
- Wanajo, S., Müller, B., Janka, H.-T., & Heger, A. 2018, *Astrophys. J.*, 852, 40, doi: 10.3847/1538-4357/aa9d97
- Wanajo, S., Sekiguchi, Y., Nishimura, N., et al. 2014, *Astrophys. J. Lett.*, 789, L39, doi: 10.1088/2041-8205/789/2/L39
- Watson, D., Hansen, C. J., Selsing, J., et al. 2019, *Nature*, 574, 497, doi: 10.1038/s41586-019-1676-3
- Waxman, E., & Bahcall, J. 1997, *Phys. Rev. Lett.*, 78, 2292, doi: 10.1103/PhysRevLett.78.2292
- Waxman, E., Ofek, E. O., & Kushnir, D. 2019, *Astrophys. J.*, 878, 93, doi: 10.3847/1538-4357/ab1f71
- Waxman, E., Ofek, E. O., Kushnir, D., & Gal-Yam, A. 2018, *Mon. Not. Roy. Astron. Soc.*, 481, 3423, doi: 10.1093/mnras/sty2441
- Winteler, C., Käppeli, R., Perego, A., et al. 2012, *Astrophys. J. Lett.*, 750, L22, doi: 10.1088/2041-8205/750/1/L22
- Witti, J., Janka, H. T., & Takahashi, K. 1994, *Astron. Astrophys.*, 286, 841
- Wollaeger, R. T., Korobkin, O., Fontes, C. J., et al. 2018, *Mon. Not. Roy. Astron. Soc.*, 478, 3298, doi: 10.1093/mnras/sty1018
- Wongwathanarat, A., Janka, H. T., & Müller, E. 2013, *Astronomy and Astrophysics*, 552, A126, doi: 10.1051/0004-6361/201220636

- Woosley, S., & Janka, T. 2005, *Nature Physics*, 1, 147, doi: 10.1038/nphys172
- Woosley, S. E. 1977, *Nature*, 269, 42, doi: 10.1038/269042a0
- , 1993, *Astrophys. J.*, 405, 273, doi: 10.1086/172359
- Woosley, S. E., & Baron, E. 1992, *Astrophys. J.*, 391, 228, doi: 10.1086/171338
- Woosley, S. E., Hartmann, D. H., Hoffman, R. D., & Haxton, W. C. 1990, *Astrophys. J.*, 356, 272, doi: 10.1086/168839
- Woosley, S. E., & Haxton, W. C. 1988, *Nature*, 334, 45, doi: 10.1038/334045a0
- Woosley, S. E., Heger, A., & Weaver, T. A. 2002, *Reviews of Modern Physics*, 74, 1015, doi: 10.1103/RevModPhys.74.1015
- Woosley, S. E., Wilson, J. R., Mathews, G. J., Hoffman, R. D., & Meyer, B. S. 1994, *Astrophys. J.*, 433, 229, doi: 10.1086/174638
- Wu, M.-R., Barnes, J., Martínez-Pinedo, G., & Metzger, B. D. 2019, *Phys. Rev. Lett.*, 122, 062701, doi: 10.1103/PhysRevLett.122.062701
- Wu, M.-R., Fernández, R., Martínez-Pinedo, G., & Metzger, B. D. 2016, *Mon. Not. R. Astron. Soc.*, 463, 2323, doi: 10.1093/mnras/stw2156
- Wu, M.-R., & Tamborra, I. 2017, *Phys. Rev. D*, 95, 103007, doi: 10.1103/PhysRevD.95.103007
- Xing, Z., Centrella, J. M., & McMillan, S. L. W. 1994, *Phys. Rev. D*, 50, 6247, doi: 10.1103/PhysRevD.50.6247
- Yadav, N., Müller, B., Janka, H. T., Melson, T., & Heger, A. 2020, *Astrophys. J.*, 890, 94, doi: 10.3847/1538-4357/ab66bb
- Yasin, H., Schäfer, S., Arcones, A., & Schwenk, A. 2020, *Physical Review Letters*, 124, 092701, doi: 10.1103/PhysRevLett.124.092701
- Zha, S., Leung, S.-C., Suzuki, T., & Nomoto, K. 2019, *Astrophys. J.*, 886, 22, doi: 10.3847/1538-4357/ab4b4b
- Zha, S., O'Connor, E. P., Chu, M.-c., Lin, L.-M., & Couch, S. M. 2020, *Phys. Rev. Lett.*, 125, 051102, doi: 10.1103/PhysRevLett.125.051102
- Zha, S., O'Connor, E. P., Couch, S. M., Leung, S.-C., & Nomoto, K. 2022, *Mon. Not. R. Astron. Soc.*, 513, 1317, doi: 10.1093/mnras/stac1035
- Zha, S., O'Connor, E. P., & da Silva Schneider, A. 2021, *Astrophys. J.*, 911, 74, doi: 10.3847/1538-4357/abec4c
- Zhang, W., Woosley, S. E., & MacFadyen, A. I. 2003, *Astrophys. J.*, 586, 356, doi: 10.1086/367609
- Zhu, Y., Wollaeger, R. T., Vassh, N., et al. 2018, *Astrophys. J. Lett.*, 863, L23, doi: 10.3847/2041-8213/aad5de
- Zhu, Y. L., Perego, A., & McLaughlin, G. C. 2016, *Phys. Rev. D*, 94, 105006, doi: 10.1103/PhysRevD.94.105006